

Mechatronics and Control Solutions for Increasing the Imaging Speed in Atomic Force Microscopy.

Stefan Kuiper

PhD Thesis

Cover: Drawing of an Atomic Force Microscope

MECHATRONICS AND CONTROL SOLUTIONS FOR INCREASING THE IMAGING SPEED IN ATOMIC FORCE MICROSCOPY.

PROEFSCHRIFT

ter verkrijging van de graad van doctor
aan de Technische Universiteit Delft,
op gezag van de Rector Magnificus Prof. ir. K.C.A.M. Luyben,
voorzitter van het College voor Promoties,
in het openbaar te verdedigen op

dinsdag 8 mei 2012 om 15:00

door

Stefan KUIPER

Werktuigbouwkundig Ingenieur
geboren te Zwolle

Dit proefschrift is goedgekeurd door de promotoren:

Prof.dr.ir. P.M.J. Van den Hof

Prof.dr.ir. G. Schitter

Samenstelling promotiecommissie:

Rector Magnificus,	voorzitter
Prof.dr.ir. P.M.J. Van den Hof,	Technische Universiteit Delft, promotor
Prof.dr.ir. G. Schitter,	Vienna University of Technology, promotor
Prof.dr.ir. R.A. de Callafon,	University of California, San Diego
Dr. A. Sebastian,	IBM Research, Zurich
Prof.dr.ir. M. Steinbuch,	Technische Universiteit Eindhoven
Prof.ir. R.H. Munnig Schmidt,	Technische Universiteit Delft
Prof.dr. U. Staufer,	Technische Universiteit Delft

disc

This dissertation has been completed in partial fulfillment of the requirements of the Dutch Institute of Systems and Control (DISC) for graduate study.

ISBN: 978-94-6191-248-0

Copyright © 2011 by Stefan Kuiper.

All rights reserved. No part of the material protected by this copyright notice may be reproduced or utilized in any form or by any means, electronic or mechanical, including photocopying, recording or by any information storage and retrieval system, without written permission from the copyright owner.

Printed in The Netherlands

Author's email: stefankuiper@hotmail.com

Preface

The thesis is the result of my PhD project that I have done in the last four and a half years within the Delft Center for Systems and Control (DCSC). The project was part of a program on high speed Atomic Force Microscopy. I owe many people gratefulness for their support, encouragements and inputs that have contributed to the realization of this thesis.

I would like to thank my promoter prof.dr.ir Georg Schitter for the possibility to work on this research topic that provides the great combination of theory and practice that I like so much. Your supervision, help and inputs were very important to me throughout this project. While you moved to Vienna after 2.5 years in the project, you made sure that this did not have any negative effect on my project by keeping one AFM instrument in Delft, maintaining the frequent contacts, and providing me with the opportunity to visit Vienna for a couple of months.

I am also very much obliged to my promoter prof.dr.ir. Paul Van den Hof. Your inputs and critical questioning during our meetings often forced me to rethink the things I was doing. This really helped me to get better understanding and grips on my work. Although due to my stay in Vienna and subsequently your stay in California there were only few occasions we could actually meet in person within the last year of the project, you made sure I promptly received your feedbacks on my writings and gave me the right critical inputs I needed to finalize the work. This way we were able to maintain a tight planning towards the end.

During the project I very much enjoyed and benefited from the cooperation and discussions I had with Jan van Hulzen, Paul Rutten, Hans Yoo, Amol Khalate, Xavier Bombois, and many others. For the practical part of the project I received a lot of help and support from Kees Slinkman, Ron van Puffelen and Arjan van Dijke, which was really important for me to achieve the experimental results. I would also like to thank Kitty, Ellen, Esther, Saskia, Linda and Olaf for their valuable organizational support. Furthermore, I would like to thank the members of my PhD committee for providing me with constructive remarks, which helped me a lot in finalizing the thesis.

My time at DCSC would not have been so great if it wasn't for the great colleagues at DCSC, with whom I had frequent talks, discussions, lunch, sports, and beers. I would especially like to mention Jan, Arturo, Nikola, Jacopo, Ivo H., Ivo G., Hans, Gijs, Pieter, Patricio, Ilhan, Rogier, Justin, Navin, Federico, Pawel, Andrea, Marco, Aleksander, Anil, Gabriel, Snezana, Mathieu, Paulo, Jianfei, Hong,

Jelmer, Solomon, Mernout, Sara, Coen, Amol, Ali, Jan Willem, Rufus, Alfredo, thank you all for being great colleagues and friends!

From April till July 2011 I had the great pleasure of visiting the Automation and Control institute (ACIN) in Vienna as a visiting researcher. I want to thank the people of the ACIN for this great opportunity and their hospitality, and in particular René, Shingo and Dominik for making sure that I got to see all the nice places in and around Vienna!

For their valuable help during my PhD defense, I would like to thank Martine Fledderus and Rick ten Berge for being my paranimfs.

Finally, my biggest thanks goes to my family and friends. Mom and dad, thank you for your unconditional support and your encouragements. Annerie, thank you for all your love and support, and for your patience throughout these years!

Stefan Kuiper,
Voorburg, April 2012.

Contents

Preface	v
1 Introduction	1
1.1 Atomic force microscopy	1
1.1.1 Principle of AFM	1
1.1.2 Image quality	3
1.2 Scope of the thesis	5
1.3 State of the art in AFM design	6
1.3.1 Lateral scanning motion	6
1.3.2 Control of the tip-sample force	10
1.4 Research objectives	15
1.4.1 Damping the scanner resonances via self-sensing actuation	15
1.4.2 Accuracy of the topography estimate	16
1.4.3 Dual actuated control of the tip-sample force	16
1.5 Approach	17
1.6 Outline	18
2 Active damping of the lateral scanner resonances by self-sensing actuation¹	21
2.1 Introduction	21
2.2 Self-sensing actuation	24
2.2.1 First principles modeling of self-sensing actuation	24
2.2.2 Self-sensing actuation of a single scanning axis	27
2.2.3 Self-sensing actuation of both scanning axes	29
2.3 Bridge circuit imbalance compensation	33
2.3.1 Hysteresis induced bridge circuit imbalance	33
2.3.2 Automated bridge circuit balancing	35
2.4 Controller design	38

2.5	Implementation	40
2.6	Experiments	41
2.6.1	Line-scan experiments	41
2.6.2	AFM-imaging	42
2.7	Conclusions	47
3	Tip-sample force control and topography estimation²	49
3.1	Introduction	49
3.2	Topography estimation problem	52
3.3	Robust design of the feedback controller and the topography estimator	56
3.3.1	Step 1: Identification and modeling of the actuator dynamics	57
3.3.2	Step 2: Model-based feedback controller and estimator design	58
3.3.3	Step 3: Improved estimator design	59
3.4	Design example and analysis	61
3.4.1	Identification and modeling	61
3.4.2	Controller and estimator design	63
3.4.3	Performance analysis	63
3.5	Experimental results	66
3.5.1	Implementation	67
3.5.2	Tracking performance	68
3.5.3	Influence of the estimator order on the topography estimation accuracy	68
3.5.4	Influence of the controller bandwidth on the topography estimation accuracy	69
3.6	Conclusions	72
4	Dual actuated control of the tip-sample force³	73
4.1	Introduction	73
4.1.1	Control problem in dual actuated AFM	75
4.1.2	Experimental Setup	77
4.1.3	Outline	77
4.2	Linear feedback controller design for dual actuated AFM	78
4.2.1	Design procedure nominal feedback controller	78
4.2.2	System identification and analysis	80
4.2.3	Model-based feedback controller design	82
4.3	Anti-windup ⁴ control for dual actuated AFM	92
4.3.1	Analysis saturation problem	92

4.3.2	Anti-Windup controller design	94
4.3.3	Experimental validation of the Anti-Windup controller	95
4.4	Imaging results	95
4.5	Addressing the topography estimation accuracy for dual actuated AFM	99
4.5.1	Topography estimation in dual actuated AFM	100
4.5.2	Integrated design of the feedback controller and topography estimator for dual actuated AFM	101
4.6	Conclusions	105
5	Conclusions and Recommendations	107
5.1	Conclusions	107
5.2	Recommendations	110
A	Identification and compensation of hysteresis within the topography estimation	113
A.1	Introduction	113
A.1.1	Compensating for hysteresis in topography estimation	114
A.2	Experimental results	115
	Bibliography	119
	List of Publications	127
	Summary	129
	Samenvatting	131
	Curriculum Vitae	133

Introduction

1.1 Atomic force microscopy

The invention of the scanning tunneling microscope (STM) in 1982 [9] was the starting point of the development of a whole family of scanning probe microscopes (SPM). The working principle of each SPM is to scan a sample in very close proximity of a very sharp measurement tip, and to record the tip-sample interaction. While STM is only limited to conductive materials, the invention of the Atomic Force Microscope (AFM) in 1986 [8] has enlarged the applicability of SPM to also image non-conductive materials. In AFM the measurement tip is mounted at the free end of a micro cantilever. By detecting the deflection of this cantilever the interaction forces between the tip and the sample can be measured [76]. By measuring and controlling the tip-sample force interaction, a large variety of sample properties can be captured, such as the sample topography and the local stiffness of the sample [7]. Moreover, by using specially functionalized tips electromagnetic properties [37], hydrophobicity of sample material [22], and charge distributions [67] can be measured. One major advantage of AFM over other high resolution imaging techniques such as electron microscopy is that AFM is not restricted to operate only in vacuum chambers, but can also be used in ambient environments or in liquids. Apart from being used as a measurement and imaging device, AFM can also be used for nanofabrication [100], such as nano scratching [99], electro-chemical processes [59], and nano manipulation [72]. Due to this huge versatility of the instrument, AFM has become one of the most popular tools in the field of micro-biology [35, 66, 23], material sciences [60], and in the high precision industry [104, 44, 12].

1.1.1 Principle of AFM

In Figure 1.1 the working principle of the AFM is depicted. The sample is probed by a very sharp tip with an end-radius on the order of a few nanometers, which is mounted on the free end of a micro cantilever, as shown in Figure 1.2. These tip and cantilever assemblies are typically produced out of silicon or silicon nitride.

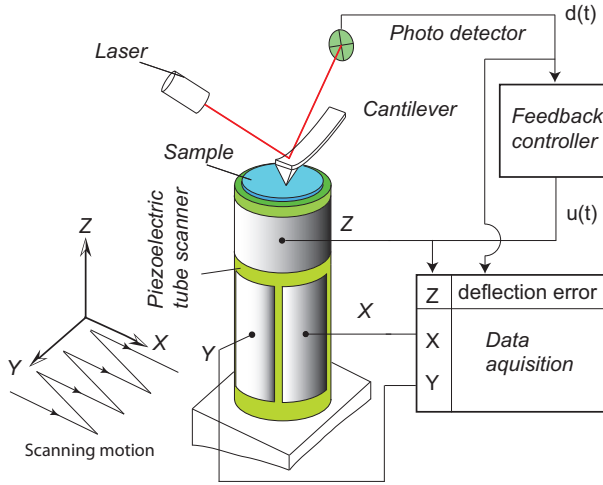


Figure 1.1: Schematic description of the Atomic Force Microscope

The cantilever beam represents a stiffness between the cantilever base and the tip in the order of 0.1 N/m up to about 100 N/m . When the tip is brought in close proximity of the sample, the interaction forces between the tip and the sample can be detected by measuring the deflection of the cantilever beam. Most often the cantilever deflection is detected by focussing a laser beam at the free end of the cantilever, and measuring the reflection of the laser spot with a segmented photodiode [3], as shown in Figure 1.1. The four segments of the photodiode allow to measure both the vertical deflection of the cantilever as well as its torsional deflection. Other methods for sensing the cantilever deflection are interferometry, capacitive sensing or via a piezoresistive layer deposited on the cantilever [76]. During imaging the sample is scanned relative to the measurement tip in a lateral scanning pattern in order to image a certain area of interest. This scanning pattern can be decomposed into a fast triangular scanning motion in the x-direction, and a slow triangular scanning motion in the y-direction. During scanning the interaction force between the tip and the sample is controlled by a feedback loop, manipulating the distance between the tip and the sample based on the measured cantilever deflection. This feedback loop prevents damage of the tip and the sample due to large interaction forces, and also allows to convert the force measurement into an estimate of the sample topography. In order to provide the lateral scanning motion and to allow the control of the tip-sample interaction force, a high precision positioning stage is used which can position the sample relative to the measurement tip in all three spatial directions.

While scanning, the measured cantilever deflection and the compensating actions of the feedback loop are recorded by the system's data acquisition in order to obtain a map of the sample topography, and possibly other sample properties. Figure 1.3 shows an AFM image of a calibration grating. Depending on the control bandwidth, the topography variations with lower spatial frequency are mainly revealed by the compensating actions of the feedback loop, while the sample topography variations that occur faster than the control bandwidth of the feedback

loop during imaging are revealed by the measured cantilever deflection. Therefore, often both the feedback controller output $u(t)$, and the measured cantilever deflection signal $d(t)$ are presented in separate images for each imaging experiment, which are denoted the 'height image' (Fig. 1.3a) and the 'cantilever deflection image' (Fig. 1.3b), respectively. Other signals may be presented as well such as the measured torsional deflection of the cantilever, which is a measure for the friction between the tip and the sample during imaging, as shown by Figure 1.3c. The combination of mechanics, electronics, and controls makes the AFM a highly complex mechatronic system, which strongly relies on proper design and integration of all its components to achieve the high requirements on its imaging performance.

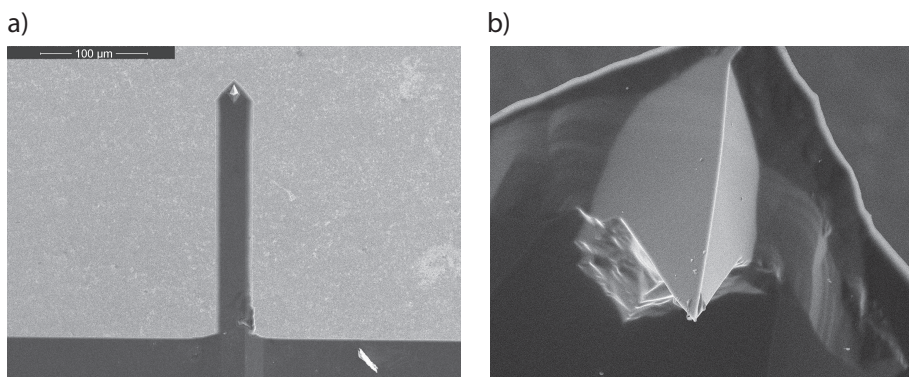


Figure 1.2: Scanning electron microscope images of a tip-cantilever assembly (a), and a close-up of the actual tip (b). The cantilever beam typically has a length of 100 to 300 μm , and the tip typically has a height of 10 μm .

1.1.2 Image quality

The quality of a topography image obtained with an AFM is determined by (i) the resolution of the image which is defined by the smallest increment (detail) the instrument is capable of resolving, and (ii) the accuracy (or 'exactness') of the measured sample dimensions. In AFM imaging the lateral resolution is largely limited by the finite sharpness of the tip, which convoluted with the sample surface results in dilation of the measured sample features, shrinking the holes and broadening the peaks on the sample surface [61]. Besides the finite sharpness of the tip, the resolution is also strongly depending on the precision, or repeatability of the imaging process. This notion of repeatability denotes to which extend the outcome of multiple imaging experiment are the same when the experiments are repeated with the exact same imaging parameters and conditions. Throughout this thesis the term 'precision' is used to denote the degree at which the imaging experiments are subject to non-repeatable errors, while the term 'accuracy' is used to denote the degree at which the imaging experiments are subject to repeatable or 'systematic' errors.

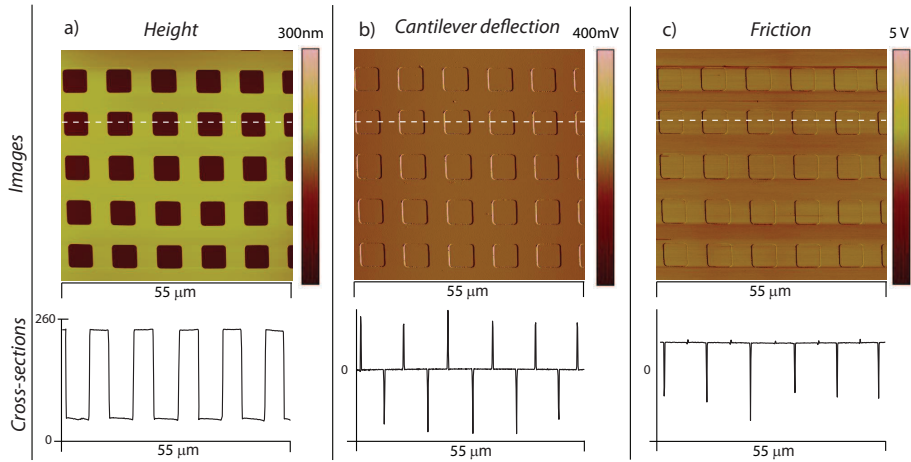


Figure 1.3: AFM images of a calibration grating with 180 nm deep, 10 μm pitch square holes, imaged in contact mode, and the cross-sections corresponding to the white dashed lines within the images. (a) shows the ‘height image’ which is directly obtained from the recorded feedback controller output $u(t)$, (b) shows the cantilever deflection image obtained from the measured cantilever deflection $d(t)$, and (c) shows the ‘friction image’ obtained from the measured torsional deflection of the cantilever.

As AFM is a mechanical microscope, the accuracy and resolution that can be obtained with an AFM imaging experiment are largely depending on the accuracy and precision at which the sample is positioned relative to the measurement tip, and the accuracy and precision of the tip-sample force measurement.

The precision of an imaging experiment can be affected by non-repeatable distortions, such as noise from the electronics, temperature drifts, vibrations from the environment, and the Brownian noise acting on the micro cantilever [76]. How these distortions affect the precision of the imaging experiments strongly depends on the duration of the imaging experiment and on the sampling time (or pixel-rate), determining which frequency components of the overall disturbance spectrum are revealed within the image. For a long duration imaging experiment with a low sampling time the obtained imaging precision may be mostly affected by the low frequency (temperature) drifts within the instrument, while a short duration imaging experiment with high sampling rate may be mostly affected by the higher frequency noise stemming for instance from the electronics.

The accuracy of the imaging experiment can be affected by repeatable distortions such as calibration errors, and possible non-linearity of the instrument. The requirements on the accuracy of the instrument are strongly depending on the type of imaging application, in which we can distinguish quantitative and qualitative imaging applications. In quantitative imaging experiments the goal is to exactly trace back the dimensions of the measured sample features towards the international length standards, requiring a high absolute accuracy of the instrument.

Meanwhile, in qualitative imaging experiments it is mostly important that the sample features are resolved with the correct relative proportions, showing low malformations, while the absolute dimensions of the sample features are of lesser importance. Therefore, qualitative imaging experiments require sufficient relative accuracy of the instrument, rather than requiring a high absolute accuracy of the data scaling.

1.2 Scope of the thesis

One of the main challenges in the development of AFM instruments nowadays, is to improve the relatively low imaging speed of these instruments. As in AFM the sample is probed point by point, AFM imaging is a rather time consuming process, taking on the order of several minutes per frame for most commercially available AFM's nowadays. Especially in industrial application, like in the semiconductor industry where AFM's are used for quality control and process monitoring [12], the low imaging speeds results in low throughputs, making it a rather cost intensive process. Moreover, in the field of nanofabrication faster AFM imaging could significantly improve the production times, as in nanofabrication the substrate needs to be imaged after each manipulation cycle [72]. Furthermore, the low imaging speed of current AFMs does not allow the capturing of fast dynamical processes as they occur on the nano scale, which would be very valuable for many research applications, e.g. in molecular biology [5,36]. Therefore, improving the imaging speed of AFM could significantly widen up the field of application of these instruments in both the industrial environments as well as new research areas within the scientific community.

While improving the imaging speed is an important challenge in AFM design, it is vital that with the improved imaging speed the quality of the AFM image is maintained. When increasing the imaging speed, the stronger excitation of higher order dynamical modes may have degrading effects on the achievable image quality [16,83]. Moreover, the higher data sampling rates in high speed AFM may result in higher sensitivity to measurement noise and external disturbances, which have adverse effects on the achievable resolution. These aspects limit the application of these instruments as a reliable inspection and measurement tool in production environments where high throughputs are required. In order to improve the accessibility of reliable measurement data at the nanometer scale, cost-effective methods need to be developed to improve the imaging speed of AFM without hampering the image quality.

As discussed above, the imaging performance of AFM strongly relies on proper mechatronic design and control of the instrument. Therefore, the main question driving this research can be formulated as:

Main Research Question:

Can the mechatronics and control of current AFM instruments be improved to increase the system performance in terms of imaging speed and image quality?

1.3 State of the art in AFM design

The operation of AFM can be split in two main tasks: (i) performing the lateral scanning motion of the sample relative to the tip in order to probe a certain area of interest, and (ii) to control the tip-sample force in order to prevent damage of the tip and the sample and to convert the force measurement into an estimate of the sample topography. Although the measures taken to perform these tasks might sometimes influence each other via cross-talk, in this section the state of the art in AFM design is discussed along this division in operating tasks. While besides imaging the AFM can also be used for other applications such as nano-fabrication and force spectroscopy as also discussed in Section 1.1, in this section the discussion is restricted to AFM imaging which is the most important application area of AFM.

1.3.1 Lateral scanning motion

For most commercially available AFM systems, the positioning of the sample or measurement tip in all three spatial directions is provided by a scanning stage utilizing piezoelectric tube scanners [10], which consist of a tube of piezoelectric material with segmented electrodes on the side, as shown in Figure 1.1. The lateral scanning motion is provided by applying an antiparallel voltage over the electrode pairs on the lower end of the tube, which induces a bending motion of the tube, and consequently an in-plane motion of the sample placed on top. The vertical displacement of the sample is achieved by applying a voltage over an ring electrode which induces a longitudinal elongation of the tube. While Figure 1.1 depicts an AFM system in which the positioning stage is moving the sample, AFMs in which the measurement probe is moved are available as well. Besides these piezoelectric tube-scanners, also AFM stages are developed utilizing piezoelectric stack actuators [5, 79, 63], which generally result in a stiffer construction with higher fundamental resonance frequencies.

The precision which can be achieved with these piezoelectric actuators is very high, as they form a rigid connection between the moving sample and the base of the cantilever, which results in a low sensitivity of the instrument to external disturbances. A major drawback of these piezoelectric actuators, however, is that the positioning accuracy is compromised by the effects of hysteresis, creep and also by the weakly damped resonant modes within these actuators [33, 17, 83]. Several methods can be found in literature to compensate for these adverse effects. Although the measures taken to compensate for these different effects can be combined, in discussing these methods a division is made between the compensation of the creep and hysteresis which are particularly dominant at low frequency regime, and the compensation of the higher order scanner dynamics which are mainly dominant in the high frequency regime.

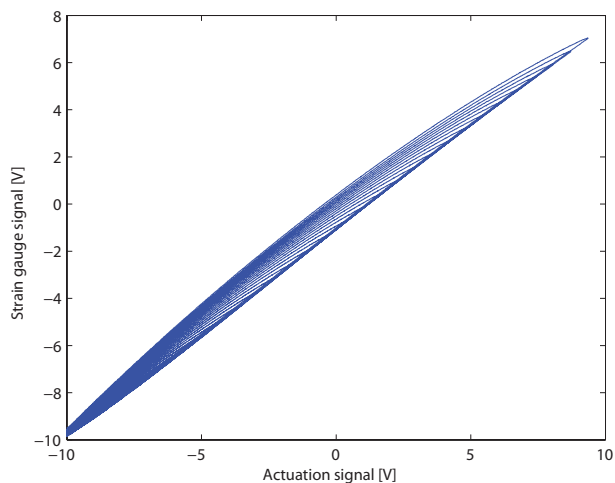


Figure 1.4: Measured hysteresis loops of a piezoelectric stack actuator for various amplitudes of the input signal [96].

Compensating scanner hysteresis and creep

Creep results in a slow drift of the piezoelectric actuator, initiated by a change in offset voltage over the electrodes, as occurs for instance when changing to another scan-area. After the offset change the drift stemming from the creeps settles out within a time frame of a couple of seconds up to about a minute. Therefore, the creep may distort the AFM imaging process mainly during the initialization phase of the imaging experiment, but settles out when the scanning operation proceeds [24, 61].

Hysteresis is a non-linear effect originating from molecular friction within the piezo element, which results in the forward motion not fully overlapping the backward motion of the scanner [17, 33], as shown in Figure 1.4. Because of this nonlinearity stemming from the hysteresis, most often only the forward ('trace') or the backward ('retrace') scanning motion is used to record the imaging data [24]. As the effects of hysteresis are very repeatable over several scan-lines, the precision of the scanning motion is not compromised by the hysteresis. However, due to the non-linear effects of hysteresis it is difficult to trace back the exact location of the tip relative to the sample which compromises the accuracy of the instrument [108], especially when the scanning motion is operated in open-loop .

In literature several methods are discussed to improve the accuracy of the scanning motion by compensating for hysteresis and creep. Using dedicated position sensors measuring the scanner displacement, the scanner accuracy can be significantly improved by direct feedback control [95, 74, 89, 14]. Especially for high accuracy metrological applications this method is preferred as the position of the sample with respect to the measurement tip can be directly traced back using the (interferometric) position sensors [63, 98], given that the system is designed following the Abbé-principles [91]. A major drawback of direct feedback control,

however, is that the precision of the instrument may be compromised by feeding back the measurement noise stemming from the displacement sensors, which is especially a problem when higher control bandwidths are required for faster AFM imaging. Moreover, the use of dedicated position sensors is often very cost intensive, and therefore not always very efficient for all applications. As an alternative, feedforward compensation methods have been proposed to compensate for the non-linearities and scanner dynamics [17, 108]. As feedforward compensation methods work in an open-loop manner, the precision of the instrument is not compromised by feedback of measurement noise. Because compensating for hysteresis and creep in an open loop manner requires accurate knowledge of the scanners non-linear behavior, and also frequent calibration, the achievable scanning accuracy with these open-loop control methods are limited. However, for most qualitative imaging applications the achieved accuracy with open-loop compensation is sufficient, and therefore these methods can be found in most commercially available AFM systems. The hysteresis within the piezo actuators can also be compensated for to a large extent, by using charge amplifiers instead of voltage amplifiers [30]. A drawback of charge control, however, is that the charge measurement is only possible above a certain bandwidth, and therefore the stability and accuracy of charge amplifiers is compromised at lower frequencies.

As the scanning motion in AFM is a repetitive motion, the tracking errors stemming from the hysteresis are also repetitive, which allows to measure the tracking errors from one scan-line, and based on that apply a compensating action for the subsequent scan-lines. This is the principle of Iterative Learning Control (ILC) [13], which has been investigated to compensate for the effects of hysteresis in AFM [56, 107]. As in ILC the measured tracking error is not fed back directly, it allows to average out the measurement noise over several scan-lines before calculating the compensating actions for the subsequent scan-lines [78, 96]. This quasi closed-loop control method therefore allows to significantly improve the scanning accuracy of the instrument without compromising the precision of the scanning motion. This is particularly important when high control bandwidths are required as in high speed AFM imaging. This data averaging may also relax the noise specifications of the position sensors, allowing the use of cheaper position sensors like strain-gages [78, 96]. However, ILC is only capable of compensating for a limited amount of uncertainty in the actuator dynamics [13], and therefore most often the control bandwidth with ILC is limited by the large dynamical uncertainty associated with the weakly damped resonant modes of the scanner at higher frequencies.

Compensating for scanner resonances

While hysteresis and creep limit the accuracy of the scanning motion particularly at larger amplitude and at lower frequencies, the weakly damped resonance modes start to compromise the scanning accuracy particularly when imaging faster, resulting in scanner oscillations when excited by the scanning signals [16, 83]. In Figure 1.5 the influence of the scanner oscillations on the quality of the AFM image is shown. As a rule of thumb, if the weakly damped resonances are not compensated for the scan-rate is limited to about 1 percent of the first fundamental

resonance frequency of the scanner as otherwise the scan accuracy is too strongly compromised by the scanner oscillations [36]. Another drawback of these weakly damped resonances is that these increase the sensitivity of the system to external disturbances, and may induce strong couplings with the z-axis [71,97], which may compromise the performance of the feedback loop controlling the tip sample force [97].

In order to improve the scan-rate of AFM imaging, several prototype AFM systems are reported in literature with improved mechanical design of the scanner stage aimed at pushing the resonant modes to higher frequencies, most often utilizing piezoelectric stack actuators instead of the piezoelectric tube actuators [5,79]. These high speed scanners allow scan speeds of a few thousand lines per second, which depending on the image resolution results in several frames per second. Some groups have investigated the use of sinusoidal scanning motions instead of the usual triangular scanning motion, using a resonating tuning fork to provide the fast scanning motion [68,41]. Although sinusoidal scanning allows higher scan-rates, the accuracy of these methods is hampered by uncertainty of the damping within the oscillating scanner, and the non-constant scanning velocity.

In order to prevent excitation of the resonant modes by the scanning signals feedforward control methods can be applied [16,83], or signal shaping methods [85], which have shown to allow about 15 times faster scanning as compared to the un-compensated case [83]. Also adaptive feedforward control methods are investigated in order to compensate for shifts in resonance frequencies due to varying load conditions [58,27]. A drawback of these open-loop control methods is that these can only compensate for the deterministic disturbances, but do not prevent excitation of these resonant modes due to external disturbances, or via the cross-talks with the z-axis which is used to track the (unknown) sample topography.

Alternatively, active damping of the resonant modes can be achieved by direct feedback control, utilizing position sensors to measure the scanner displacement [95,74,89,14]. Active damping by feedback control allows to also compensate for non-deterministic excitation of the resonant modes, and allows certain robustness against variations in the dynamical behavior of the scanner, which might occur when changing the sample and measurement tip. When using the feedback controller only to apply active damping to the resonant modes, and not to compensate for the effects of hysteresis and creep, a selective feedback controller can be used with a high feedback gain only in the frequency regions of the resonant modes, in order not to severely compromise the scanners precision by the feedback of measurement noise [88]. However, the use of dedicated position sensors is rather cost intensive, and most often difficult to integrate within the scanner design without adding additional weight to the scanning unit, which would again lower the bandwidth of the system. In [6,64] the use of external position sensors is omitted by using part of the available electrode surface of a piezoelectric tube for sensing, measuring the voltage change over these passive electrodes by the bending of the tube. Although this technique enables active damping of the fundamental resonances, the maximum scan-range is compromised as not the whole available electrode surface is used for actuation. Alternatively in [31], a reduction of scanner oscillations is achieved by connecting a shunt impedance in parallel

with the scan-electrodes, damping the resonances within the fast scanning axis of the scanner by about 20 db.

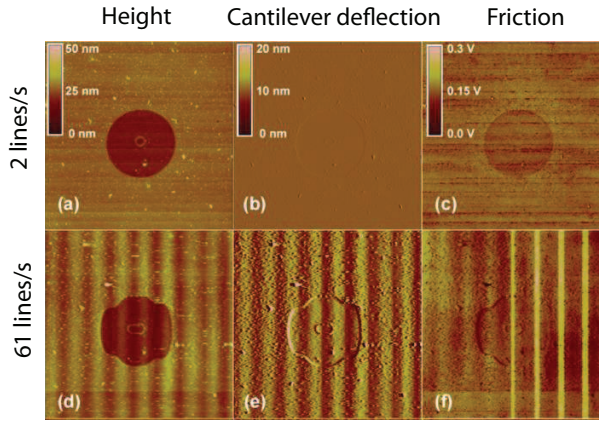


Figure 1.5: Silica-bead projection pattern imaged at 2 lines per second (a-c), and at 61 lines per second (d-f), demonstrating the image distortions stemming from the excitation of the undamped lateral resonance mode of the scanner when imaging at high speed [83].

1.3.2 Control of the tip-sample force

In AFM, the tip-sample interaction forces are controlled in a feedback loop by detecting the deflection of the cantilever and manipulating the distance between the tip and the sample as shown by Figure 1.7. The reason for this feedback loop is twofold: (i) in order to prevent damage or wear of the tip and the sample, and (ii) to convert the force measurement into an estimate of the sample topography.

In this subsection the state of the art in controlling the tip-sample force is discussed, divided in the different imaging modes, the tracking of the sample surface, and the estimation of the sample topography.

Imaging modes

The force interaction between the tip and the sample is stemming from the attractive van-der-Waals, capillary, magnetic and electrostatic forces, and the repulsive forces due to the Pauli repulsion [76]. When the tip is moving closer to the sample surface, it first enters a regime in which the attractive forces are dominant, before entering the regime in which the repulsive forces are dominant, as shown by the qualitative sketch in Figure 1.6a. The actual tip-sample force interaction curve strongly depends on the material and geometric properties of the tip and the sample, and the environmental conditions. The tip sample force interaction can be measured by a force curve experiments in which the sample is moved towards the tip and back, while measuring the cantilever deflection [24]. The typical shape

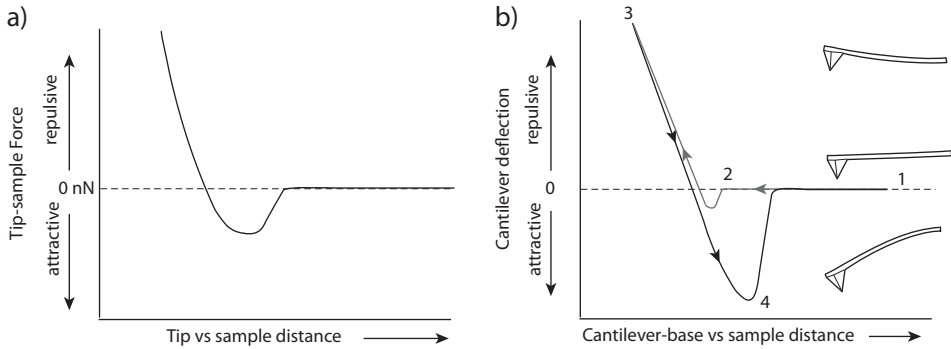


Figure 1.6: (a) Qualitative sketch of the interaction force between the tip and the sample as a function of the distance between the two, showing the attractive and repulsive regime.

(b) Qualitative sketch of the typical result of a force curve measurement, showing the cantilever deflection as a function of the distance between the sample and the cantilever base. The experiment is started at point 1 at which the tip is far from the sample surface and moved towards the sample. At point 2 the 'snap-in' occurs due to the attractive forces. While the distance is further reduced the tip-sample force enters the repulsive regime until a user defined maximum is reached at point 3. During the retraction phase the tip keeps on sticking to the sample surface due to the adhesion forces, until it snaps loose at point 4.

of such a force distance curve is by the qualitative sketch in Figure 1.6b. Based on the measured cantilever deflection and the (known) stiffness parameters of the cantilever, the tip-sample force curve of Figure 1.6a can be derived.

During AFM imaging, the interaction forces between the tip and the sample can be measured via different imaging modes, which can be divided in static imaging modes, and dynamics imaging modes [7, 24]. In static mode imaging the cantilever deflection signal is directly used as an input for the feedback controller, which is aimed to control the tip-sample force to a constant setpoint level, and thus a constant tip-sample distance throughout the scan-area, as shown by Figure 1.7b. In static mode imaging the tip and the sample are in such close contact that the overall tip-sample forces are in the repulsive regime (cf. Fig. 1.6), or 'in contact'. Consequently, static mode imaging is also referred to as 'contact' mode imaging.

In dynamic mode imaging the cantilever is oscillating close to its natural resonance frequency, driven by for instance a small piezoelectric actuator located at the mounting spot of the cantilever. The oscillation amplitude and phase with respect to the driving signal are depending on the tip-sample interactions, and therefore can be used as the input variable for the feedback loop in order to control the average height between the tip and the sample surface [24]. Furthermore, in 'Frequency Modulation' (FM) mode the frequency of the excitation signal for the oscillating cantilever is controlled towards a predefined phase angle via a phase-

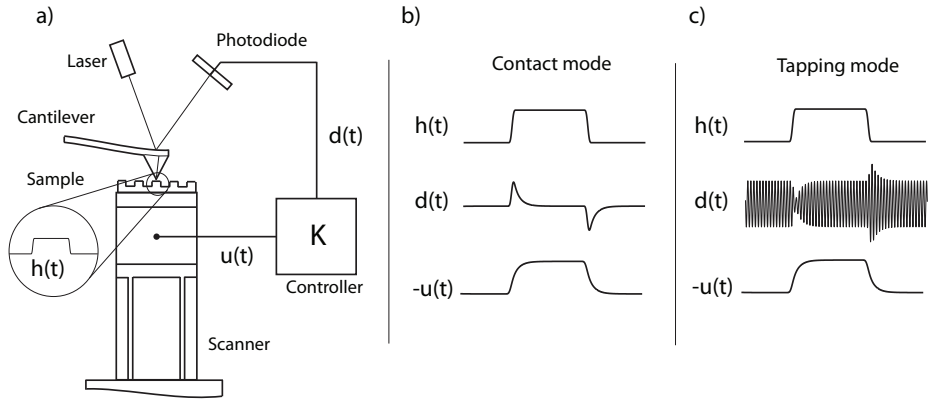


Figure 1.7: Schematic of the feedback loop in AFM controlling the tip-sample force (a), with the sample topography $h(t)$, the measured cantilever deflection signal $d(t)$, and the compensating action of the feedback controller $u(t)$. In contact mode imaging (b) the feedback loop is manipulating the height of the sample relative to the cantilever base in order to control the deflection of the cantilever towards a constant set-point value. In tapping mode imaging (c) the cantilever is oscillating above the sample surface, while the feedback controller is controlling the oscillation amplitude of the cantilever.

locked loop [2]. This phase-locked loop therefore allows the to detect the changes in resonance frequency due to the tip sample interaction, which can also be used as an input for the feedback controller to control the height of the oscillating tip above the sample surface.

In dynamic non-contact imaging the tip is oscillating at a small amplitude above the sample surface within the attractive regime of the tip-sample interaction (cf. Fig. 1.6), while most often the tip sample distance is controlled by detecting the phase or in FM mode. Dynamic non-contact mode imaging allows for very low tip-sample forces which prevent degradation of the tip and the sample, and allows for extremely high resolution imaging when operated in vacuum [32]. However, in ambient conditions most samples develop a liquid meniscus layer on the surface which makes it difficult to prevent the tip from sticking to the surface in non-contact mode imaging. To overcome this problem dynamic contact mode imaging, or *tapping* mode imaging [109] has been developed in which the tip is oscillating above the sample surface with a larger amplitude of about 10 nm up to about a 100 nm. The momentum of the oscillating tip prevents it from sticking to the sample surface. In tapping mode imaging the tip sample interaction reaches into the repulsive regime, which causes a decrease in oscillation amplitude when the average tip-sample distance is reduced. Therefore, in tapping mode the oscillation amplitude of the cantilever is most often used as the controlled variable in the feedback loop in order to maintain a constant average tip-sample distance, as shown in Figure 1.7c.

The advantage of tapping mode imaging over static contact mode imaging is that

the lateral shear forces between the tip and the sample are significantly smaller, which reduces the chance of damage and wear of the tip and the sample. A limitation of tapping mode imaging, however, is that converting the measured cantilever oscillation into an oscillation amplitude signal requires demodulation and low-pass filtering which adds additional dynamics and phase lag to the feedback loop. Therefore, when higher imaging bandwidths are required often contact mode imaging is preferred because it allows a higher control bandwidth [79, 68], although recently significant improvements have been made on high speed tapping mode imaging [73, 4, 47, 42].

For either imaging mode, a strong limitation on the achievable measurement bandwidth is posed by the first resonance frequency of the cantilever [36]. Therefore, for high speed imaging applications, several groups have developed very short cantilevers with high fundamental resonance frequencies, sometimes even above 1 MHz [106, 5].

Tracking of the sample topography

During imaging it is important that the tip-sample forces are not getting too high to prevent damage or wear of the tip and the sample. Therefore, a high feedback bandwidth of the vertical feedback loop is important to minimize the tip-sample force variations while scanning. This becomes particularly important when imaging fragile (biological) samples at a high scan-rate, and on rough sample surfaces [36].

Improved control of the tip-sample force by use of modern model-based control techniques has been investigated [80, 75], taking into account the higher order actuator dynamics in the design of the feedback controller. Compared to the classical PI-controllers used in most commercially available AFM systems, model-based feedback control has shown to allow up to about 5 times higher closed-loop bandwidth [80]. Furthermore, feedforward control methods are investigated, making use of that fact that a large part of the topography variation are repetitive from one scan-line to the next [84].

The major limitation on the control bandwidth, however, is posed by the higher order dynamics of the actuators, which due to slight variations in the load conditions are unpredictable and difficult to model. Therefore, pushing the control bandwidth far beyond the first resonance frequencies of the scanner is most often not possible. In order to allow higher control bandwidths, several prototype systems are reported with improved mechanical designs, optimized for higher resonance frequencies of the scanner, utilizing piezoelectric stack actuators [5, 79, 46, 29], as well as MEMS-based actuators with integrated measurement probes [93, 94]. Optimizing these type of actuators for high positioning bandwidth, however, comes at the cost of a reduction in positioning range, limiting the application of these actuators to samples with relatively small topographic features when used as the sole means of tracking the sample profile. Meanwhile, most often in AFM imaging the largest topographic variations to be tracked by the vertical feedback loop are relatively slowly varying for instance stemming from a small tilt of the sample, while the high frequency topography variations are typically of smaller amplitude. This aspect allows to combine a long-range,

low-bandwidth actuator with a short-range, high-bandwidth actuator in order to obtain a system with both a high control bandwidth as well as a large effective positioning range. This technique is generally referred to as dual-actuation, and has been thoroughly investigated for implementations on Hard Disk Drives (HDD) (e.g. [65, 40]), and also has been investigated for scanning probe microscopes [29, 93, 81, 43, 26], showing vast improvements on the control-bandwidths of the vertical feedback loops as compared to single actuated system, without sacrificing effective positioning range.

Topography estimation

During imaging both the measured cantilever deflection and the compensating action of the feedback control loop are recorded in order to determine the sample topography [24]. When imaging slow enough such that the feedback loop is able to maintain a constant tip-sample force, the sample topography is directly revealed by the compensating actions of the feedback loop, i.e. the opposite of the z-actuator displacement (cf. Fig. 1.7). Therefore, in high accuracy metrological AFM systems the sample topography is estimated by measuring the compensating actions of the z-actuator using high accuracy (interferometric) position sensors [63, 98]. However, for most commercially available AFM the use of such dedicated position sensors is too cost-intensive. Furthermore, the obtained imaging precision may be limited by the noise floor of these position sensors, which particularly becomes a problem at the higher bandwidth required for high speed AFM imaging. Therefore, in most AFM systems the sample topography is estimated based on the output of the feedback controller [24], assuming a static relation between the feedback controller output and the displacement of the z-actuator. Although this method allows for low cost, and low-noise topography estimation, the accuracy of such approach is limited as the actuator dynamics are neglected. To compensate for the inaccuracies stemming from the non-linear hysteresis within the piezoelectric z-actuator, the use of charge control has been investigated [28]. Moreover, when the bandwidth of the feedback controller is increased to allow faster imaging, also the high frequency resonances of the actuator may start to influence the topography estimation. To provide more accurate sample topography estimation the feedback controller output can be filtered by a model of the actuator dynamics [80], which is particularly relevant for high speed AFM imaging. While the compensation action of the feedback loop mostly reveals the low frequency topography variations, the topography variations that occur faster than the feedback bandwidth are revealed within the cantilever deflection signal, as also shown by Figure 1.7. Recently, high bandwidth topography estimation is shown by taking the cantilever deflection signal directly into account in the topography estimation [75], using an estimator embedded within a model-based feedback controller. This method can also be extended to dynamic imaging mode, by including a model of the sensor dynamics [57].

1.4 Research objectives

As evident from the investigation of the state of the art described above, high speed AFM imaging is a highly dynamical process in which the higher order dynamics of the entire system strongly influence the performance of the imaging process. Therefore, proper handling of the system dynamics is vital to allow high speed AFM imaging while maintaining a good imaging quality. This holds for both the lateral scanning motion, as well as for the control of the tip-sample force, and the topography estimation. Special high speed AFM systems are developed which are tailored for specific imaging experiments, and optimized to push the dynamics of the system to higher frequencies. Although these high speed AFM systems are capable of much higher imaging speeds than conventional AFM systems, the overall system architecture is often similar and the achievable imaging speed is restricted by the systems dynamics in the same manner as in conventional AFM. Therefore, in this research the focus is put on developing systematic techniques to handle these performance limiting factors, such that these techniques may be used to improve the imaging speed of both conventional AFM systems, as well as specialized high speed AFM systems. The following research questions are formulated to investigate methods to improve both the lateral scanning motion, as well as the control of the tip-sample force, and the topography estimation:

1.4.1 Damping the scanner resonances via self-sensing actuation

The weakly damped resonances of the scanner stage can cause oscillations when excited which poses a strong limitation on the achievable scan-rate and accuracy of the scanning motion. Excitation of the weakly damped lateral resonance modes by the a priori known scanning signals can be avoided by feedforward control, or by signal shaping. However, feedforward control does not allow to compensate for the excitation of the resonance modes by unknown environmental disturbances, or by cross-talk with the z-axis which tracks the unknown sample topography. Moreover, feedforward control requires accurate knowledge of the systems dynamics and is therefore very sensitive for slight changes in the system dynamics, occurring for instance when changing the tip or sample. Alternatively, feedback control may be applied, allowing robust active damping of the resonance modes, using dedicated displacement sensors to measure the movement of the positioning stage. Active damping by feedback control allows to compensate for the excitation of the weakly damped resonance modes by scanning signals, as well as environmental disturbances and cross-talk with the z-axis. However, the displacement sensors required for feedback control are typically too cost-intensive for most imaging applications, require full redesign of the system's hardware, and in many cases have a too high noise floor which limits the precision of the system when used for direct feedback control. Using the piezo material itself as an actuator and sensor simultaneously has been investigated in the smart structure community [20]. These techniques are denoted 'self-sensing actuation', and eliminate the need for dedicated position sensors. Recently, similar techniques have been applied on piezoelectric positioning stages, damping the resonance mode via ac-

tive shunt-damping [31].

A difficulty for the practical implementation of the self-sensing actuation principle on piezoelectric positioning stages, is that the properties of the piezo material may exhibit non-linear behavior due to hysteresis which may hamper the integrity of the obtained sensing signal, particularly at larger positioning ranges. Furthermore, while most of the contributions mentioned above are mainly concerned with compensation of the oscillations in the fast-scanning axis, mechanical cross-couplings in the piezoelectric tube can induce oscillations in the slow scanning axis as well. This becomes even more evident when image rotation is applied, as in that case the fast and slow scanning directions are not in line with the position axes of the piezoelectric tube scanner. Therefore, to prove the applicability of self-sensing actuation techniques in AFM imaging the following research question will be addressed:

Research Question:

Can self-sensing actuation be used to actively dampen the resonance modes of the scanning stage in AFM, in both scanning axes, over the whole scanning range of the instrument?

1.4.2 Accuracy of the topography estimate

The feedback loop in AFM controlling the tip-sample force is used to prevent damage and wear of the tip and sample during imaging, and to convert the tip-sample force measurement into an estimate of the sample topography. The demand for higher imaging speeds has motivated a vast amount of research focussed on increasing the bandwidth of this feedback loop, utilizing improved mechanical designs and modern model-based control techniques. However, the consequences of these higher control bandwidths on the accuracy of the topography estimate has not been investigated in much detail. In [80], [75] improved topography estimation is shown by taking into account a model of the dynamical behavior of the system. The dynamical behavior of the system, however, may show variations when changing the tip or sample, which limits the achievable modeling accuracy. Therefore, one of the questions to be addressed in this research is formulated as:

Research Question:

How does the dynamical uncertainty of the system influence the accuracy of the topography measurement, and how could this be addressed in the design of the mechatronic system and controller?

1.4.3 Dual actuated control of the tip-sample force

Dual actuated control of the tip-sample force has shown to be a promising method to allow a higher control bandwidth of the tip-sample force interaction without

compromising the effective positioning range. The control of such dual actuated AFM is more complex as compared to single actuated AFM. The feedback controller should control the tip-sample force via the two actuators, while preventing strong destructive interference between both actuators and coping with the limited positioning range of the short-range actuator. Moreover, in dual actuated AFM the sample topography estimation is more involved due to the additional actuator. Because the controller is an integral part of such dual actuated system, proper design of the controller requires a comprehensive analysis of the overall control system and its objectives. Therefore, developing a systematic approach to design the controller might significantly improve the performance of these systems, and might also provide valuable insight on the potential, limitations, and design trade-offs in dual actuated AFM. This could be used to formulate the design requirements for future high speed AFM designs. Therefore, the question to be answered in this research is:

Research Question:

What are the advantages and limitations of dual actuated control of the tip-sample force on the overall system performance, and how to systematically develop a controller for such an over-actuated system?

1.5 Approach

In order to answer the research questions raised above, a commercially available AFM system is used as a platform to develop and experimentally validate novel strategies to improve the imaging performance. In this research two commercially available AFM systems are used: the Multimode III and the Multimode V systems, both build by Bruker Nano Inc. (Santa Barbara, CA, USA). A photograph of the Multimode V system is shown in Figure 1.8. Both of these AFM systems are scanning sample systems. The system architecture of these Multimode systems is comparable with most AFM systems, such that the results obtained with these systems are transferable to most other AFM systems as well.

Within this research the mechanics, electronics, and control of these AFM systems are adapted in order to answer the research questions formulated above. Hereby a strong focuss is put on analyzing and improving the control of the imaging process in AFM. The controller part is the most flexible part of the AFM and is therefore usually designed based on the given hardware components. Focussing on the controller design allows to identify the performance limiting aspects of the system, and may provide valuable insights to redefine the design criterions for future AFM hardware components. Following such evolutionary design approach allows to continuously improve the performance of AFM systems, and mechatronic systems in general.

1.6 Outline

This thesis comprises three main parts, each addressing one of the research questions as formulated above. Chapter 2 discusses active damping of the lateral resonances of the scanning stage in AFM by means of self-sensing actuation. The influence of the dynamical uncertainty on the accuracy of the topography estimation is investigated in Chapter 3, and an integrated design methodology for the feedback controller and topography estimator is proposed and experimentally verified. In Chapter 4 the use of two actuators to control the tip-sample force is investigated, a control strategy for dual-actuated AFM is proposed, and the consequences of the dual actuators on the quality of the topography estimate is discussed. Conclusions, and recommendations are given in Chapter 5.

Active damping of the lateral scanner resonances by self-sensing actuation¹

During AFM imaging, the sample is scanned relative to the measurement tip in the lateral plane by use of a piezoelectric scanning stage in order to probe a certain region of interest. Excitation of the weakly damped resonances of the scanner by the scanning signals may result in strong oscillations in the scan-trajectory, which are a major source of image distortion, and limit the achievable imaging speed. In this chapter active damping of the resonant modes in both scan axes of a piezoelectric tube scanner is demonstrated, without the need for additional position sensors. By connecting the tube scanner in a capacitive bridge circuit, the scanner oscillations can be measured in both scanning axes, using the same piezo material as an actuator and sensor simultaneously. In order to compensate for circuit imbalance caused by hysteresis in the piezo element, an adaptive balancing circuit is used. The obtained measurement signal is used for feedback control, reducing the resonance peaks in both scanning axes by 18 dB and the cross-coupling at those frequencies by 30 dB. Experimental results demonstrate a significant reduction in scanner oscillations when applying the typical triangular scanning signals, over the entire working range of the instrument. Recorded AFM images show a considerable reduction in image distortion due to the proposed control method, enabling artifact free AFM imaging at a speed of 122 lines per second with a standard piezoelectric tube scanner.

2.1 Introduction

In order to probe a certain area of interest, in AFM imaging the sample is scanned relative to the measurement tip in the lateral plane utilizing a piezoelectric scan-

¹Parts of this chapter are also published in [50,49,51,52]

ning stage. For most AFM systems this scanning motion can be decomposed into a fast triangular scanning motion in the 'fast scanning axis', and a slow triangular scanning motion in the 'slow scanning axis', which allow a constant lateral tip-sample velocity during the recording of the sample profile.

The demand for high speed AFM imaging requires that the speed of the lateral scanning motion is increased. However, a strong limitation on the achievable imaging speed is posed by the weakly damped resonances within the piezoelectric scanning stages. These weakly damped resonances may induce strong oscillation in the scan trajectory when excited by the scanning signals, which is a major source of image distortion in AFM imaging [17,83]. To prevent excitation of these oscillations the line scan rate is limited to about 1% of the scanners fundamental resonance frequency [36].

In literature several methods can be found to compensate for the scanner oscillations, which can be subdivided in feedforward and feedback control methods [19, 14]. With feedforward techniques the input signal is shaped such that the scanner resonances are not excited, which result in a significant enhancement of the achievable scan speed [17,83,56,85]. Feedforward methods, however, do not apply direct damping to the scanners resonant modes, such that these may still be excited by environmental noise, or via the cross-talk with the z-axis of the scanner which tracks the unknown sample profile. Furthermore, the performance obtained with feedforward methods is relatively sensitive for changes of the system dynamics, occurring for instance when changing the sample mass resulting in a shift of the resonance frequency [83].

Alternatively, feedback control methods [95, 74, 89] can be applied to actively dampen the lateral scanner resonances. The major advantage of these feedback control methods is that these can account for unknown disturbances, and generally provide better performance robustness against variations in the dynamical behavior of the scanner. However, as conventional feedback control methods require the use of position sensors, e.g. capacitive or optical, application of feedback control is cost-intensive, and difficult to integrate within the existing scanner hardware.

Using the piezo material it self as a sensor and actuator simultaneously has been investigated within the smart-structure community [20], which is usually referred to as 'self-sensing actuation', and may eliminate the need for dedicated position sensors. Recently similar work has been done on piezoelectric tube scanners [31], by connecting a shunt impedance in parallel with the scan-electrodes, which significantly reduces the scanner oscillations.

A difficulty for the practical implementation of the self-sensing actuation principle on piezoelectric positioning stages, is that the properties of the piezo material may exhibits non-linear behavior due to hysteresis which may hamper the integrity of the obtained sensing signal, particularly at larger positioning ranges. Furthermore, while most of the contributions mentioned above are mainly concerned with compensation of the oscillations in the fast-scanning axis, mechanical cross-couplings in the piezoelectric tube can induce oscillations in the slow scanning axis as well. This becomes even more evident when image rotation is applied, as in that case the fast and slow scanning directions are not in line with the position axes of the piezoelectric tube scanner. Therefore, to address these issues, this chapter is fo-

cussed on the development of a method to use the principle of self-sensing actuation to dampen the lateral resonances of a piezoelectric scanning stage, in both scanning axes and over the entire positioning range of the instrument.

In this research a Multimode III system (Bruker Nano Inc., Santa Barbara, USA) is used as a platform to develop and test the self-sensing actuation and control techniques. This system is equipped with a piezoelectric tube-scanner ('E-scanner') to allow positioning of the sample in all three spatial directions with a positioning range of $10 \times 10 \times 2.5 \mu\text{m}$ (x-y-z), equivalent to the one depicted in Figure 2.1. The architecture of this piezo based scanning stage is equivalent to most piezoelectric scanners used in AFM imaging, such that the techniques developed on this system may easily translate to other piezo-based AFM imaging systems as well.

The principle of self-sensing actuation, and the implementation of the self-sensing bridge circuitry on both scanning axes of a piezoelectric tube-scanner is discussed in Section 2.2. In Section 2.3 an adaptive bridge-circuit balancing technique is introduced which guarantees the integrity of the measurement signals under influence of component mismatch and hysteresis in the piezo elements. Based on the obtained measurement signals, active damping of the scanner resonances by feedback control is shown in Section 2.4, and the implementation of this controller is discussed in Section 2.5. The active damping of the scanners lateral resonance modes is demonstrated experimentally in Section 2.6, in both line-scan experiments, as well as AFM imaging experiments.

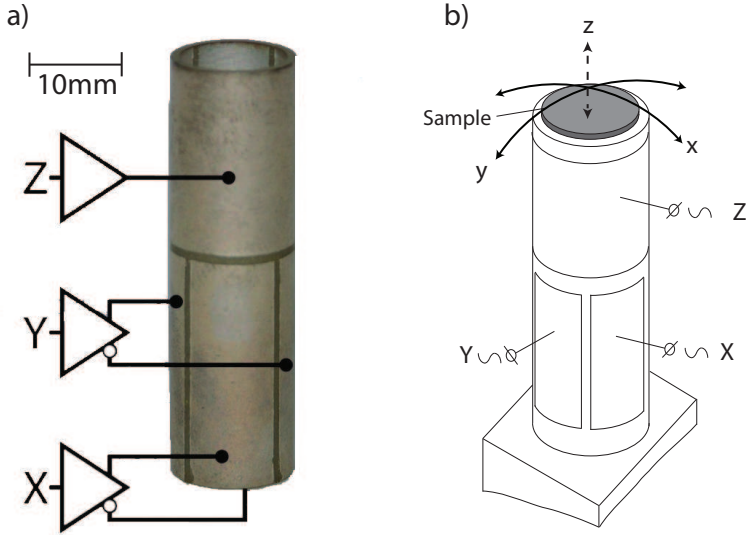


Figure 2.1: Example of an piezoelectric tubescanner (a), and a schematic description of the actuation principle (b). The tube scanners consist of a tube of piezoelectric material with segmented electrodes on the side. To provide the lateral scanning motion, a voltage is applied over the 'X' and 'Y' electrodes on the bottom which induces a bending motion of the tube, and consequently a translational motion of the sample placed on top of the tube.

2.2 Self-sensing actuation

Using a piezo-element both as an actuator and sensor simultaneously was first described in [20], by connecting the piezo-electric actuator in a bridge circuit along with three reference capacitors, as shown in Figure 2.2. In this section first the principles of self-sensing actuation is explained in Section 2.2.1 via the derivation of a first principles model. This model is experimentally validated in Section 2.2.2, by implementation of the self-sensing bridge circuitry on one scanning axis of the piezoelectric tube-scanner. In Section 2.2.3 it is presented how the self-sensing bridge circuitry can be extended to allow self-sensing actuation of both scanning axes of the piezoelectric tube scanner.

2.2.1 First principles modeling of self-sensing actuation

In this section the principle of self-sensing bridge circuitry of Figure 2.2 is explained by analytically deriving the frequency responses from the input signal $u_i(t)$ towards the actuator displacement $x(t)$, and the measurement signal obtained from the bridge circuit $u_m(t)$. For the analysis the assumption is made that the piezo is driving a mass M , which is significantly larger than the mass of

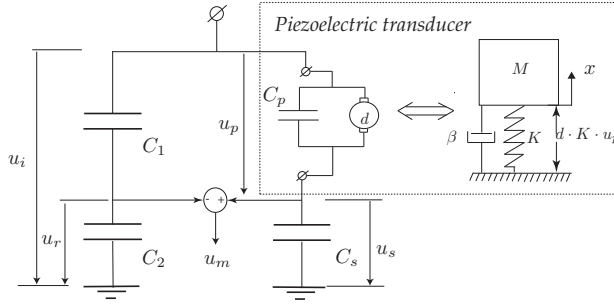


Figure 2.2: Scheme of self-sensing piezo-actuation, the capacitance ratios are chosen as $C_P/C_s = C_1/C_2$.

the piezo itself, i.e. M can be modeled as a lumped mass attached to the end of the piezo. The damping coefficient of the mechanical structure is denoted β in Figure 2.2. As will be experimentally verified later on in this section, the resulting second order model nicely describes the dynamics of one scanning axis of the piezoelectric tube-scanner considered in this work within the frequency range up to 10 kHz.

A piezoelectric element is a transducer, transferring energy from the electrical to mechanical domain and vice versa by the following relations [62]:

$$\begin{bmatrix} x(t) \\ q(t) \end{bmatrix} = \begin{bmatrix} K^{-1} & d \\ d & C_p \end{bmatrix} \begin{bmatrix} f_p(t) \\ u_p(t) \end{bmatrix}, \quad (2.1)$$

with displacement $x(t)$, mechanical stiffness K , charge $q(t)$, piezoelectric constant d , external force $f_p(t)$, capacitance C_p , and piezo voltage $u_p(t)$.

Force $f_p(t)$ is the force acting on the piezo element, which given the previous assumptions is proportional to sum of the acceleration and damping forces; $f_p = -M \frac{\partial^2 x(t)}{\partial t^2} - \beta \frac{\partial x(t)}{\partial t} = -M \ddot{x}(t) - \beta \dot{x}(t)$. Substituting this into Equation (2.1) leads to the following differential equation:

$$f_p(t) = -M \ddot{x}(t) - \beta \dot{x}(t) = K (x(t) - d \cdot u_p(t)). \quad (2.2)$$

The voltage over the piezo $u_p(t)$ can be derived from the second row of Equation (2.1) as

$$u_p(t) = \frac{1}{C_p} (q(t) - d \cdot f_p(t)). \quad (2.3)$$

Comparing Equations (2.2) and (2.3) shows that these are coupled. It is this coupling between the mechanical and electrical domain that enables self-sensing actuation. In order to derive the dynamical behavior of the piezo actuator connected in the bridge circuit, first the Laplace-transform of Equation (2.2) is taken:

$$\begin{aligned} F_p(s) &= -(Ms^2 + \beta s)X(s) = K (X(s) - d \cdot U_p(s)), \\ X(s) &= \frac{d \cdot K}{Ms^2 + \beta s + K} \cdot U_p(s), \end{aligned} \quad (2.4)$$

$$F_p(s) = -d \cdot K \frac{Ms^2 + \beta s}{Ms^2 + \beta s + K} \cdot U_p(s) = -d \cdot K \frac{s^2 + \nu s}{s^2 + \nu s + \omega_n^2} \cdot U_p(s), \quad (2.5)$$

with $\nu = M^{-1}\beta$, and $\omega_n = \sqrt{M^{-1}K}$ the natural eigenfrequency of the piezo element with unconnected electrodes. Substitution of Equation (2.5) in Equation (2.3) leads to:

$$\begin{aligned} U_p(s) &= \frac{Q(s)}{C_p} + \frac{d^2 K}{C_p} \cdot \frac{s^2 + \nu s}{s^2 + \nu s + \omega_n^2} \cdot U_p(s) \\ &= \frac{1}{C_p \left(1 - k^2 \frac{s^2 + \nu s}{s^2 + \nu s + \omega_n^2}\right)} \cdot Q(s), \end{aligned} \quad (2.6)$$

with $k = \sqrt{C_p^{-1}d^2K}$, which is also known as the Electromechanical coupling factor [62]. Notice that if $k = 0$ the piezo behaves like a normal capacitor according to Equation (2.6).

The relation between the charge $q(t)$ and the input voltage over the bridge-circuit $u_i(t)$ can be derived as $q(t) = C_s \cdot u_s(t) = C_s (u_i(t) - u_p(t))$, where C_s and $u_s(t)$ are the capacitance and voltage over the capacitor that is in series with the piezo element (see Figure 2.2). This leads to:

$$\begin{aligned} U_p(s) &= \frac{C_s}{C_p \left(1 - k^2 \frac{s^2 + \nu s}{s^2 + \nu s + \omega_n^2}\right)} \cdot (U_i(s) - U_p(s)) \\ &= \frac{1}{1 - k^2 + r} \cdot \frac{r \cdot (s^2 + \nu s + \omega_n^2)}{s^2 + \nu s + \omega_n^2 \cdot \frac{1+r}{1-k^2+r}} \cdot U_i(s), \end{aligned} \quad (2.7)$$

with $r = C_p^{-1}C_s$ the capacitance ratio. From Equations (2.7) and (2.4) the transfer function from input voltage $U_i(s)$ toward the actuator displacement $X(s)$ can be derived as:

$$\begin{aligned} G_x(s) = \frac{X(s)}{U_i(s)} &= \frac{1}{1 - k^2 + r} \cdot \frac{r \cdot (s^2 + \nu s + \omega_n^2)}{s^2 + \nu s + \omega_n^2 \cdot \frac{1+r}{1-k^2+r}} \cdot \frac{d \cdot \omega_n^2}{s^2 + \nu s + \omega_n^2} \\ &= \frac{1}{1 - k^2 + r} \cdot \frac{r \cdot d \cdot \omega_n^2}{s^2 + \nu s + \omega_n^2 \cdot \frac{1+r}{1-k^2+r}}. \end{aligned} \quad (2.8)$$

Notice that the mechanical eigenfrequency of the piezo connected in the bridge-circuit now depends on the coupling factor k and the capacitance ratio r .

The purpose of the self-sensing bridge configuration is to measure the mechanical oscillations at the measurement output voltage $u_m(t) = u_s(t) - u_r(t)$ of the bridge-circuit. The voltage $u_s(t)$ can be derived as $u_s(t) = u_i(t) - u_p(t)$, which with substitution of Equation (2.7) leads to the transfer function from input voltage $U_i(s)$ towards the voltage $U_s(s)$:

$$G_s(s) = \frac{U_s(s)}{U_i(s)} = \left(1 - \frac{1}{1 - k^2 + r} \cdot \frac{r \cdot (s^2 + \nu s + \omega_n^2)}{s^2 + \nu s + \omega_n^2 \cdot \frac{1+r}{1-k^2+r}}\right)$$

$$= \frac{1}{1 - k^2 + r} \cdot \frac{(1 - k^2) \cdot (s^2 + \nu s) + \omega_n^2}{s^2 + \nu s + \omega_n^2 \cdot \frac{1+r}{1-k^2+r}}. \quad (2.9)$$

The voltage $u_r(t)$ is measured over capacitor C_2 of the left branch of the bridge-circuit (Figure 2.2). Because the capacitor ratios in both branches are chosen equal, this voltage is given as: $u_r(t) = C_1 \cdot (C_1 + C_2)^{-1} \cdot u_i(t) = (1 + r)^{-1} \cdot u_i(t)$. With this expression and Equation (2.9), the transfer function from input voltage $U_i(s)$ towards the measurement voltage $U_m(s)$ is given as:

$$\begin{aligned} U_m(s) &= U_s(s) - U_r(s) \\ G_m(s) = \frac{U_m(s)}{U_i(s)} &= \frac{1}{1 - k^2 + r} \cdot \frac{(1 - k^2) \cdot (s^2 + \nu s) + \omega_n^2}{s^2 + \nu s + \omega_n^2 \cdot \frac{1+r}{1-k^2+r}} - \frac{1}{1 + r} \\ &= \frac{1}{1 - k^2 + r} \cdot \frac{-k^2 \cdot r}{1 + r} \cdot \frac{s^2 + \nu s}{s^2 + \nu s + \omega_n^2 \cdot \frac{1+r}{1-k^2+r}}. \end{aligned} \quad (2.10)$$

Now based on Equation (2.8) and Equation (2.10) the relation between the actuator displacement $X(s)$, and the measurement signal from the bridge circuitry $U_m(s)$ can be derived:

$$\frac{U_m(s)}{X(s)} = \frac{U_m(s)}{U_i(s)} \cdot \frac{U_i(s)}{X(s)} = \frac{-k^2}{(1 + r) \cdot d \cdot \omega_n^2} \cdot (s^2 + \nu s). \quad (2.11)$$

i.e. for low intrinsic damping or high frequencies $\omega \gg \nu$, the measurement voltage $u_m(t)$ is proportional to the second derivative of the displacement, or the acceleration of the mass.

Given the derived frequency responses the system can be represented by the block-diagram shown in Figure 2.3, with $G_x(s) = \frac{X(s)}{U_i(s)}$, $G_s(s) = \frac{U_s(s)}{U_i(s)}$, and $G_m(s) = \frac{U_m(s)}{U_i(s)}$, i.e. the transfer functions of Equations (2.8), (2.9), and (2.10), respectively. Block A in Figure 2.3 denotes the gain of the high voltage amplifier, and signal $R(s)$ the applied reference signal. In the next section the analytically derived frequency responses are experimentally validated by implementing the self-sensing bridge circuitry on a single scanning axis of the piezoelectric tube scanner.

2.2.2 Self-sensing actuation of a single scanning axis

To validate the first principles model derived above, the self-sensing actuation circuit is implemented on one scanning axis of the piezoelectric tube scanner (E-scanner). Technical details about the practical implementation of the bridge-circuitry can be found in Section 2.5.

Figure 2.4 shows the frequency responses from input signal $U_i(s)$ towards the actuator displacement $X(s)$, towards voltage over the capacitor in series with the piezo element $U_s(s)$, and towards the measurement voltage over the bridge circuit $U_m(s)$. The frequency response of the actuator displacement is measured with a vibrometer (Polytec, Karlsruhe, Germany), and clearly reveals the scanners fundamental resonance mode at about 3 kHz.

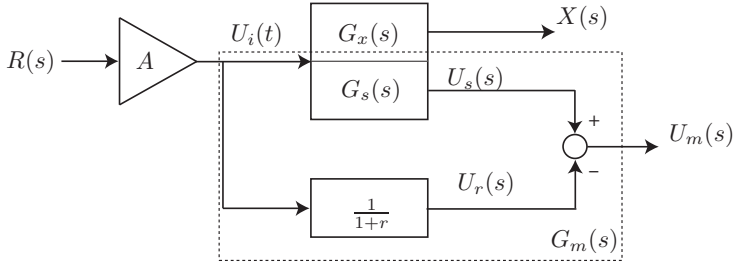


Figure 2.3: Blockdiagram of the self-sensing actuation with transfer functions $G_x(s)$, $G_s(s)$, and $G_m(s)$ according to Equations (2.8), (2.9), and (2.10), respectively. Block A denotes the gain of the high voltage amplifier, and $R(s)$ is the applied reference signal.

From this system the following parameters are known:

$$A = 25, \quad r = \frac{C_s}{C_p} = \frac{C_2}{C_1} = \frac{56nF}{4nF} = 14, \quad d = 40[\text{nm/V}].$$

Based on the measured frequency responses shown in Figure 2.4 (solid lines) and the transfer functions derived earlier, the following parameters are identified:

$$\omega_n = 1.8 \cdot 10^4[\text{rad/s}], \quad \nu = 1.07 \cdot 10^3[\text{s}^{-1}], \quad k=0.16.$$

The transfer functions based on the first principles model and the identified parameters are plotted in dashed lines in Figures 2.4a-c. These modeled frequency responses show some mismatch with the actual frequency responses on higher frequencies, which may be due to the amplifier roll-off and higher order modes of the tube scanner that are not taken into account in the model. Figure 2.4c shows that the DC gain of the actual measurement output differs from zero, as suggested by Equation (2.10). This is due to small impedance mismatches between both branches of the bridge-circuit, resulting in slight phase variations. For higher frequencies however, the measured frequency responses match well with the modeled frequency response of Equation (2.10), confirming that the first principles model derived above largely explains the dynamical behavior of the system.

The results of Figure 2.4c clearly demonstrates that the measurement signal obtained from the self-sensing bridge circuitry allows to measure the mechanical scanner resonances at about 3 kHz, and therefore may be used as an input for a feedback controller to allow active damping of this resonance mode. Moreover, comparing Figures 2.4a and c reveals that the frequency response of the measurement signal $\frac{U_m(\omega)}{U_i(\omega)}$ shows a quasi second order derivative with respect to the frequency response of the actuator displacement $\frac{X(\omega)}{U_i(\omega)}$, as also explained by Equation (2.11). Notice that the fundamental resonance frequency of 3 kHz is also visible in the frequency response of the voltage over the capacitor in series with the piezo element $\frac{U_s(\omega)}{U_i(\omega)}$ (see Fig. 2.4b). However, the zero pair appearing directly after the resonance frequency renders this mode almost un-observable, and therefore difficult to control by feedback based on $U_s(s)$. By subtraction of the voltage from the other branch of the bridge circuit $U_m(\omega) = U_s(\omega) - U_r(\omega)$ (cf. Fig. 2.2) this zero pair is shifted towards the origin, resulting in a clearly observable resonance mode in the frequency response towards $\frac{U_m(\omega)}{U_i(\omega)}$ (see Fig. 2.4c), which can be used

for controlling this mode by feedback control.

2.2.3 Self-sensing actuation of both scanning axes

To allow self-sensing actuation in both scanning axes of the piezoelectric tube-scanner, the bridge circuitry of Figure 2.2 is implemented on both scanning axes of the piezoelectric tubescanner, according to the scheme in Figure 2.5. A detailed description on the electronic implementation of this circuit, including buffer amplifiers is given in Section 2.5. Figure 2.6 show the frequency responses from the input signals towards the lateral scanner displacements measured with a vibrometer (Polytec, Waldbronn, Germany), and the frequency responses of the measurement signals obtained from the self-sensing bridge circuitry. The weakly damped fundamental resonances at 3 kHz can clearly be observed in the frequency responses of the measured scanner displacement, both in the direct responses as well as in the cross-coupling. Figure 2.6 shows that these scanner resonances can be clearly resolved in the responses of the measurement signals from the self-sensing bridge circuitry as well. However, as can be seen in Figure 2.6 (grey lines), the measurement signals show a strong cross-coupling over all frequencies which is not observed in the responses of the displacement recorded with the vibrometer. This cross-talk is caused by the large parasitic coupling capacitances within the piezoelectric tube, which are denoted C_c in Figure 2.5. This capacitive coupling is stemming from the fact that the electrodes of both individual scanning axes are located closely to each other on the same piezoelectric tube (cf. Fig. 2.1). By measuring the capacitances between the adjacent electrodes on the piezoelectric tube the coupling capacitances are determined to be about 0.4 nF, which amounts to 10% of the capacitances of the active piezo segments, measured to be about 4 nF. This capacitive coupling causes a direct electric feed-through of the driving voltage from one axis towards the measurement signal of the other axis, resulting in a large cross-talk as observed by the grey lines in the off-diagonal response of the measurements signals in Figure 2.6.

The capacitive cross-talk in the piezoelectric tube scanner is compensated for by using two additional capacitors, denoted C_{V_y} and C_{V_x} in Figure 2.5. These variable capacitors are tuned such that they cancel out the cross-talk of the driving voltage of the X- and Y-axis towards the measurement signals, reducing the coupling in the measurement signals up to 30 dB, as clearly can be seen in the frequency responses of the measurement signals in Figure 2.6 (black lines). After compensation, a strong coupling in the measurement signals is only observed in the frequency regions of the mechanical resonances of the tube, which are a true mechanical couplings, as also observed in the vibrometer measured displacement. As will be discussed in Section 2.4, the electrical decoupling of the measurements signals allows for decoupled control for active damping of the resonances based on the obtained measurement signals, instead of requiring the more complex MIMO control techniques, this simplifies the controller design and enables a low-cost analog implementation of the feedback controller for active damping of the resonance modes.

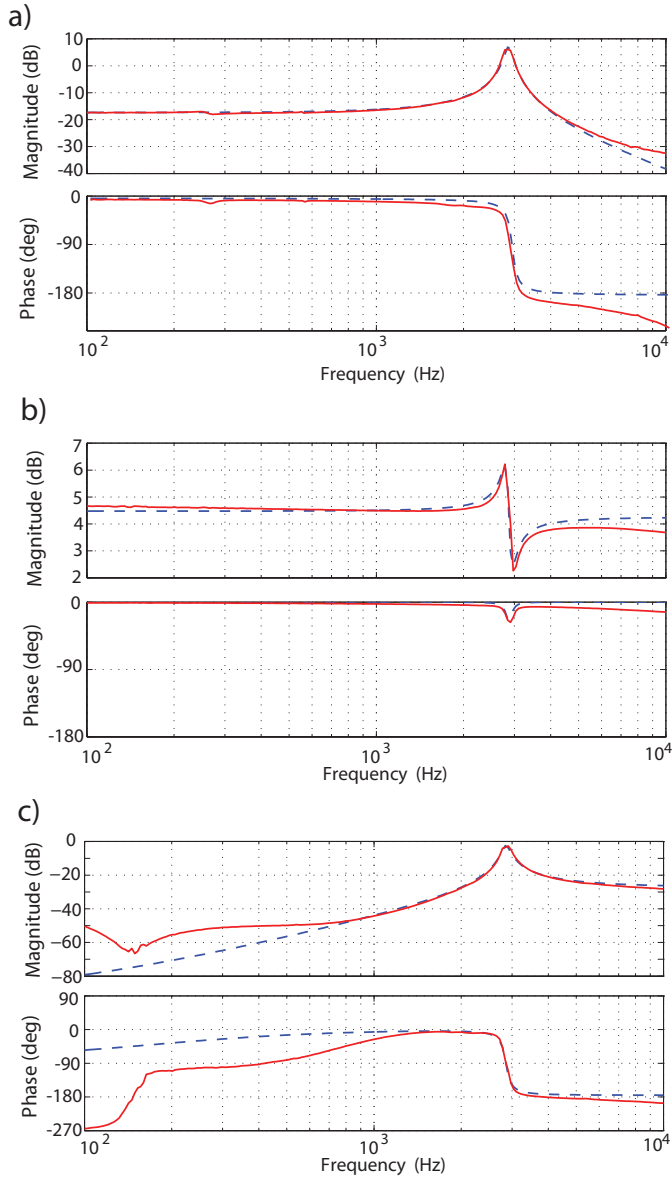


Figure 2.4: Measured (solid lines) and modeled (dashed lines) frequency responses from input signal $R(s)$ towards (a) the actuator displacement $X(s)$ (measured with a vibrometer), (b) the voltage over capacitor in series with piezo $G_s(s)$, and (c) the bridge-circuit output voltage $G_m(s)$.

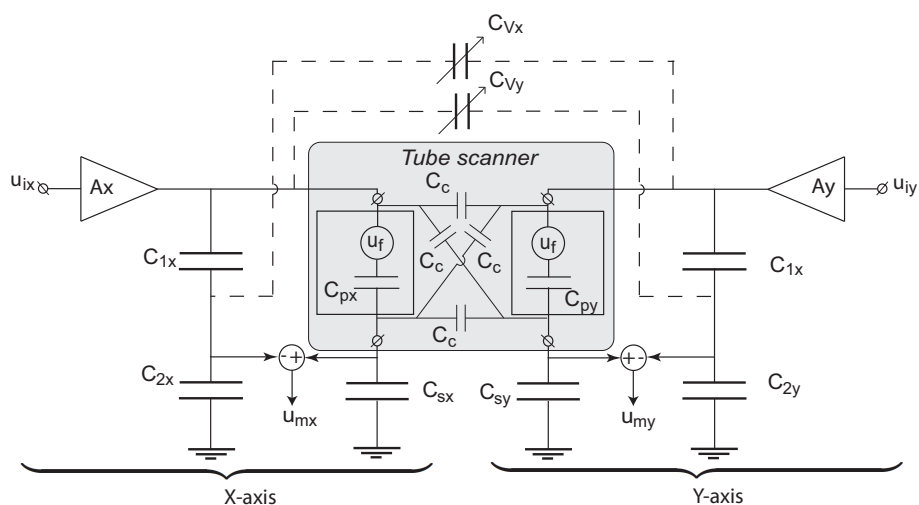


Figure 2.5: Scheme of the self-sensing actuation circuit for both scanning axes of a piezoelectric tube scanner. The external forces on the piezo element generate a voltage $u_f = \frac{d}{C_p} \cdot f_p(t)$.

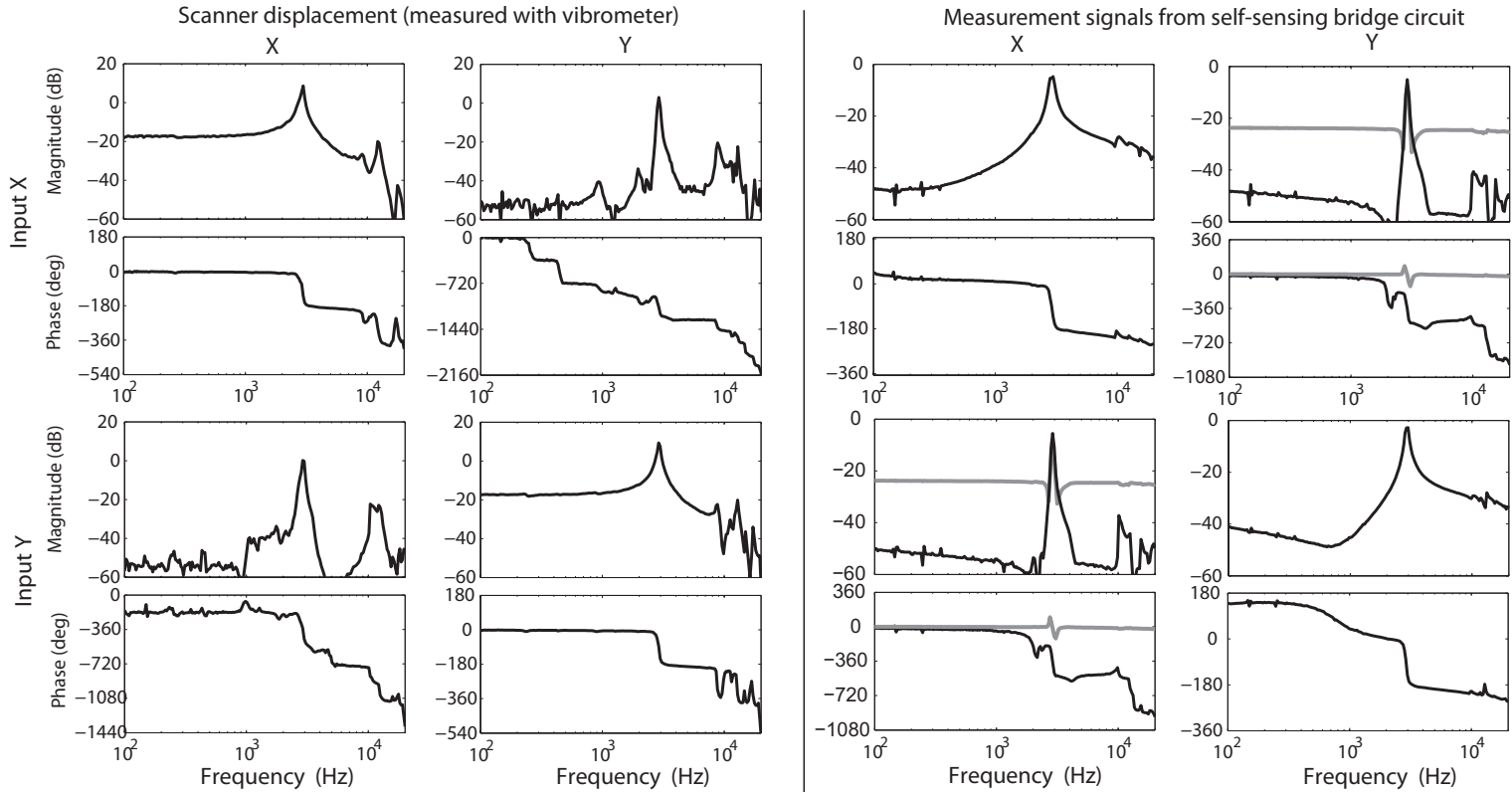


Figure 2.6: Frequency response plots from input signals towards the scanner displacement measured with a vibrometer (left two columns), and the measurement signals obtained from the self-sensing bridge-circuit (right two columns). The grey lines in the off-diagonal responses of the self-sensing measurement signals show the responses before compensating for the capacitive coupling between both axes, and the responses after compensation are shown by the black lines.

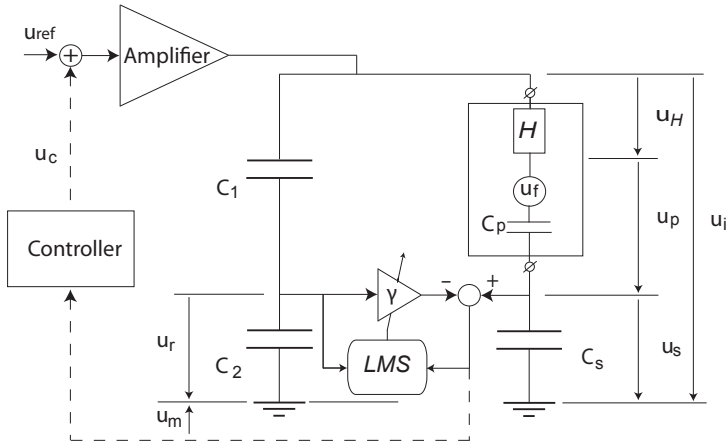


Figure 2.7: Scheme of capacitive bridge circuit for self-sensing piezo actuation with adaptive circuit balancing and feedback controller (one axis). The external forces on the piezo element generate a voltage $u_f = \frac{d}{C_p} \cdot f_p(t)$. The hysteresis within the piezo element is modeled as a non-linear impedance which is in series with the 'ideal' piezo element.

2.3 Bridge circuit imbalance compensation

While the frequency responses shown in Figure 2.6 are captured with small amplitudes excitation signals, for larger amplitude signals the piezoelectric tube scanner suffers from hysteresis which influences the responses of the scanner displacement and the measurement signals. If not accounted for, the hysteresis within the piezoelectric tube scanner can cause an imbalance in the self-sensing bridge circuit which may affect the integrity of the self-sensing signal. In this section the influence of the hysteresis induced bridge circuit imbalance is analyzed, and an adaptive balancing technique is demonstrated to compensate for these effects.

2.3.1 Hysteresis induced bridge circuit imbalance

As discussed in [33], the hysteresis within a piezoelectric element occurs as a non-linear relation between the voltage $u_p(t)$ over the piezoelectric element and the resulting charge $q(t)$. The hysteresis can therefore be modeled as a non-linear impedance which is in series with the 'ideal' piezo element [1] as shown in the bridge circuit of Figure 2.7. As no hysteresis is present in the reference capacitors of the bridge circuit, an imbalance in the bridge circuit is introduced, resulting in a differential voltage over the bridge circuit that is depending on the hysteresis induced voltage drop $u_H(t)$ over the piezo-element. As shown by Figure 2.7, due the hysteresis the voltage over the capacitor in series with the piezoelement now

becomes:

$$u_s(t) = u_i(t) - u_p(t) - u_{\mathcal{H}}(t). \quad (2.12)$$

In most AFM setups the loss in position accuracy due to the hysteresis is compensated in open loop by calibrated feedforward compensation, as discussed in Section 1.3.1. In order not to interfere with the scanner calibration, feeding back the hysteresis induced voltage drop $u_{\mathcal{H}}(t)$ should be avoided when using the measurement signals for the self-sensing bridge circuit as input for the feedback controller for active damping of the scanner resonances.

To analyze the hysteresis induced imbalance in the bridge circuit, the voltage $u_s(t)$ over the capacitor C_s (cf. Fig. 2.7) is measured as a function of the input voltage $u_i(t)$ over the bridge circuit. Figure 2.8 shows the response for two 20 Hz triangular reference signals at an amplitude of 80 V_{pp} and 400 V_{pp}. These measurements show that the hysteresis not only causes a curved response, but also a varying peak to peak gain for the different driving amplitudes, as is apparent from the different slopes of the hysteresis curves. In the graph of Figure 2.9 (solid line) the measured peak to peak gain is shown for different driving amplitudes, showing a variation of around 30% from the smallest (30 V_{pp}) to the largest (440 V_{pp}) driving voltage amplitudes. Therefore, the major part of the hysteresis induced voltage $u_{\mathcal{H}}(t)$ in the measurement signal $u_m(t)$ can be canceled by compensating for this variation in the peak-to-peak gain. This can be done by adding an additional gain γ to the bridge circuitry to re-balance the two branches of the bridge circuit, as depicted in Figure 2.7. Hence, the measurement voltage over the bridge circuit is now given by:

$$u_m(t) = u_s(t) - \gamma \cdot u_r(t) \quad (2.13)$$

The gain value γ may be adapted to optimally balance the bridge circuitry for the applied driving signals, which comes down to minimizing energy of the measurement signal $u_m(t)$, as will be shown in Section 2.3.2.

Figure 2.10 shows the vibrometer measurement of the scanner displacement in response to a 80 Hz triangular reference signal, and the resulting measurement signal from the self-sensing bridge circuit in the uncompensated case (grey line), and when compensating for the gain variation by balancing the bridge via the additional gain γ (black line). In the uncompensated case, large low-frequency components are visible in the self-sensing signal, which are not explained by the linearized frequency responses of Figure 2.6, but stemming from the imbalance in the bridge circuit due to the non-linear hysteresis within the actuator. In the compensated case (Fig. 2.10, black lines), the low-frequency components in the self-sensing signal are significantly reduced by compensating for the bridge circuit imbalance via γ . Because adaptation of the gain γ only compensates for the variation of the peak-to-peak gain due to hysteresis, residual components stemming from the curvature of the hysteresis loops (cf. Fig. 2.8) can still be observed in the self-sensing signal, which are predominantly in the frequency range of the line scan rate. However, as the goal of the self-sensing bridge circuitry is to dampen the high frequency oscillations stemming from the fundamental resonance modes, which are typically a factor 30 to 100 higher than the fastest line scan rate, the residual low frequency components stemming from the hysteresis can be easily

eliminated by high-pass filtering. This high-pass filtering is eventually integrated within the feedback controller as discussed in Section 2.4. Especially for the larger scan-ranges the obtained reduction in circuit imbalance due to the gain adaptation via γ is found to be vital to avoid interference with the scanner calibration when using the measurement signal for feedback control, as is demonstrated experimentally in Section 2.6.

To guarantee optimal circuit balancing over all scan-ranges and at all time, the adjustment of balancing gain γ is automated, as described in the following subsection.

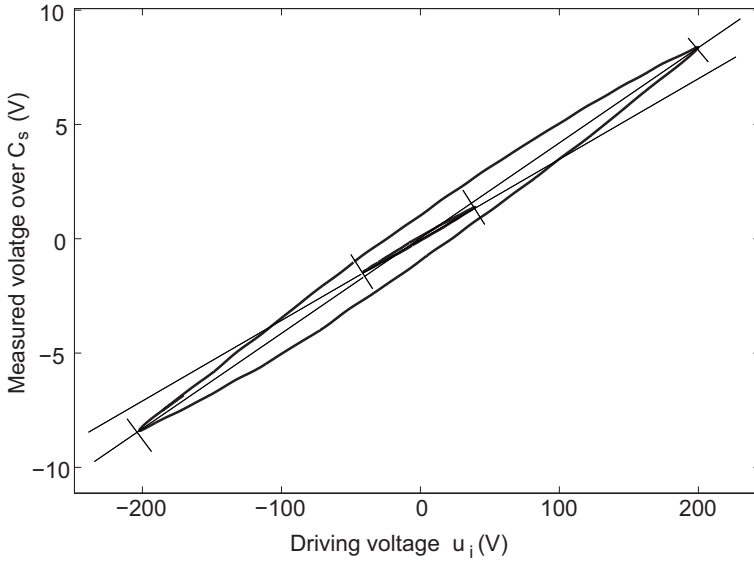


Figure 2.8: Measured voltage $u_s(t)$ over capacitor C_s in series with piezo to a 80 V_{pp} and a 400 V_{pp} driving voltage $u_i(t)$. The straight lines illustrate the difference in peak-to-peak gain for the different driving voltage amplitudes.

2.3.2 Automated bridge circuit balancing

Automated compensation of possible imbalance of the self-sensing bridge circuit due to component mismatch, or change of piezo-capacitance C_p , caused by aging or temperature drift, has been discussed in literature by adaptation of the gain value γ [15, 103]. The adaptive gain value $\gamma(t)$ is hereby minimizing the Least Mean Square (LMS) estimate of the measurement signal $\gamma(t) = \arg \min_{\gamma} (E[u_m^2(t)])$, which is equivalent as minimizing the energy of the measurement signal. In this section it is shown that such an adaptation method can also be used to compensate for the varying peak-to-peak gain caused by the hysteresis of the piezo element when the scanning axes are following the typical triangular

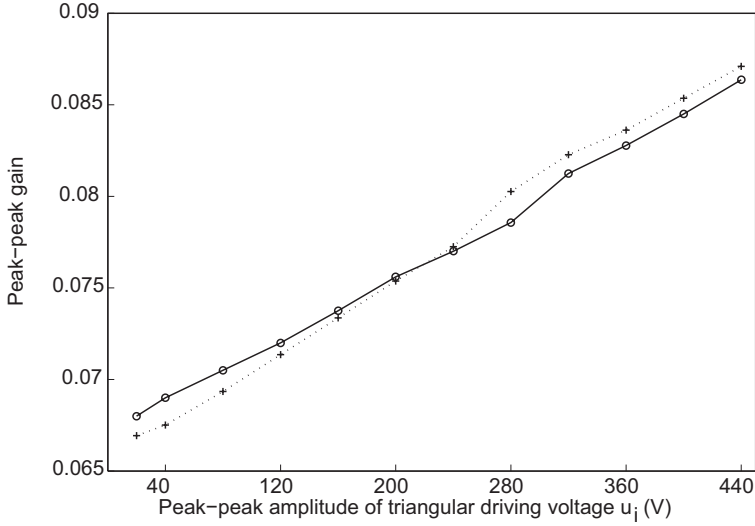


Figure 2.9: Peak-to-peak gain u_s/u_i (solid) and $\gamma \cdot u_r/u_i$ (dashed) for different amplitudes of triangular driving voltages, showing that the gain γ adapts to the gain difference in u_s/u_i for all input ranges.

scanning signals, as used in AFM. The update law for $\gamma(t)$ is hereby taken as

$$\gamma(t) = \gamma_0 + \gamma_a(t) = \gamma_0 + \frac{\mu}{2} \int \frac{\partial J(t)}{\partial \gamma_a(t)} dt, \quad (2.14)$$

where γ_0 is the initially set gain value, and $\gamma_a(t)$ is the adaptive gain value. The gain value γ_0 is tuned such that it minimizes the feed-through for the linearized system (i.e. for small amplitudes). The factor μ is the learning gain which determines the convergence speed and stability of the adaptation. $J(t)$ is the cost function to be minimized by the adaptation, which is chosen as

$$J(t) = [u_m(t)]^2 - \rho[\gamma_a(t)]^2, \quad (2.15)$$

with $u_m(t)$ according to Equation (2.13), and factor ρ which is denoted the 'forgetting gain' which function is described below. Taking the derivative of $J(t)$ with respect to $\gamma_a(t)$ leads to

$$\frac{\partial J(t)}{\partial \gamma_a(t)} = -(2 \cdot u_m(t) \cdot u_r(t) + 2 \cdot \rho \cdot \gamma_a(t)), \quad (2.16)$$

where $u_r(t)$ is the voltage measured over capacitor C_2 (cf. Fig 2.7). Substitution in Equation (2.14) gives

$$\gamma(t) = \gamma_0 - \mu \int (u_m(t) \cdot u_r(t) + \rho \cdot \gamma_a(t)) dt. \quad (2.17)$$

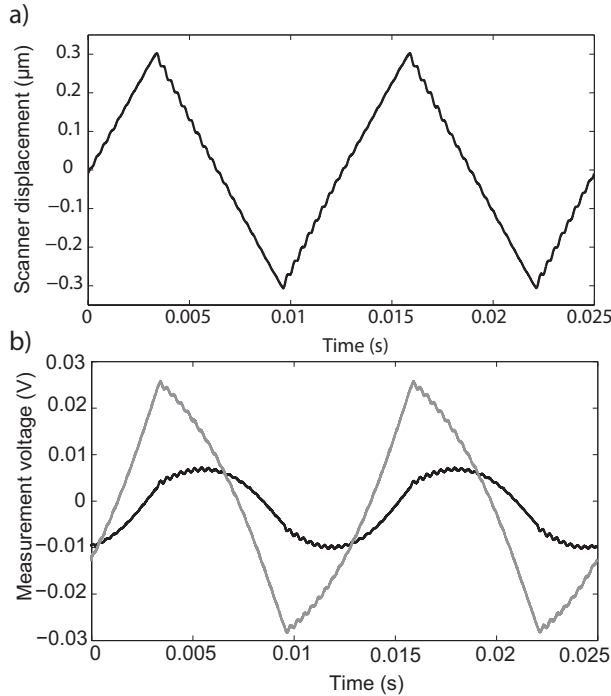


Figure 2.10: Response of the system to a 80-Hz triangular reference signal (X-axis only). Graph (a) shows the scanner displacement measured with a vibrometer, while graphs (b) show the measurement signal from the bridge-circuit, without (grey) and with (black) adaptive balancing of the bridge-circuit. The major part of the hysteresis induced voltage in the self-sensing measurement signal is compensated by the gain adaptation.

Equation (2.17) shows that at zero input signal ($u_r(t) = 0$), the term $\rho \cdot \gamma_a(t)$ is the only term within the integral. The previously learned gain $\gamma_a(t)$ will therefore converge back to zero, hence the term 'forgetting factor' for ρ . This addition to the adaptation algorithms described in [15, 103] causes $\gamma(t)$ to converge more rapidly towards γ_0 when changing to a smaller input signal and prevents drifting of $\gamma_a(t)$ when no input signal is applied.

The LMS-based adaptive circuit balancing is implemented on both scanning axes via analog electronics, as discussed in more detail in Section 2.5. Figure 2.9 shows the measured peak-to-peak gain variation in $u_s(t)$ for a low-frequency triangular input signal with varying amplitudes, demonstrating that $u_r(t) \cdot \gamma(t)$ is able to track this gain variation (dashed), to compensate the hysteresis induced imbalance in the bridge circuit. The learning gain μ is set such that when changing the scan-range the adaptable gain $\gamma_a(t)$ converges within about 3 seconds. The learning rate should, however, not be set too high in order to avoid undesirable interference between the LMS-based gain adaptation and the actual feedback control for active damping of the resonant modes.

2.4 Controller design

After compensating for the possible bridge circuit imbalance, the obtained measurement signals of the self-sensing bridge circuit can be used for feedback control to allow active damping of the weakly damped resonances of the piezoelectric tube scanner. Figure 2.7 (dashed lines) shows the control structure of this control method for one scan axis. Although the tube scanner is a MIMO system with two inputs (X and Y) and two self-sensing channels, the frequency responses of the measurement signals are largely decoupled due to compensation of the capacitive cross-talks between both axes, as discussed in Section 2.2. This decoupling allows the use of two decoupled controllers instead of requiring a full MIMO controller, which reduces the complexity of the controller. The residual coupling at 3 kHz stemming from the actual mechanical resonances of the system is initially not considered within the design of the decoupled controllers. However, the remaining coupling at 3 kHz eventually does not pose any stability issues for the designed controllers and significant damping of the resonances is also achieved in the couplings, as discussed further below. Furthermore, due to the symmetry of the tube scanner, the frequency responses of both axes are largely similar which allows using identical SISO controllers for both scanning axes.

The primary goal of the feedback controller is to actively dampen the lateral scanner resonances at 3 kHz, as observed in both scanning axes (cf. Fig. 2.6). Recall that within the frequency region of the resonance modes the measurement signal obtained from the bridge circuit is proportional to the negative acceleration of the scanner, as derived from the first principle model in Equation (2.11), and also revealed in Figures 2.4, and 2.6. Hence, an integrating action within this frequency region will lead to a signal which is proportional to the negative velocity of the scanner, which by high gain, positive feedback control results in damping of the resonance modes. Therefore, the controller is required to have a high gain integral action in the frequency region of the resonance modes, (i.e. providing a phase lag of 90 degrees), and the feedback sign is taken positive as shown in Figure 2.7.

An important aspect for the design of the feedback controller is that it should provide sufficient attenuation at lower frequencies, in order to suppress any residual low-frequency components in the measurement signal stemming from the hysteresis induced voltage drop over the piezo $u_H(t)$ (cf. Fig. 2.10). Feeding back the components in the measurement signal stemming from the hysteresis should be avoided in order not to interfere with the calibration of the setup where the loss in position accuracy due to the hysteresis is compensated for in an open-loop manner, as discussed in Section 1.3.1. Moreover, the feedback controller should provide sufficient high frequency roll-off to prevent instability of the system due to higher order modes of the system. Hence, a selective feedback controller is required, only applying a high feedback gain in the frequency region of the first lateral resonance modes of the scanner. An additional advantage of such selective feedback control approach is that the feedback of any potential measurement noise is minimal, such that the precision of the instrument is hardly affected by feeding back sensor noise [88]. Therefore, the controller is chosen as a 4th order

bandpass filter with the following transfer function:

$$C(s) = \alpha \cdot \frac{s^2}{(s^2 + 2\zeta \cdot \omega_c \cdot s + \omega_c^2)^2}, \quad (2.18)$$

where α is a gain factor, and ζ and ω_c are the damping and corner frequency of both the high-pass and low-pass action of the bandpass filter. The controller is tuned such that it provides a phase lag of 90° degrees at the resonance frequency of the tube scanner, which resulted in $\omega_c = 7400$ [rad/s]. The damping of the controller poles is set to $\zeta = 1$ in order to smoothen the phase decay of the controller, adding some robustness to variations in the tube scanner resonance frequencies.

The controllers are implemented as analog circuits, as discussed in Section 2.5. Figure 2.11 shows the measured frequency responses of the loop-gains of both scanning axes. The bandpass characteristics of the controllers can be clearly recognized, only applying a high feedback gain in the frequency region of the mechanical resonances of the tube scanner at 3 kHz. As can be seen, the phase of the loop gain is largely between $+90^\circ$ and -90° at the frequencies where the gain exceeds the 0 dB-line, resulting in a stable and well damped closed loop system. Figure 2.12 shows the frequency response of the scanner displacement measured with a vibrometer, in the uncontrolled case (grey) and with the active damping by the proposed feedback scheme (black). It clearly shows the significant reduction of the resonance peaks in both scanning axes by 18 dB, and the reduction in cross-coupling at these frequencies of about 30 dB.

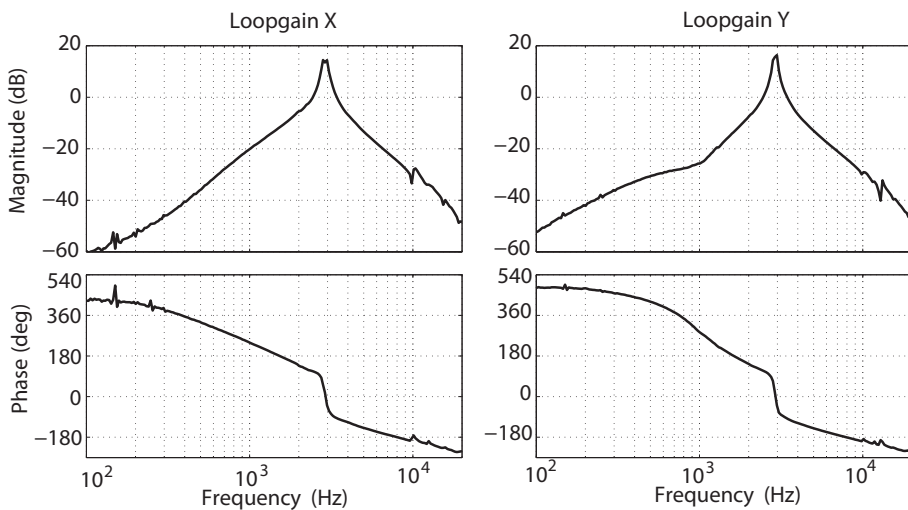


Figure 2.11: Frequency responses of the loop-gains of the X-axis and the Y-axis.

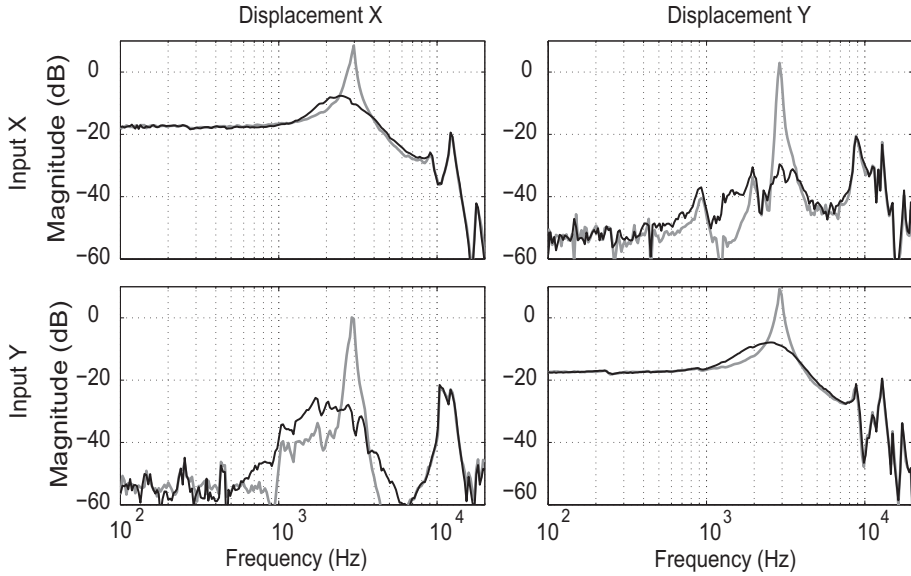


Figure 2.12: Frequency response plot of the tube scanner displacement measured with a vibrometer, uncontrolled (grey) and controlled (black).

2.5 Implementation

The proposed control method is implemented by analog electronics as shown for one axis in Figure 2.13. As for the implementation only analog electronics are used, the use of expensive digital signal processors is omitted. The implementation of the proposed control method therefore only requires a low-cost modification of the electronics of the conventional AFM system, and leaves all other hardware unchanged.

The bridge circuit, as discussed in Section 2.2, is implemented using additional resistors in parallel with the capacitors in order to prevent drift due to the finite input impedance of the buffer amplifier measuring the voltages over capacitors C_s and C_2 . The resistor values are chosen such that the resulting time constants $\tau = \frac{1}{R_p \cdot C_p}$ of the capacitor-resistor pairs are equal for the entire bridge circuit. The high voltage amplifier, denoted A_{HV} in Figure 2.13, is a dual channel, single ended amplifier (PZD700, Trek, Medina, USA). Variable capacitors C_{V_x} and C_{V_y} are used to compensate for the capacitive coupling between the two scanning axes, as discussed in Section 2.2.

The *LMS*-based adaptive circuit balancing, described in Section 2.3, is implemented using two multipliers (AD633) and one operational amplifier (OP27). The nominal gain value γ_0 of the adaptation (cf. Section 2.3) is set using the variable resistor R_{V_1} , the forgetting factor ρ using the variable resistor R_{V_2} , and the learning gain μ using the variable resistor R_{V_3} .

The feedback controller is implemented using two operational amplifiers (OP27), where the overall feedback gain is set using the variable resistor R_{V_5} . A switch

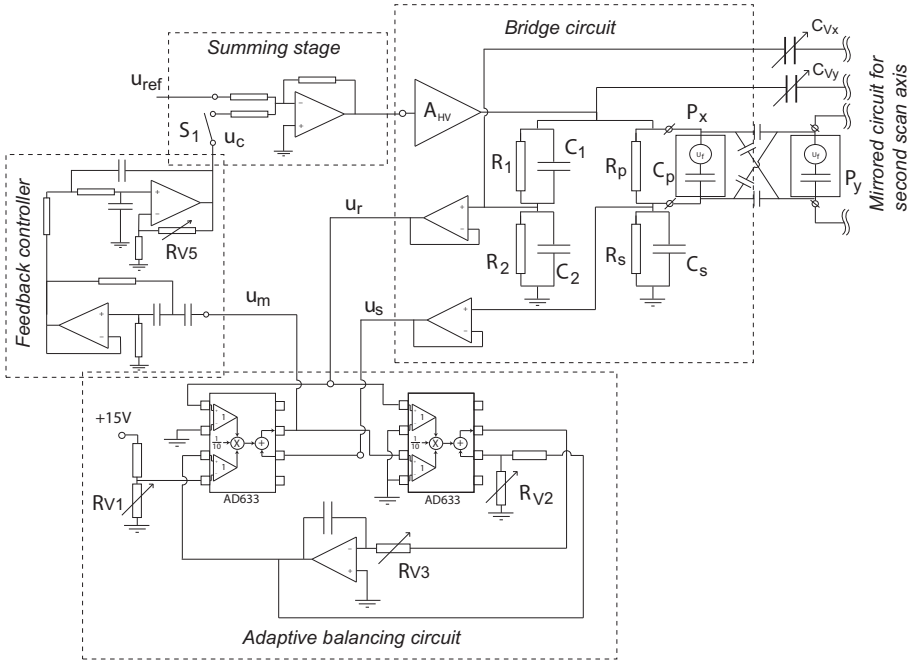


Figure 2.13: Analog implementation of self-sensing actuation and control of a piezoelectric tube scanner of one scanning axis. Switch S_1 open corresponds to the uncontrolled case, and S_1 closed corresponds to the actively damped case.

S_1 is used to enable and disable the active damping. A summing stage, implemented using one operational amplifier (OP27), adds the reference signal $u_{ref}(t)$ and control signal $u_c(t)$ forming the input signal for the high voltage amplifier.

2.6 Experiments

In order to demonstrate the improved system performance by the proposed control method, the system response to triangular reference signals of different amplitudes and frequencies is measured. These triangular scanning signals are typically used for the scanning motion in AFM imaging, aimed to achieve in a constant velocity between the tip and the sample while the sample profile is recorded. Moreover, AFM images are recorded to show the reduction in image distortion.

2.6.1 Line-scan experiments

To determine the reduction in scanner oscillations due to the proposed control method, the systems response is measured when scanning with a triangular reference signal at varying scan-frequencies and amplitudes. These triangular scan-

ning signals are generated via a signal generator, and therefore do not include the additional feedforward compensation for the loss in positioning accuracy due to of the hysteresis, which is normally present during actual AFM imaging. The results are shown in Figure 2.14 for scanning in the X-axis at a line-scan frequency of 60 Hz (a,c,e,g) and 120 Hz (b,d,f,h), and a driving voltage amplitudes of $50 V_{pp}$ (a,b), $200 V_{pp}$ (c,d) and $500 V_{pp}$ (e,f), respectively. Also the response of the unactuated Y-axis is shown while scanning the X-axis with a $200 V_{pp}$ driving voltage (g,h).

Each sets of graphs shows the scanner displacement $x(t)$ and velocity $v_x(t)$ measured with a vibrometer, the measurement signal from the bridge circuit $u_m(t)$ and the output signal of the controller $u_c(t)$. In each set of graphs the response of the system is shown for the uncontrolled case (red), where the feedback loop is disconnected via switch S_1 (cf. Fig. 2.13), and for the controlled case (blue), i.e. with active damping of the resonances in both scanning axes.

In the uncontrolled cases (red), the oscillations of the scanner are visible in the displacement and velocity signal, as well as in the measurement signal. These oscillations last over the entire scan-line for both scanning speeds. In the actively damped cases, the oscillations significantly reduced, only occurring at the begin of the scan line where the scanning motion is reversed.

In Figure 2.14 (g,h) the responses of the system is shown in the unactuated Y-axis, while the X-axis is driven by a $200 V_{pp}$ triangular reference signal of 60 Hz (g) and 120 Hz (h). In the uncontrolled case the coupling induced oscillations are clearly visible, while in the controlled case these oscillations are significantly reduced.

Although an adaptive circuit balancing techniques is used to compensate for most of the bridge circuit imbalance caused by the hysteresis (cf. Section 2.3), the measurement signal still contains small residual low-frequency components as is visible in Figure 2.14 (c-f). As discussed in Section 2.3, feeding back these low-frequency components in the measurement signal should be avoided in order not to interfere with the scanner calibration. Although the controllers have strong high-pass characteristics, a small part of the low-frequency components in the measurements signals still enter the control signals as can be seen in Figure 2.14 (c-f). This effect becomes more prominent for the larger scan-ranges and at higher scan-frequency. For the smaller scan-ranges a small jump can be observed in the control signal only at the beginning of each line scan (a,b), whereas for the larger scan-range (e,f) the low-frequency components in the control signal last over the whole line scan. Nevertheless, in all cases the scanner oscillations are significantly reduced by the proposed control method as compared to the uncontrolled tube scanner, enabling AFM imaging at high speeds.

2.6.2 AFM-imaging

To demonstrate the improvement in image-quality, AFM-images of a 476 nm line-pitch calibration grating are obtained with the uncontrolled and the actively damped tube scanner. In order to show the true benefit of controlling both axis of the tube scanner, the images shown in Figure 2.15 are obtained while scanning at an image rotation of 45° . Therefore, the reference signals $r_x(t)$ for the X-axis and

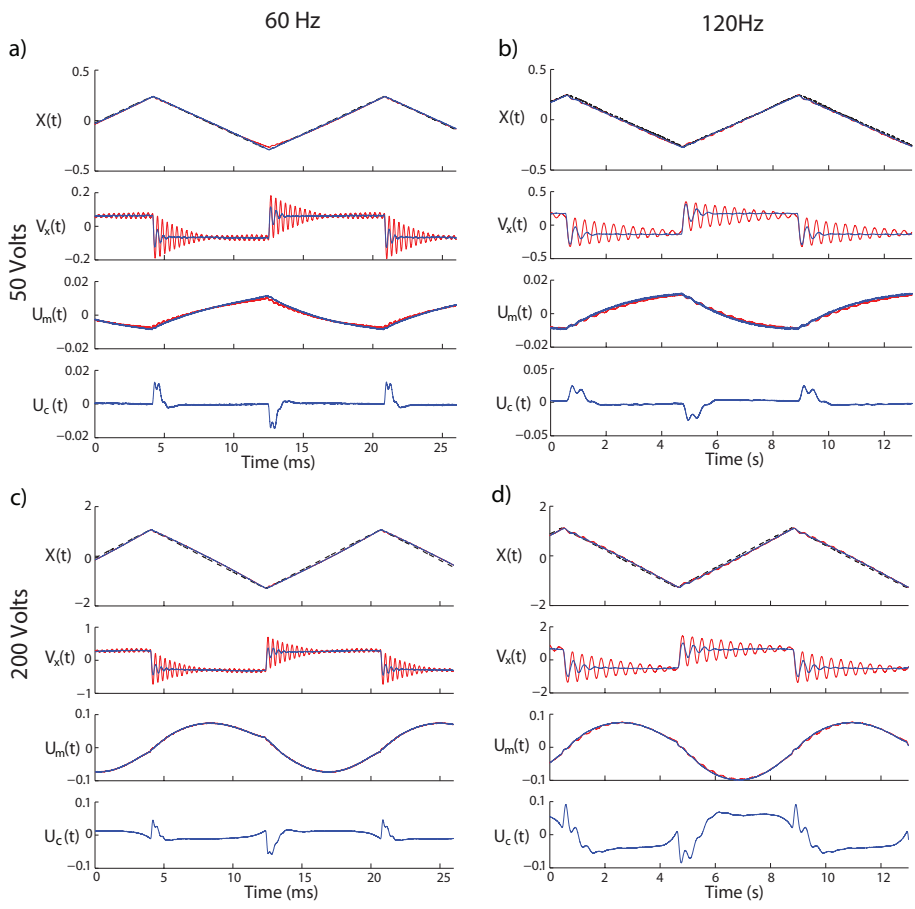
$r_y(t)$ Y-axis are given as:

$$\begin{aligned} r_x(t) &= \cos\left(\frac{\pi}{4}\right) \cdot r_f(t) - \sin\left(\frac{\pi}{4}\right) \cdot r_s(t), \\ r_y(t) &= \cos\left(\frac{\pi}{4}\right) \cdot r_f(t) + \sin\left(\frac{\pi}{4}\right) \cdot r_s(t), \end{aligned}$$

where $r_f(t)$ and $r_s(t)$ are the triangular signals for the fast and slow scanning axis respectively. Note that due to the image rotation the reference signals of both axes are a summation of two triangular signals of different frequency, corresponding to the 122 Hz line scan rate ($r_f(t)$), and the 0.24 Hz frame rate ($r_s(t)$). As discussed in Section 2.3, the compensation for the peak to peak gain variation due to the hysteresis only works for pure triangular reference signals. Note, however, that the triangular reference signal for the slow scanning axis is at such low frequency that any hysteresis induced imbalance in the bridge circuit due to this low-frequency reference signal will be effectively attenuated by the high pass characteristic of the controller. Therefore, it is sufficient to let the adaptive circuit balancing only learn the peak to peak gain variation due to the fast triangular reference signal $r_f(t)$. This peak to peak gain variation appears to be largely independent to any offsets. Therefore, when scanning at an image rotation first the optimal adaptive gain γ_a is learned for the fast triangular reference signal by the *LMS*-adaptation and then fixed, before applying the slow triangular reference signal $r_s(t)$ to the system.

The resulting images are shown in Figure 2.15 for the uncontrolled and controlled cases. The fast scanning direction corresponds to the horizontal orientation of the images, where the left side is the beginning of each scan-line. In the uncontrolled case (a-c), the image-distortion caused by the scanner oscillations can be clearly recognized by the non-straightness of the grid-lines (a and b) which occurs throughout the whole images. Also in the friction image (c) vertical lines can be observed which are a result of the non-constant tip-velocity over the sample caused by the scanner oscillations [83].

In the controlled case (d-f), only a slight image distortion is visible at the beginning of each scan-line (left part of the images), and the vertical lines in the friction image due to variations in the scanning speed are disappeared. This clearly demonstrates that the image quality is significantly improved by the proposed control method when capturing AFM images at high speeds.



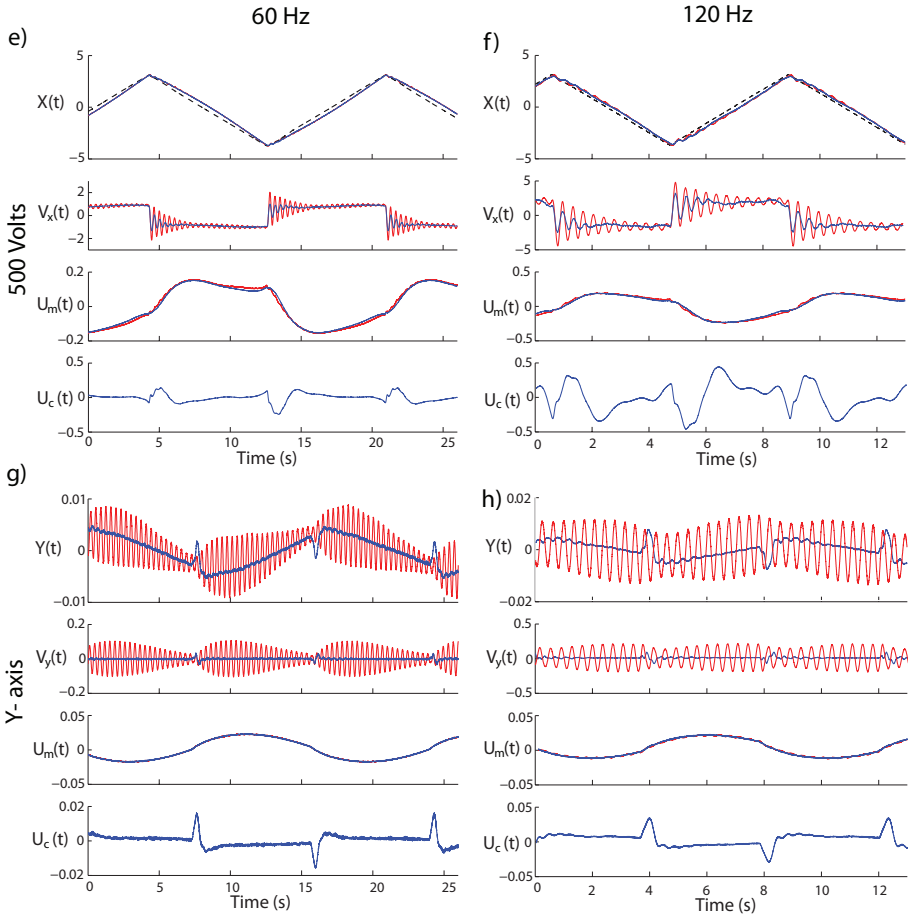


Figure 2.14: Outputs of the self-sensing piezoelectric tube scanner as a response to a triangular driving signal in the x-direction of 60 Hz (left) and 120 Hz (right) of varying amplitudes. Each set of graphs shows the scanner displacement $x(t)$ [μm], scanner velocity $V_x(t)$ [mm/s], measurement signal from bridge circuit $u_m(t)$ [V] and control signal from the controller $u_c(t)$ in the uncontrolled case (blue) and with active damping in both scanning axes (red). The lower sets of graphs shows the uncontrolled and actively damped response in the unactuated Y-axis, while driving the X-axis with a 200 Volts triangular driving signal of 60 Hz and 120 Hz.

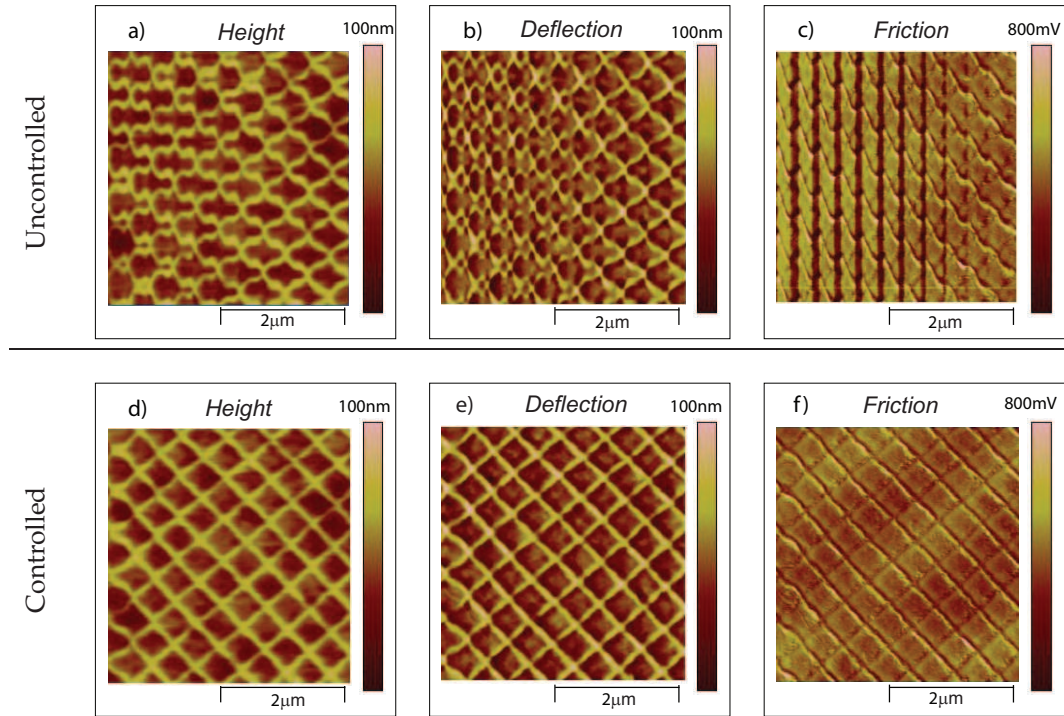


Figure 2.15: AFM images of a calibration grid with line pitch of 476 nm, scanned with at an image rotation 45° and at a line-scan speed of 122 Hz. The resolution of the images is 256×256 pixels. The upper images (a-c) are captured with the uncontrolled system, while the bottom images (d-f) are captured using the proposed control method for active damping of the tube scanner.

2.7 Conclusions

In this chapter active damping of the mechanical resonances of a piezoelectric tube scanner is demonstrated in both scanning axes via self-sensing actuation. By connecting the scanning axes of the tube scanner in two coupled capacitive bridge circuits, the scanner oscillations in both scanning axes can be measured, without the need for dedicated position sensors. Compensation of hysteresis induced imbalance in the bridge circuits is demonstrated by adapting a variable balancing gain for each line scan amplitude, which is automated by a *LMS*-based adaptation circuit. Using the obtained measurement signals for feedback control enables active damping of the mechanical resonances of the tube scanner with up to 18 dB, and a damping of the mechanical coupling at these frequencies by 30 dB. Experimental results verify a significant reduction of scanner oscillations when applying the typical triangular scanning signals to the scanner, resulting in a significant reduction in image distortion when using the controlled tube scanner for AFM-imaging. Implementation of the proposed control method only requires a small modification of the AFM electronics and leaves all other AFM hardware unchanged. Therefore, the proposed self-sensing actuation, and control method is a very cost efficient way of adding damping to the mechanical resonances of the tube scanner for AFM-imaging and other scanning probe systems.

Although in this research only piezoelectric tube scanners are considered, the proposed method may also be applied to other positioning stages, for instance in high bandwidth flexure stages utilizing piezoelectric stack actuators. Implementation of this control method on piezoelectric stack actuators would be easier as capacitive coupling between the individual actuators is not present and therefore does not have to be dealt with in the bridge circuitry.

Tip-sample force control and topography estimation²

In AFM the tip-sample force is controlled in a feedback loop to prevent damage of the tip and sample during imaging, and to convert the measurement of the tip-sample force into an estimate of the sample topography. Dynamical uncertainties of the system pose a strong limitation on the achievable control bandwidth, and on the accuracy of the topography estimation. This chapter presents an integrated approach to design a robust feedback controller and topography estimator, taking into account the dynamical uncertainties of the imaging system. The proposed methodology is demonstrated on a commercially available AFM system, showing a direct trade-off between the closed-loop control bandwidth and the accuracy of the topography estimation due to the dynamic uncertainties in the system. This design trade-off is experimentally verified by comparing the performance of the designed feedback controllers and topography estimators on the physical AFM system.

3.1 Introduction

In AFM the sample topography is measured by probing the sample with the measurement tip and scanning the sample relative to the tip in a lateral scanning pattern. During imaging the force between the tip and the sample is controlled in a feedback loop to prevent the tip-sample force from becoming too high in order not to cause damage to the tip and the sample. Figure 3.1 shows a block diagram of the feedback loop in AFM controlling the tip-sample force, with the actuator dynamics G , the sensor dynamics B , and the feedback controller K . While scanning, the sample topography enters the feedback loop as an unknown disturbance signal, denoted $h(t)$ in Figure 3.1. Signal $n(t)$ in Figure 3.1 denotes

²Parts of this chapter are also published in [54,55]

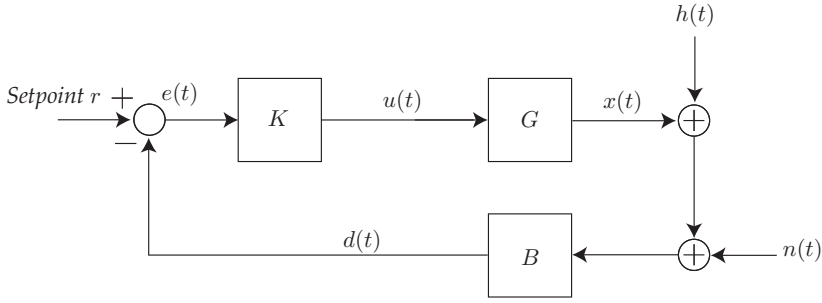


Figure 3.1: Block diagram of the feedback loop controlling the tip sample force in an AFM system, with actuator dynamics G , sensor dynamics B , and feedback controller K , topography signal $h(t)$, cantilever deflection signal $d(t)$, controller output $u(t)$, and noise signal $n(t)$.

the noise and disturbances acting on the system, which may be stemming from various sources, such as electronic noise from the sensor electronics and power amplifier, vibrations stemming from the environment, temperature drifts within the instrument, and Brownian noise observable from the small cantilever [76]. Although stemming from various sources, these noise contributions can be viewed as a signal entering the feedback loop at the same location as the sample topography signal $h(t)$.

During imaging, the feedback controller is aimed to minimize the variations of the tip-sample force with respect to the constant setpoint level r , in some sense minimizing the control error $e(t) = r - d(t)$. Based on the compensating actions of the feedback loop an estimate $\hat{h}(t)$ of the sample topography is obtained, of which the quality can be judged by the topography estimation error $\epsilon(t) = \hat{h}(t) - h(t)$.

In high accuracy metrological AFM-systems, the sample topography is estimated by directly measuring the actuator displacement $x(t)$ with high accuracy displacement sensors (e.g. interferometric) [63,98], aimed to trace back the measured sample dimensions towards the international length standards. When assuming that the feedback loop is fast enough to track the sample topography variations while scanning (i.e. $e(t) \approx 0$), the measurement of the actuator displacement can be regarded as a direct measure of the sample topography: $\hat{h}(t) = -\bar{x}(t)$, with $\bar{x}(t)$ the measured actuator displacement.

For most AFM systems the requirements on the accuracy are not as high as in metrological AFM, and the use of high accuracy displacement sensors to measure the actuator displacement is considered not very cost-efficient. Moreover, the sensor noise of the position sensors may degrade the measurement precision, which becomes more severe at higher imaging bandwidths, as with high-speed AFM. Therefore, in most AFM-systems the sample topography is approximated by taking a calibrated scaling of the control signal $u(t)$, assuming that the controller output is directly proportional to the actuator displacement, and the control error is small: $\hat{h} = -\hat{x}(t) \propto u(t)$ [24].

Although taking a calibrated scaling of the control signal $u(t)$ allows for low noise, and thus precise estimation of the sample topography, the accuracy of this

approach is limited due to the fact that the actuator dynamics are neglected. For instance, due to possible hysteresis within the piezoelectric actuator the relation between the control signal $u(t)$ and the actuator displacement $x(t)$ may not be fully linear, limiting the accuracy of the topography estimate if not accounted for. Therefore, in [28] improved topography estimation is shown by compensating for the actuator hysteresis, utilizing charge control. Also methods have been developed to compensate for the non-linearity of hysteresis in AFM by inverse hysteresis models [17, 63]. Furthermore, when increasing the bandwidth of the feedback loop, also the higher frequency resonances within the actuator dynamics are excited, which influence the accuracy of the topography estimation if not accounted for. In [80] a method is discussed to improve the accuracy of the topography estimate by simulating the sample profile based on a model of the higher order actuator dynamics: $\hat{h}(t) = -\hat{x}(t) = -\hat{G}(p)u(t)$, with \hat{G} a model of the actuator dynamics, and $p = \frac{d}{dt}$ the differential operator. To compensate for the influence of environmental disturbances on the topography estimation, in [82] a method is presented to measure and subtract the vibration induced image distortions from the image by using a capacitive sensor mounted in parallel with the piezo-actuator.

The assumption that the actuator displacement $x(t)$ directly represents the sample topography only holds when scanning relatively slow, allowing the feedback control loop sufficient time to recover from topography variations such that the control error is almost zero: ($e(t) \approx 0 \rightarrow h(t) \approx -x(t)$). However, at higher imaging speeds the control error is not fully zero, and part of the topography information will appear in the cantilever deflection signal $d(t)$. Therefore, most often the cantilever deflection signal $d(t)$ is presented in a separate image to reveal the sample topography variations that occur faster than the control bandwidth of the feedback loop during imaging [24]. In [75] a method is presented to design a model based controller and estimator that provides an estimate of the sample topography by directly taking into account the cantilever deflection signal and a model of the system dynamics, allowing high bandwidth topography estimation. In [57] this method is extended to dynamic mode imaging, taking into account a linear model of the tip sample interaction.

In order to improve the imaging speed of AFM, a vast amount of research is dedicated to improving the control bandwidth of the feedback loop that controls the tip-sample force, utilizing modern model-based control methods [84,75], and improved mechanical design of the positioning stages [5,79,46,29]. However, when increasing the control bandwidth in AFM imaging, also the topography estimation becomes a highly dynamical process in which the higher order dynamics of the instrument may start to influence the instruments accuracy. An important aspect that needs to be considered in this context is that the dynamical behavior of the system may show variations due to the varying weight and alignment of the sample and cantilever, and due to the varying imaging conditions. As these dynamical variations are largely unpredictable, these constitute a certain degree of dynamical uncertainty which limits the modeling accuracy of the system dynamics, and thus of the ability of accurately estimating the sample topography. This becomes more relevant for high speed AFM applications in which the

bandwidth of the system is pushed to higher frequencies, leading to stronger excitation of the higher order dynamics of the system which typically constitute larger dynamical uncertainty. Therefore, in this chapter it is analyzed how the dynamical uncertainty of the system influences the accuracy of the topography estimate, and how this could be addressed in the design of the feedback controller and topography estimator.

In Section 3.2 the topography estimation problem in AFM is analyzed, and how this is influenced by dynamical uncertainty of the system and by the design of the feedback controller. In Section 3.3, an integrated design methodology is proposed in order to design a feedback controller and topography estimator to guarantee frequency domain performance specification on both the control error as well as the topography estimation error, given the dynamical uncertainty of the system. This integrated design methodology is demonstrated and verified for a commercially available AFM system in Section 3.4. In Section 3.5, the influence of the dynamical uncertainty on the accuracy of the topography is experimentally verified, while conclusions are drawn in Section 3.6.

3.2 Topography estimation problem

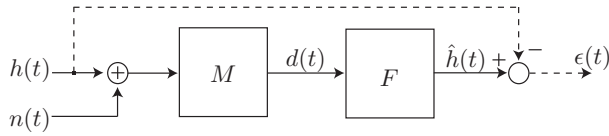


Figure 3.2: Block diagram depicting the topography estimation problem in AFM as a filtering problem based on sensor output $d(t)$.

In order to analyze the topography estimation problem in AFM, in this section the optimal topography estimator is derived based on the Wiener theory [102]. Based on the expression of the optimal topography estimator, it is analyzed how the topography estimation accuracy is influenced by the dynamical uncertainty of the system, and by the design of the feedback controller. While in most AFM systems the sample topography is estimated based on both the cantilever deflection signal $d(t)$ and the control signal $u(t)$, the later one can be directly derived from the first given that the feedback controller is known: $u(t) = K(p) \cdot d(t)$. Therefore without loss of generality the topography estimation problem can be posed as a filtering problem solely based on the cantilever deflection signal $d(t)$. Later on in this section the practical considerations are discussed which motivate the use of both available signals $u(t)$ and $d(t)$ for the topography estimation. Moreover, in the following analysis the setpoint is neglected as this is constant throughout each imaging experiments (i.e. $r = 0$). Hence, the topography estimation problem may be depicted as in the block diagram of Figure 3.2, with the system dynamics M and the topography estimator F . Notice that this topography estimator F is a form of a disturbance estimator, estimating an unknown input signal (distur-

bance) based on the available output signals [70, 86]. Assuming linear dynamics the sensor output in AFM is given as:

$$d(t) = \underbrace{\frac{B(p)}{1 + L(p)}}_{M(p)} \cdot (h(t) + n(t)), \quad (3.1)$$

with the loop gain $L(p) = G(p) \cdot K(p) \cdot B(p)$, and $p = \frac{d}{dt}$ the differential operator. The sensor signal $d(t)$ is the input for the sample topography estimator F which provides an estimate of the sample topography:

$$\hat{h}(t) = F(p) \cdot d(t), \quad (3.2)$$

The topography estimation error is now given as:

$$\varepsilon(t) = \hat{h}(t) - h(t) = F(p) \cdot d(t) - h(t), \quad (3.3)$$

The Mean Square Error value of this signal can be derived via the Parsevals theorem as:

$$\mathbf{E} [\varepsilon(t)^2] = \frac{1}{2\pi} \int_{-\infty}^{\infty} \Phi_{\varepsilon}(\omega) d\omega \quad (3.4)$$

with $\Phi_{\varepsilon}(\omega)$ the power spectral density of the topography estimation error signal, which is given as:

$$\Phi_{\varepsilon}(s) = F(s) \cdot F^*(-s) \cdot \Phi_d(s) - F(s) \cdot \Phi_{dh}(s) - F^*(-s) \cdot \Phi_{hd}(s) + \Phi_h(s). \quad (3.5)$$

By setting the derivative of $\Phi_{\varepsilon}(s)$ with respect to the estimator filter $F(s)$ to zero the following expression for the optimal Wiener filter can be obtained [102]:

$$F(s) = \frac{\Phi_{hd}(s)}{\Phi_d(s)} = \frac{M^*(-s)\Phi_h(s)}{M(s)M^*(-s)(\Phi_h(s) + \Phi_n(s))} = \underbrace{\frac{\Phi_h(s)}{\Phi_h(s) + \Phi_n(s)}}_{F_2(s)} \cdot \underbrace{\frac{1}{M(s)}}_{F_1(s)}, \quad (3.6)$$

in which the fact is used that the topography signal $h(t)$ and the noise signal $n(t)$ are not correlated. As shown by Equation (3.6) the optimal estimator can be split in a part that handles the noise denoted F_2 , and a part which inverts the system dynamics denoted F_1 . The spectrum of $h(t)$ is depending on the sample topography profile and the imaging speed, of which the first is not known beforehand and varies strongly between different experiments. Therefore, by splitting the design of the estimator, the part inverting the system dynamics F_1 needs to be designed only once, while the noise filter F_2 can be adjusted for the changing imaging conditions. The design and application of F_2 to filter out the measurement noise can be done after the imaging data is obtained and analyzed. Such filtering of the imaging data to filter out the (high frequency) noise is a common procedure during the post-processing of the AFM images [24].

While noise filtering via F_2 can improve the precision of the topography estimate,

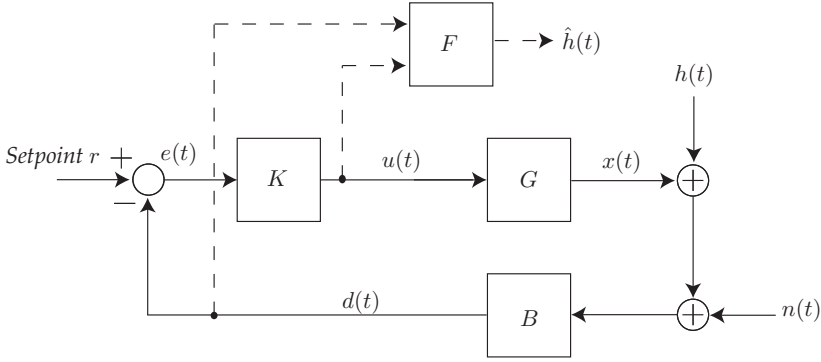


Figure 3.3: Block diagram of the feedback loop controlling the tip sample force in AFM with the topography estimator F , the which provides an estimate $\hat{h}(t)$ of the topography signal $h(t)$ based on sensor signal $d(t)$, and control signal $u(t)$.

proper inversion of the system dynamics M via F_1 is vital for accurate representation of the sample features, especially at faster imaging speeds at which the higher order dynamics of the system are excited. Based on Equations (3.1) and (3.6) the estimated sample topography based on the optimal Wiener filter can be written as:

$$\begin{aligned}
 \hat{h}(t) &= F_2(p) \cdot F_1(p) \cdot d(t) = F_2(p) \cdot \frac{1}{M(p)} \cdot d(t), \\
 &= F_2(p) \cdot \left[\hat{B}^{-1}(p) + \hat{G}(p) \cdot K(p) \right] \cdot d(t), \\
 &= F_2(p) \cdot \begin{bmatrix} \hat{B}^{-1}(p) & -\hat{G}(p) \end{bmatrix} \cdot \begin{bmatrix} 1 \\ -K(p) \end{bmatrix} \cdot d(t), \\
 &= F_2(p) \cdot \underbrace{\begin{bmatrix} \hat{B}^{-1}(p) & -\hat{G}(p) \end{bmatrix}}_{\hat{F}_1} \cdot \begin{bmatrix} d(t) \\ u(t) \end{bmatrix}, \tag{3.7}
 \end{aligned}$$

with \hat{G} and \hat{B} models of the actuator and sensor dynamics, respectively. The resulting topography estimator can be depicted as shown in Figure 3.3. Equation (3.7) shows that by taking the output of the feedback controller $u(t)$ into account in the topography estimate (as is also done in conventional AFM) the dynamics of the feedback K do not need to be taken into account in the topography estimator, which simplifies the design of the estimator. However, the resulting topography estimator does require dynamical models of the sensor dynamics \hat{B} and of the actuator dynamics \hat{G} in order to accurately represent the sample features, as shown by Equation (3.7).

In dynamic mode AFM, the cantilever dynamics in B are non-linear, making it difficult to model. Therefore, in dynamic mode AFM one strongly relies on the controller output $u(t)$ for estimation of the sample topography, presuming a good linearization effect of the feedback loop. Recently, however, techniques

are developed to explicitly handle the cantilever dynamics in dynamic mode AFM [73, 42, 57]. In contrast, for contact-mode AFM the cantilever dynamics can be regarded fairly linear [80], and calibration of the sensor gain in B can be done before each imaging experiment by performing a force curve measurement [76]. The modeling of the higher order actuator dynamics is neglected in conventional AFM-systems, and the actuator displacement is approximated by a static scaling of the control signal $u(t)$, i.e. actuator model \hat{G} is taken as static. In high-speed AFM-systems, however, the bandwidth of the feedback loop is pushed close to, or even beyond the first the resonance frequency of the actuator, such that a dynamical actuator model \hat{G} must be used for more accurate sample topography estimation [80, 75].

Notice that when the noise $n(t)$ is assumed to be zero, the noise filter of Equation (3.6) becomes $F_2 = 1$, and the transfer from topography signal $h(t)$ towards the topography estimation error $\varepsilon(t)$ can be calculated as:

$$\begin{aligned} F_1(p) \cdot M(p) - 1 &= \frac{\hat{B}^{-1}(p)B(p) + \hat{G}(p) \cdot K(p) \cdot B(p)}{1 + L(p)} - 1, \\ &= \frac{\left[\hat{B}^{-1}(p)B(p) - 1 \right] + \left[\hat{G}(p) - G(p) \right] \cdot K(p) \cdot B(p)}{1 + L(p)}, \end{aligned} \quad (3.8)$$

i.e. part of the topography estimation error is stemming from the modeling error of the sensor dynamics $[B(p) \cdot \hat{B}^{-1}(p) - 1]$, and partly from the modeling error of the actuator dynamics $[\hat{G}(p) - G(p)]$. Hence, the accuracy of the topography estimation is strongly depending on the accuracy of the models for the sensor dynamics, and of the actuator dynamics.

The accuracy of the dynamical models may be hampered by variations in the dynamical behavior of the system, caused for instance by changing the cantilever, the sample mass, or the alignment of the sample on the scanner [101]. While during each AFM imaging experiment the system dynamics may be largely constant, the dynamical variations mostly occur from one imaging experiment to the next when setting up the new experiment. Although it is possible to identify these dynamical variations before each imaging experiment, this is not desirable as such identification experiments are time-consuming, require special expertise of the operator, and may also cause damage of the tip and the sample. Therefore, the dynamical variations of the system constitute a certain degree of dynamical uncertainty, which limits the modeling accuracy of the system dynamics, and therefore poses a limitation on the accuracy of the topography estimation.

Important is to note the influence of the feedback controller K in Equation (3.8), determining the propagation of the modeling errors towards the topography estimation error. Hence, due to the inevitable modeling errors of the system dynamics, the feedback control problem and the topography estimation problem are coupled. Consequently, the design of the feedback controller should be done not only considering the requirements on the control of the tip-sample force, but also considering the influence of the feedback controller on the accuracy of the topography estimation. Therefore, in the next section an integrated design methodology is proposed to handle this combined control and estimation problem in AFM, while

in Sections 3.4 and 3.5 the coupling between the control and estimation problems is experimentally verified based on a commercially available AFM system.

3.3 Robust design of the feedback controller and the topography estimator

The feedback controller and topography estimator should be designed such that (i) sufficiently fast tracking of the sample profile is provided in order to prevent too high force variation between the tip and the sample, which might cause damage between the tip and the sample, and (ii) the topography estimation error can be guaranteed to be within certain specifications, given the dynamical uncertainty of the system. To handle the coupled control and estimation problem in AFM, as analyzed in the previous section, the \mathcal{H}_∞ framework [90] is particularly suited as it allows to synthesize the controller and the estimator to guarantee certain specifications on the system performance, given a model of the system that captures the dynamical behavior of the system and its uncertainty. Therefore, in this research an integrated design methodology is proposed to design the feedback controller and topography estimator based on robust \mathcal{H}_∞ control techniques.

For simplicity, in the following only contact-mode imaging is considered in which the sensor dynamics B are assumed to be fully known, static, and normalized, i.e. ($B = \hat{B} = 1$). However, most of the considerations also hold for dynamic mode AFM. Furthermore, in this section only the estimator part that handles the system dynamics $F_1(s)$ is designed (cf. Eqn. (3.6)), as this part is responsible for accurately handling the system dynamics within the topography estimation. The noise filtering component $F_2(s)$ is considered to be done separately in the post-processing phase of each imaging experiment, and therefore in the following the influence of noise on the system performance is not considered. Hence, in this section the modeling errors of the actuator dynamics is considered as the sole source of the topography estimation errors.

The proposed design methodology consists of three steps:

1. The first step in the design process is to identify the dynamical behavior of the system including its dynamical variations, and to capture this dynamical behavior within a parametric model that can be used for model-based design of the feedback controller and the topography estimator.
2. In a second step the feedback controller, and topography estimator are designed via μ -synthesis [90] to satisfy certain specification on the system performance, given the system dynamics captured by the model.
3. In a third step the design of the estimator is improved by obtaining higher order models of the system dynamics. In contrast to the feedback controller, the topography estimator is not required to run in realtime which allows a higher computational complexity, and therefore allows the use of higher order dynamical models which may yield a better accuracy of the topography estimate.

In the subsequent sections these steps of the design method are discussed in more detail.

3.3.1 Step 1: Identification and modeling of the actuator dynamics

The dynamics of the z-actuator in AFM can be identified by driving the actuator with an excitation signal and measuring the cantilever deflection signal, while the lateral scanning motion is disabled. When using cantilevers with resonance frequencies higher than the frequency range of interest, while using small enough excitation amplitudes to keep the tip in firm contact with the sample during the identification experiments, the cantilever dynamics can be regarded as static and their influence can be neglected within these experiments. In order to identify the dynamical behavior of the system including its uncertainty under all working conditions, the measurements are repeated with different sample discs, and by changing the alignment of the sample disc on the scanner. The recorded frequency responses are denoted $\Upsilon_j(\omega_f)$, with $j \in [1 \dots k]$ the j^{th} frequency response measurement, and k the number of different frequency response measurements. The various load conditions during the identification experiments should be chosen such that the set of frequency responses $\Upsilon_j(\omega_f)$ gives a good and complete resemblance of how the system is used in practice. Based on the frequency response measurements of $\Upsilon_j(\omega_f)$ a nominal model and dynamical uncertainty set can be fitted that captures the dynamical behavior of the system with all possible combinations of measurement probes and samples:

$$\check{G}(s, \Delta) = G_n(s) \cdot (1 + \Delta(s) \cdot Q(s)) \quad (3.9)$$

$$\mathcal{G}(s) = \{ \check{G}(s, \Delta), \|\Delta(s)\|_\infty \leq 1 \}, \quad (3.10)$$

with $G_n(s)$ a parametric model of the nominal actuator dynamics, and filter $Q(s)$ and uncertain parameter $\Delta(s)$ capturing the dynamical variations of the system. To minimize the conservatism of the model, the nominal model $G_n(s)$ can be obtained by first determining the optimal non parametric response of the nominal model at each frequency point which minimizes the worst-case modeling error:

$$\Gamma(\omega_f) = \alpha(\omega_f) + i \cdot \beta(\omega_f), \quad (3.11)$$

$$\{\alpha(\omega_f), \beta(\omega_f)\} = \arg \min_{\alpha(\omega_f), \beta(\omega_f)} \max_{j=1 \dots k} |\Upsilon_j(\omega_f) - \alpha(\omega_f) - i \cdot \beta(\omega_f)|. \quad (3.12)$$

The minimization of Equation (3.12) has to be solved as an optimization problem at each frequency point, similar as described in [18]. Based on the optimal non-parametric nominal response $\Gamma(\omega_f)$, a parameterized nominal model $G_n(s)$ can be obtained by data fitting techniques [69]. Given the parametric nominal model $G_n(s)$ and the identification data from the various measurement trials, the worst-case multiplicative modeling error can be determined at each frequency point:

$$\Psi(\omega_f) = \max_{j=1 \dots k} \left| \frac{\Upsilon_j(\omega_f) - G_n(\omega_f)}{G_n(\omega_f)} \right|. \quad (3.13)$$

The maximum multiplicative modeling error $\Psi(\omega_f)$ can be incorporated in the set of Equation (3.9), via a parameterized over-bounding function $Q(\omega_f) \geq \Psi(\omega_f)$. The overbounding filter $Q(s)$ can be obtained using spectral overbounding techniques [77, 45].

Although in this research a multiplicative modeling error description is used in the model of Equation (3.9), other modeling error descriptions could be used as well (e.g. additive). In choosing a type of modeling error description it should be taken into account how tightly this modeling error description can be over-bounded by the finite order over-bounding function $Q(s)$ [21]. A too loose over-bounding function may lead to undesirably large conservatism in the model set, limiting the exactness of the synthesis solution. For the systems considered in this research the multiplicative uncertainty description resulted in the tightest upper-bounds.

3.3.2 Step 2: Model-based feedback controller and estimator design

Based on the dynamical model of Equation (3.9), the feedback controller and topography estimator are designed to guarantee \mathcal{H}_∞ -norm bounded performance specifications on the control error, and the topography estimation error. Therefore, the design problem is cast into the mixed-sensitivity framework [90], as depicted in Figure 3.4. The feedback controller K and topography estimator $F_{\mu-syn}$ are part of the same filter which depends on the parameters to be found θ . Hence, this filter has the negative cantilever deflection signal $-d(t)$ as input, and the control signal $u(t)$ and estimated sample topography $\hat{h}(t)$ as outputs. The resulting topography estimator is in the form of Equation (3.2), with only the cantilever deflection signal as input. The underscore $\mu-syn$ for the topography estimator in Figure 3.4 is used to denote that this is the estimator to be obtained via μ -synthesis, as also higher order estimator design is discussed in Section 3.3.3. Filters $W_{es}(s)$, $W_e(s)$, and $W_u(s)$ in Figure 3.4 are the weighting filters on the topography estimation error $\epsilon(t)$, the control error $e(t)$, and the controller output $u(t)$, respectively. These weighting filters can be chosen to represent the performance specification on the closed loop system, as demonstrated for a practical system in Section 3.4.1. This design methodology is similar as described for a nominal feedback controller and estimator design in [75], except for the fact that here the dynamical uncertainty of the system is explicitly addressed. The objective of the controller and estimator synthesis is now formulated as to find the parameters $\bar{\theta}$ that minimize the worst-case \mathcal{H}_∞ -norm of the system:

$$\gamma \geq \min_{\theta} \max_{\Delta} \left\| \begin{array}{c} W_e(s) \cdot S(s, \theta, \Delta) \\ W_u(s) \cdot K(s, \theta) \cdot S(s, \theta, \Delta) \\ W_{es} \cdot [F_{\mu-syn}(s, \theta) \cdot S(s, \theta, \Delta) - 1] \end{array} \right\|_{\infty}, \quad (3.14)$$

with upper-bound γ , and the sensitivity function of the uncertain system $S(s, \theta, \Delta) = [1 + \check{G}(s, \Delta) \cdot K(s, \theta)]^{-1}$. The minimization of Equation (3.14) is a non-convex optimization problem and requires iterative procedures as the μ -synthesis,

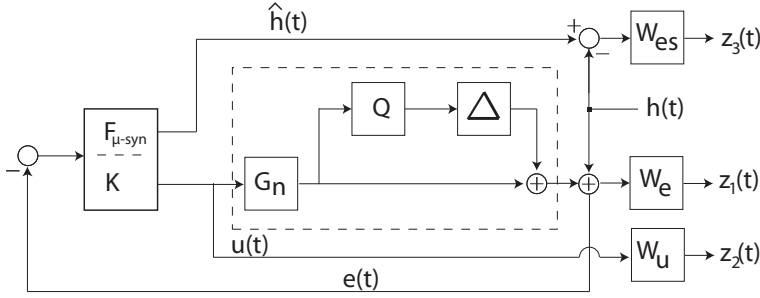


Figure 3.4: System description for design of the robust feedback control and topography estimator, with input $h(t)$, and performance channel-outputs $z_1(t)$, $z_2(t)$ and $z_3(t)$. This system is the entry for the μ -synthesis of Equation 3.14

DK -iteration method [90] in order to approximate the optimal controller parameters. After controller synthesis, the robust performance of the controlled system can be analyzed in a more accurate manner based on the nonparametric frequency responses $\Upsilon_j(\omega_f)$ obtained during the identification experiments, as discussed in Section 3.4.3.

3.3.3 Step 3: Improved estimator design

The topography estimator should be designed to minimize the worst case topography estimation error given the dynamical uncertainty of the system. Although for the model-based design of the feedback controller K and the topography estimator $F_{\mu\text{-syn}}$ the model of Equation (3.9) is assumed, due its limited order this model captures a larger set of frequency responses than the actual system, and therefore the obtained topography estimator may not provide the best performance robustness for the actual system. Moreover, the fact that the topography estimator is not restricted to run in realtime allows a high computational complexity and the use of a high order topography estimator, which may yield better accuracy. The topography estimation accuracy may be improved by redesigning the topography estimator, given the feedback controller K from the μ -synthesis, and the frequency responses $\Upsilon_j(\omega_f)$ obtained from the identification experiments. Based on the feedback controller K obtained via the minimization of Equation (3.14), and the identified frequency responses $\Upsilon_j(\omega_f)$, the worst case magnitude of the transfer from topography signal $h(t)$ towards the topography estimation error $\varepsilon(t)$ can be determined at each frequency point by:

$$\max_{j=1\dots k} \left| \frac{\tilde{F}(\omega_f) \cdot \begin{bmatrix} 1 \\ -K(\omega_f) \end{bmatrix} \cdot B}{1 + \Upsilon_j(\omega_f) \cdot K(\omega_f) \cdot B} - 1 \right|, \quad (3.15)$$

with $\tilde{F}(\omega) = [\hat{B}^{-1} \quad -\hat{G}(\omega)]$ the topography estimator following the structure of Equation (3.7), with both the cantilever deflection signal $d(t)$, and the control signal $u(t)$ as inputs (cf. Fig. 3.3), and assuming the noise filter $F_2 = 1$. While the topography estimator obtained from the μ -synthesis $F_{\mu\text{-syn}}$ is in the form of Equation (3.2) with only the cantilever deflection signal as input, it can also be casted in the form of Equation (3.7) by $\tilde{F}_{\mu\text{-syn}}(\omega) = [\hat{B}^{-1} \quad -\hat{G}_{\mu\text{-syn}}(\omega)]$, with $\hat{G}_{\mu\text{-syn}} = \frac{F_{\mu\text{-syn}}(\omega) - 1}{K(\omega)}$. Recall from Section 3.2 that the topography estimator with both the cantilever deflection signal $d(t)$ and the control signal $u(t)$ as inputs does not require accurate knowledge of dynamics of the feedback controller K , and therefore would yield better accuracy in practice. Assuming the sensor dynamics to be known $\hat{B} = B = 1$, the worst case magnitude of the transfer from topography signal $h(t)$ towards the topography estimation error $\epsilon(t)$ of Equation (3.15) know becomes:

$$\begin{aligned} & \max_{j=1\dots k} \left| \frac{[\hat{B}^{-1} \cdot B + \hat{G}(\omega_f) \cdot K(\omega_f) \cdot B] - [1 + \Upsilon_j(\omega_f) \cdot K(\omega_f) \cdot B]}{1 + \Upsilon_j(\omega_f) \cdot K(\omega_f) \cdot B} \right|, \\ & = \max_{j=1\dots k} \left| \frac{[\hat{G}(\omega_f) - \Upsilon_j(\omega_f)] \cdot K(\omega_f)}{1 + \Upsilon_j(\omega_f) \cdot K(\omega_f)} \right|, \end{aligned} \quad (3.16)$$

with $\hat{G}(\omega_f)$ the model of the actuator dynamics within the topography estimator. Hence, based on the frequency responses of $\Upsilon_j(\omega_f)$, the optimal nonparametric topography estimator which minimizes the worst-case magnitude of the transfer from topography signal $h(t)$ towards the topography estimation error $\epsilon(t)$ at each frequency point can be found by:

$$\begin{aligned} \tilde{F}_{nonpar}(\omega_f) &= [\hat{B}^{-1} \quad -\hat{G}_{nonpar}(\omega_f)], \\ \hat{G}_{nonpar}(\omega_f) &= \bar{\alpha}(\omega_f) + i \cdot \bar{\beta}(\omega_f), \\ \{\bar{\alpha}(\omega_f), \bar{\beta}(\omega_f)\} &= \arg \min_{\alpha(\omega_f), \beta(\omega_f)} \max_{j=1\dots k} \left| \frac{[\bar{\alpha}(\omega_f) + i \cdot \bar{\beta}(\omega_f) - \Upsilon_j(\omega_f)] \cdot K(\omega_f)}{1 + K(\omega_f) \cdot \Upsilon_j(\omega_f)} \right|, \end{aligned} \quad (3.17)$$

which can be calculated as a linear optimization problem at each frequency point. For practical implementation however, a parametric topography estimator is required which can be obtained from the optimal nonparametric topography estimator of Equation (3.17) via least squares data fitting techniques:

$$\tilde{F}_{par}(\omega_f) = [\hat{B}^{-1} \quad -\hat{G}_{par}(\omega_f)], \quad (3.18)$$

$$\hat{G}_{par}(\omega, \bar{\varphi}) = \arg \min_{\varphi} \sum_{\omega_f=\omega_1}^N \left[\hat{G}_{par}(\omega, \varphi) - \hat{G}_{nonpar}(\omega_f) \right]^2. \quad (3.19)$$

Minimization of Equation (3.19) can be done by the Sanathanan-and-Koerner method [69], or by Instrumental Variable based linear regression methods [11]. As demonstrated in Section 3.4, redesigning the topography estimator with high order dynamical models significantly improves the accuracy of the topography estimate as compared to the estimator $F_{\mu\text{-syn}}$ obtained via the minimization of Equation (3.14).

3.4 Design example and analysis

In order to verify the integrated design of the feedback controller and topography estimator presented in 3.3, the design methodology is demonstrated on the Multimode V system equipped with the J-scanner. Two different design cases are discussed and compared with different emphasis on the accuracy of the topography estimate.

3.4.1 Identification and modeling

In order to identify the dynamical behavior of the system and its variations, the system is setup several times with different sample discs, and by varying the alignment of the sample discs on the actuator. The actuator responses are measured by using a network analyzer (4395A, Agilent, Santa Clara, CA,USA). The system is prepared several times using different sample discs with masses ranging from 0.5 to 1 gram, and by varying the alignment of the sample disc on the actuator. By only using cantilevers with high free resonance frequencies (≥ 300 kHz) in contact mode, the sensor dynamics can be considered static below 100 kHz, which is the frequency range of interest. Therefore, the sensor dynamics B are neglected in the following analysis, and for convenience the DC-gain from actuator input $u(t)$ to cantilever deflection signal $d(t)$ is normalized ($\lim_{\omega \rightarrow 0} G(\omega) \cdot B(\omega) = 1$) in the following discussion.

The results of two different frequency response measurements are depicted in Figure 3.5a, showing the first longitudinal resonance of the piezoelectric tube scanner at 8 kHz. Based on 12 different frequency response measurements, the un-parameterized nominal frequency response $\Gamma(\omega_f)$ is (cf. Eqn. (3.11)) obtained via a linear optimization at each frequency point implemented via the optimization toolbox of `matlab`, as shown by the black solid line of Figure 3.5a. The un-parameterized nominal frequency response $\Gamma(\omega_f)$ is used to fit a 7th order dynamical model $G_n(s)$ by the Sanathanan-and-Koerner method via the `fitfrd` command of `matlab`. The nominal actuator model $G_n(s)$ is shown by the dashed-dotted lines of Figure 3.5a.

Based on the nominal model $G_n(s)$ the maximum multiplicative modeling error $\Psi(\omega_f)$ is determined (cf. Eqn. (3.13)), which is shown by the solid line of Figure 3.5b. The maximum multiplicative uncertainty $\Psi(\omega_f)$ clearly shows the variations in the dynamical behavior associated with the different load conditions, which tends to become larger with increasing frequency. Moreover, Figure 3.5b reveals a large peak in the dynamical uncertainty at 1 kHz, which is stemming from the coupling with the first lateral resonance modes of the scanner in the x and y directions. The dynamical uncertainty shown in Figure 3.5b poses a strong limitation on the achievable control bandwidth, and on the accuracy of the topography estimate. In order to incorporate this dynamical uncertainty into the model of Equation (3.9), a 5th order over-bounding function $Q(s) \geq \Psi(\omega_f)$ is obtained by the via the log-Chebyshev algorithm based `fitmagfrd` command of `matlab`, and manually adjusted to provide a tight over-bound for the dynamical uncertainty, as is shown by the dashed line of Figure 3.5b.

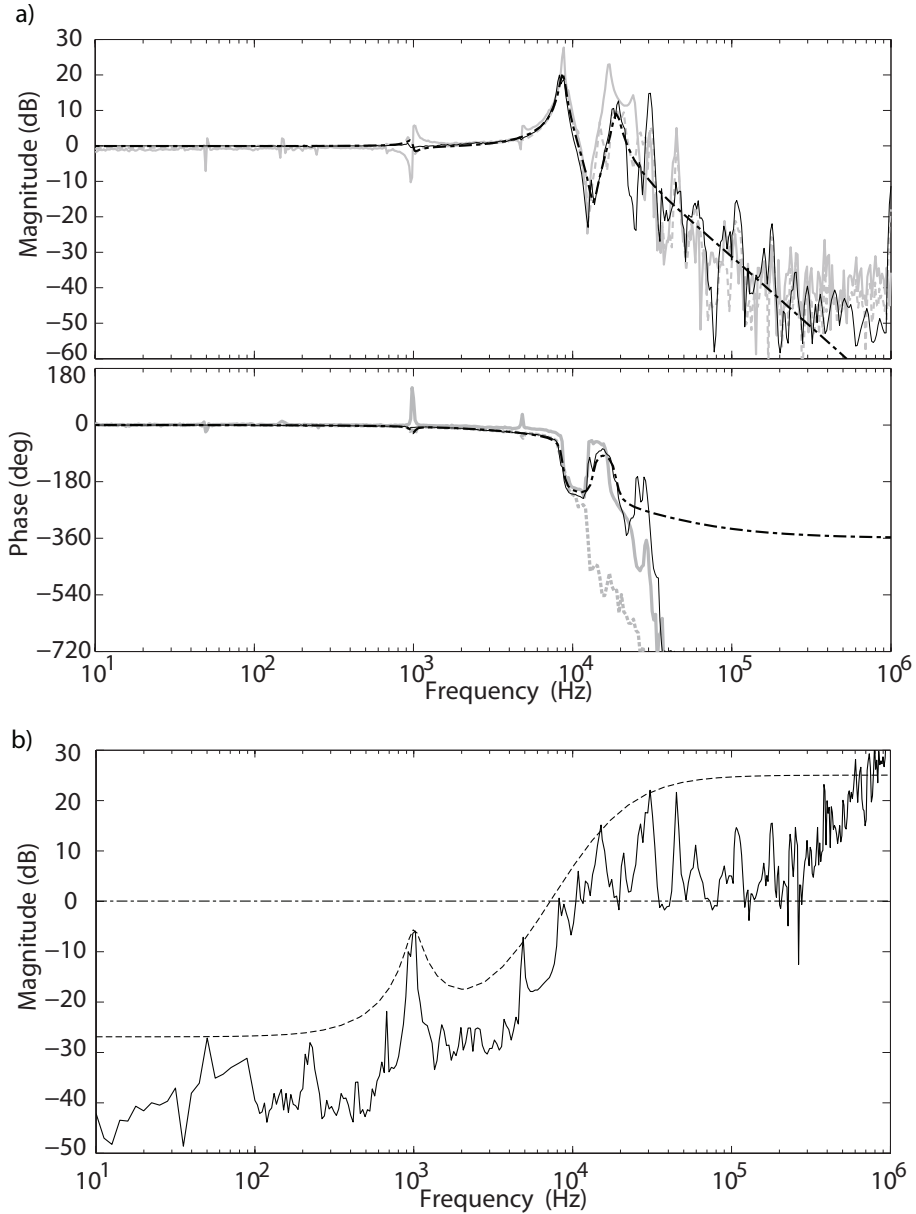


Figure 3.5: (a) Frequency response of the tube scanner measured in two identification experiments (solid grey, and dashed grey), the un-parameterized nominal response $\Gamma(\omega_f)$ (solid, black) calculated following Equation (3.11), and the frequency response of the 7th order model $G_n(s)$ (dashed-dotted, black). (b) Bode magnitude response of the maximum multiplicative model error $\Psi(\omega_f)$ calculated according to Equation (3.13), and the over-bounding filter $Q(s)$ (black, dashed).

While the frequency response measurements discussed above are captured with small amplitude excitation signals, for larger signals these type of piezoelectric actuators may suffer from hysteresis. For this particular actuator the hysteresis is measured to cause a gain variation of less than 1.5% at full positioning range, as discussed in Appendix A. These gain variations are, however, significantly smaller than the dynamical uncertainty stemming from the varying load conditions. Therefore, the 1.5%, or -36 dB dynamical uncertainty stemming from the hysteresis is considered to be sufficiently captured by the dynamical overbounding function $Q(s)$, and not explicitly addressed in the remainder of this chapter. For AFM systems with more severe actuator hysteresis, a method is discussed in Appendix A to explicitly address the hysteresis in the topography estimation utilizing a charge measurement.

3.4.2 Controller and estimator design

The dynamical model obtained from the identification experiments is used for the design of the feedback controller K and topography estimator $F_{\mu\text{-syn}}$ following the μ -synthesis procedure as discussed in Section 3.3.2. To enforce the desired disturbance rejection characteristics of the closed-loop system, the weighting filter $W_e(s)$ (cf. Fig. 3.4) is shaped as an inverse high-pass filter. The weighting filter $W_u(s)$ on the controller output is shaped as an inverse high-pass filter with a corner frequency of 6 kHz enforcing a high frequency roll-off to attenuate high frequency noise and higher order dynamical modes of the system. The emphasis which is given on the accuracy of the topography estimation can be tuned via the weight $W_{es}(s)$. In order to analyze the consequences of taking the topography estimation problem directly into account when designing the feedback controller, two different feedback controllers and corresponding topography estimators are synthesized, using different weights on the topography estimation error: $W_{es}(s) = 1$, and $W_{es}(s) = 8$. With these static weights the topography estimation error is weighted evenly strong over all frequencies, while also frequency depended weights on the topography estimation error may be used. Given these weights on the topography estimation error, the cornering bandwidth of the weighting filter on the control error $W_e(s)$ is tuned up to the point that the synthesis objective $\gamma \leq 1$ (cf. Eqn. (3.14)) is just met. This allows to find the maximum control bandwidth of the system given the performance specification on the topography estimation accuracy. After the μ -synthesis, for both design cases a 30th order parametric topography estimator F_{par} is designed according to the procedure discussed in Section 3.3.3.

3.4.3 Performance analysis

Figure 3.6 shows the open-loop frequency response plots of the feedback controllers corresponding to both design cases. Notice that in the design case with higher emphasis on the topography estimation accuracy (solid lines, Fig. 3.6) a lower overall controller gain is obtained, and also a steep notch filter at 1 kHz

in order to suppress the dynamical uncertainties associated with the lateral resonance of the tube-scanner in that frequency region (cf. Fig. 3.5b). Figures 3.7 shows the Bode magnitude plots of the nominal sensitivity function and the nominal complementary sensitivity function for both design cases, showing that both the disturbance rejection bandwidth (400 Hz vs. 1 kHz) as well as the tracking bandwidth (600 Hz vs. 3 kHz) is significantly lower for the design case with higher emphasis on the topography estimation accuracy.

Figure 3.8 shows the worst-case magnitude of the transfer from topography signal $h(t)$ towards the topography estimation error $\epsilon(t)$ according to Equation (3.15) analyzed for both design cases with the topography estimator $F_{\mu-syn}$ obtained from the μ -synthesis (gray lines), and with the 30th order estimator F_{par} designed according to Equation (3.18) (black lines). The solid lines, and the dashed lines in Figure 3.8 correspond to the design cases $W_{es}(s) = 1$, and $W_{es}(s) = 8$, respectively. The magnitudes of these graphs provide a measure of the accuracy of the topography estimate at each frequency point.

Comparing the results of Figures 3.7 and Figure 3.8 shows that for the system with the lower control bandwidth (solid lines), the accuracy of the topography estimate is better as compared to the case with the higher control bandwidth (dashed lines), particularly at higher frequencies. This is explained by the fact that with a lower control bandwidth, also the excitation of the uncertain dynamics is lower, which improves the accuracy of the topography estimation. Hence, Figures 3.7 and 3.8 clearly reveal the design trade-off between the control bandwidth of the system and the accuracy of the topography estimate.

Furthermore, comparing the gray lines in Figure 3.8 corresponding to the cases with the topography estimator $F_{\mu-syn}$ directly stemming from the μ -synthesis, with the black lines in Figure 3.8 corresponding to the topography estimator F_{par} obtained according to Equation 3.18, shows that for both design cases the topography estimation accuracy is significantly improved by the higher order dynamical models in F_{par} . Hence, these results clearly motivate the need for redesigning the topography estimator after the μ -synthesis, as discussed in Section 3.3.3.

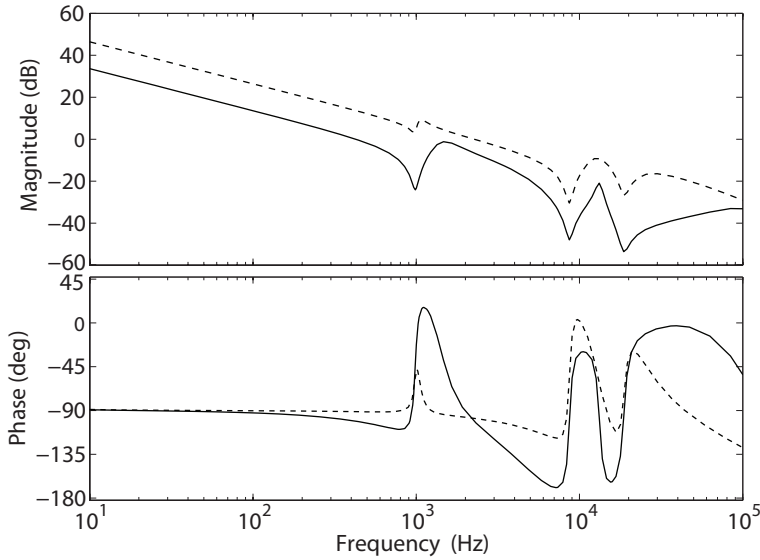


Figure 3.6: Open-loop frequency response plots of the designed feedback controllers. The dashed lines correspond to the design case with lower emphasis on the topography estimation accuracy ($W_{es} = 1$), and the solid lines correspond to design case with higher emphasis on the topography estimation accuracy ($W_{es} = 8$).

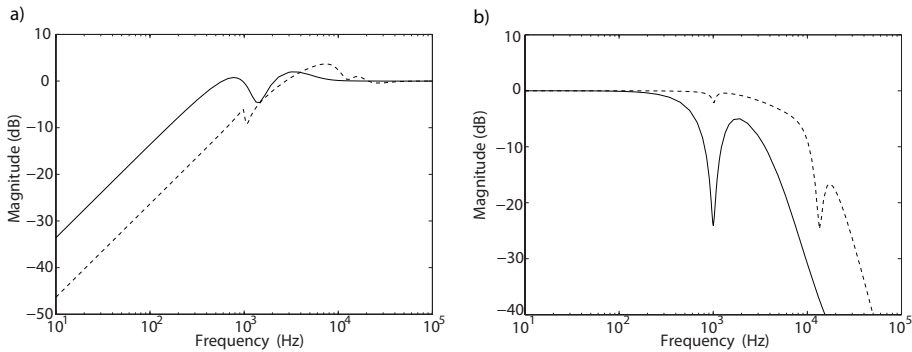


Figure 3.7: Frequency response plot of the nominal sensitivity function (a), and the nominal complementary sensitivity function (b). The dashed lines correspond to the design case with lower emphasis on the topography estimation accuracy ($W_{es} = 1$), and the solid lines correspond to design case with higher emphasis on the topography estimation accuracy ($W_{es} = 8$).

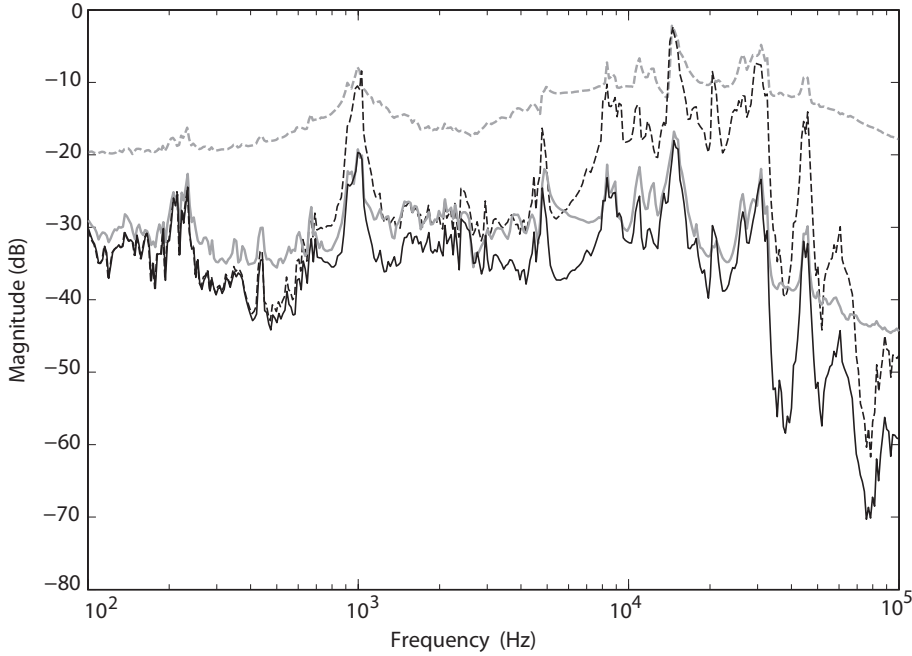


Figure 3.8: Worst-case magnitude of the transfer from topography signal $h(t)$ towards the topography estimation error $\varepsilon(t)$ determined at each frequency point for the closed-loop system designed with $W_{es} = 1$ (dashed lines), and $W_{es} = 8$ (solid lines). The gray lines correspond to the systems with the topography estimator $F_{\mu-syn}$ directly obtained from the μ -synthesis, while the black lines correspond to the systems with the 30th order parametric estimator F_{par} according to Equation (3.18).

3.5 Experimental results

The feedback controllers and topography estimators designed in the Section 3.4 are implemented on the physical system in order to experimentally verify three different aspects:

1. The two design cases discussed in Section 3.4 resulted in two feedback controllers with a different control bandwidth. In Section 3.5.2 the better the tracking performance of the high bandwidth feedback controller is validated.
2. While neglected in conventional AFM systems, in Section 3.2 it is shown that the system dynamics need to be addressed within the topography estimation in order to improve the accuracy, as also recognized in [80,75]. In Section 3.5.3 the improved accuracy is experimentally validated by comparing (i) the accuracy of a topography estimator where the actuator

dynamics are neglected and a static actuator model is used (i.e. $\hat{G} = c$), and (ii) the accuracy of a topography estimator which includes a dynamical actuator model $\hat{G}_{par}(s)$ designed according to Equation (3.18).

3. In Section 3.2 it is shown that due to the dynamical uncertainty of the system, the feedback control problem and the topography estimation problem are coupled. In Section 3.4, it is shown that due to this coupling a trade-off has to be made between the control bandwidth and the accuracy of the topography estimate. In Section 3.5.4 this trade-off is experimentally validated.

3.5.1 Implementation

The feedback controllers are implemented on the AFM system using a *Field-Programmable-Gate-Array* (FPGA, Virtex-II Pro XtremeDSP Development Kit, Nalatech, Camarillo CA, USA). To facilitate the implementation the 21th order low-bandwidth controller and the 25th order high-bandwidth controller obtained from the μ -synthesis are order reduced via the balanced truncation method [90] to 8th and 10th order, respectively. The controllers are discretized to a sampling rate of 260 kHz, and implemented on the FPGA in a biquad structure. The computation of the (model-based) topography estimation is done offline, by recording the cantilever deflection signal and the control signal via the data channels of the Nanoscope V controller, and filtering the data with the designed estimator in Simulink of matlab.

In order to isolate the topography estimation errors stemming from the dynamical uncertainty of the system from other error sources such as the scanner drift in the lateral plane and the finite sharpness of the tip, an artificial topography signal is added to the sensor signal using an analog summing amplifier, while the scanning motion of the system is disabled. As the artificial topography signal is fully known, this method allows to accurately verify the topography estimation errors stemming from the dynamical uncertainty of the system.

To compare the system performance with the different feedback controllers and topography estimators, a 200 Hz blockwave signal with an amplitude of 250 nm is applied to the system as 'topography' signal and the system responses are measured, as shown in Figure 3.9. The resulting signals are captured at a sampling rate of 100 kHz, of which the time stamp is denoted t_k , with $k \in [0, \dots, m]$ the recorded data samples. In order to judge the consistency of the results, these experiments are repeated 3 times while varying the weight and alignment of the sample on the scanner, of which the results are listed in Table 3.1. The results depicted in Figure 3.9 correspond to the experiment series denoted 'a' in Table 3.1.

Notice that the magnitudes of the control errors and the topography estimation errors of the different experiments listed in Table 3.1 strongly depend on the amplitude and frequency content of the applied topography signal. However, the chosen block-wave signal contains many different frequency components such that the obtained results are representative for a broad range of imaging experiments.

3.5.2 Tracking performance

Figures 3.9a-b show the controller outputs $u(t_k)$ (solid lines) for the system with the low-bandwidth, and with the high bandwidth controller captured from one experiment, along with the applied reference signal (dashed-lines). Meanwhile, Figures 3.9c-d show the corresponding measured tracking errors. Figures 3.9a-d clearly reveal that the system controlled by the high bandwidth controller provides faster recovery of the changes in sample profile. The results of the various experiments listed in Table 3.1 show that the RMS value of the tracking error ($\epsilon_{RMS} = \sqrt{\frac{1}{m} \sum_k^m e^2(t_k)}$) is about 30% lower in case of the high bandwidth feedback controller. The smaller tracking errors imply lower tip-sample force variations when imaging, which result in more gentle probing of the sample matter and less chances of damage to the tip and sample.

3.5.3 Influence of the estimator order on the topography estimation accuracy

Based on the recorded controller output $u(t_k)$ and the cantilever deflection signal $d(t_k)$, the topography signal is reconstructed using the topography estimator (cf. Eqn 3.7), which is implemented in Matlab-Simulink. Figures 3.9e-f show the estimated topography signals $\hat{h}(t_k)$ stemming from the topography estimators in two cases: (i) a topography estimator using a static actuator model $\hat{G} = c$ (red solid lines), similar as is done in conventional AFM systems, and (ii) a topography estimator with the 30th order dynamical actuator model $\hat{G}(s)$ (blue solid lines) designed according to the procedure discussed in Section 3.3.3. This dynamical model is discretized by the Tustins methods to the sampling rate of 100 kHz via the `c2d.m` command of `matlab`. Hence, the sample topography is obtained as $\hat{h}(t_k) = e(t_k) - \hat{G}(p_k) \cdot u(t_k)$, and $\hat{h}(t_k) = e(t_k) - c \cdot u(t_k)$ for the topography estimator with either the dynamical actuator model or the static actuator model as respectively shown by the blue and red lines in Figures 3.9e-f. The topography estimation errors $\epsilon(t_k) = \hat{h}(t_k) - h(t_k)$ are shown in Figure 3.9g-h, showing significantly less topography estimation errors when using a dynamical actuator model in the topography estimator, especially at the representation of the sharp edges of the sample topography. Table 3.1 lists both the RMS ($\epsilon_{RMS} = \sqrt{\frac{1}{m} \sum_k^m \epsilon^2(t_k)}$), and the peak values of the topography estimation error ($\epsilon_{max} = \max_{k \in [1, \dots, m]} |\epsilon(t_k)|$) for the different experiments, for the systems with either the static or the dynamic actuator model. Table 3.1 shows that with these experiments the peak of the topography estimation error is 25% to 60% less for the system with a dynamical actuator model, both with the low and with the high bandwidth controller. In case of the low bandwidth controller, the RMS value of the topography estimation error is about 30% less for the system with dynamical actuator model. In case of the high bandwidth controller the difference between both estimator designs in terms of RMS value of the topography estimation error is less pronounced, which is due to the stronger excitation of

Experiment series		400 Hz controller			1 kHz controller			
		a	b	c	a	b	c	
Tracking error		e_{RMS} [nm]	75	80	65	48	43	50
Topography estimation error	Static actuator model	ε_{RMS} [nm]	5	5	4	6	6	7
		ε_{max} [nm]	23	23	25	33	43	33
	Dynamic actuator model	ε_{RMS} [nm]	3	3	3	5	7	6
		ε_{max} [nm]	15	13	10	25	23	23

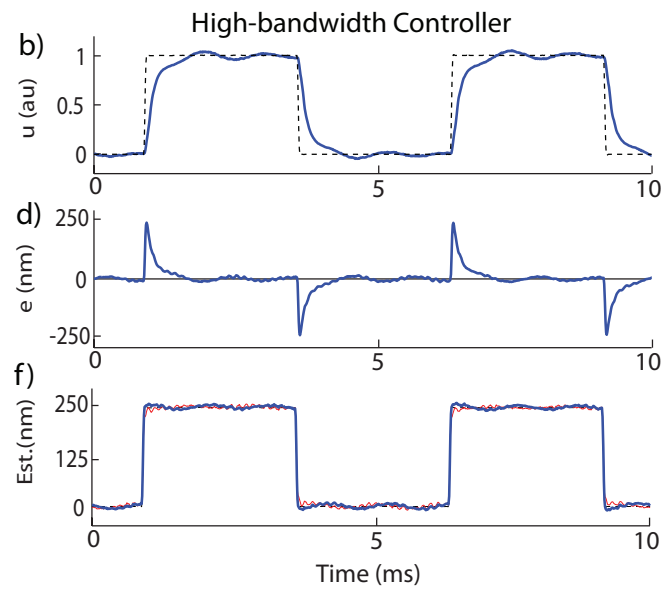
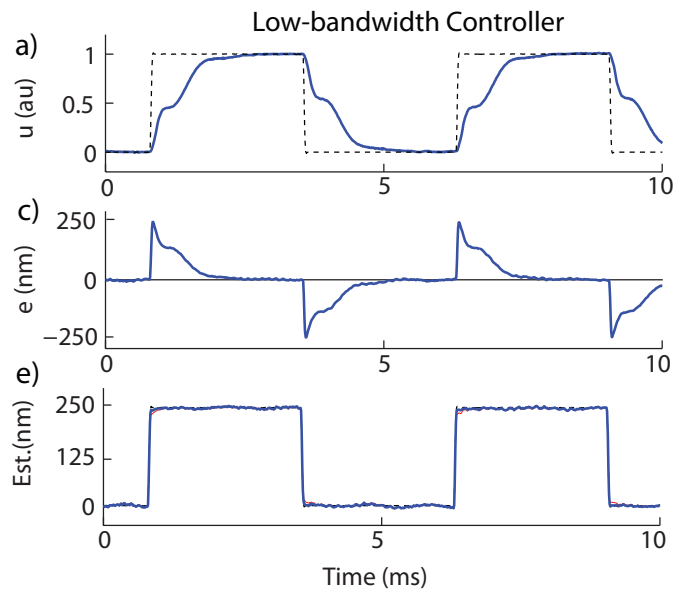
Table 3.1: Tracking error and topography estimation error in [nm] when applying a 200 Hz, 250 nm amplitude blockwave signal as topography signal to the system with different feedback controllers and topography estimators, as obtained with for 3 experiments (a,b,c) while varying the load conditions on the scanner.

the dynamical couplings with the lateral resonance mode at 1 kHz with the high bandwidth controller. The dynamical couplings with this lateral resonance mode strongly depend on the alignment of the sample disc on the scanner, and therefore causes large dynamical uncertainty at 1 kHz as also shown by Figure 3.5b. Figures 3.9i-j shows the frequency spectra of the topography estimation errors, clearly showing that the system with dynamical actuator model performs better in all frequencies, apart from the frequency region of the first lateral resonance mode at 1 kHz. This is explained by the fact that the dynamic actuator model is designed to minimize the worst-case modeling error over all possible experiments (cf. Section 3.3.1), which does not guarantee that it provides the best match in every experiment. However, the results shown in Figure 3.9e-h and Table 3.1 clearly reveal the overall benefit of using a dynamic actuator model in the topography estimate, especially for the representation of the sharp edges of the sample.

3.5.4 Influence of the controller bandwidth on the topography estimation accuracy

Comparing the topography estimation errors stemming from the system with the low bandwidth controller with those of the system with the high bandwidth controller clearly reveals that the accuracy of the topography estimate is about 40% better with the low bandwidth controller, both in terms of RMS and in peak error. Therefore, these results clearly confirm the trade-off between the bandwidth, and the accuracy of the topography estimate, as also shown by the frequency domain results in Figure 3.8.

The frequency spectra of the topography estimation error signals, shown in Figures 3.9i-j, clearly reveal that the major frequency components of the topography estimation signals are around the lateral resonance mode at 1 kHz, and the first longitudinal resonance mode at 8 kHz, which correspond to the frequency regions with the highest dynamical uncertainty (cf. Fig. 3.5). Hence, these results show good resemblance with the frequency domain results obtained in Section 3.4.



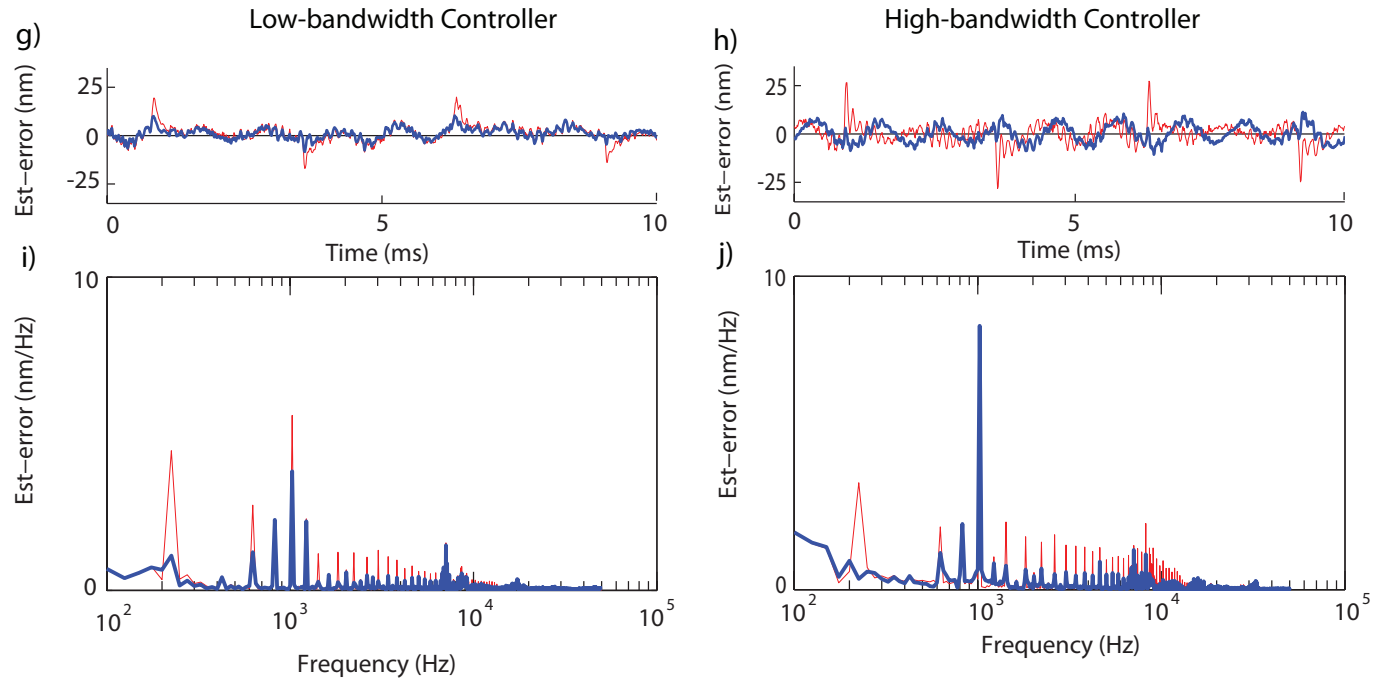


Figure 3.9: System outputs when applying a 200 Hz, 250 nm block wave signal as an artificial topography signal, for the case with the low bandwidth controller (a,c,e,g,i), and for the case with the high bandwidth controller (b,d,f,h,j). Figures (a-b) show the applied topography signal together with the output of the feedback controller, while figure (c-d) show the control error. Figures (e-f) shows the outputs of the topography estimator, Figures (g-f) show the topography estimation error, and Figures (i-j) show the frequency spectra of the topography estimation error signal. The red lines in Figures (e-j) correspond to case when using a static actuator model in the topography estimator, and the blue lines corresponds to the case when using a dynamic actuator model in the topography estimator.

3.6 Conclusions

This chapter presents an integrated approach to design a robust feedback controller and topography estimator for the feedback loop controlling the tip-sample force in AFM, while taking into account the dynamical uncertainties of the system. The proposed design approach is demonstrated on a commercially available AFM-system, showing two different designs with different emphasis on the accuracy of the topography estimation. Experimental results verify that due to the dynamical uncertainty of the instrument a trade off has to be made between the control bandwidth of the feedback loop controlling the tip sample force, and the accuracy of the topography estimation. Moreover, it is experimentally verified that the use of a dynamic actuator model in the sample topography estimator significantly improves the accuracy of the instrument.

As a consequence of the trade-off between the control bandwidth and the accuracy, the intended imaging applications of the instrument has to be considered when designing the feedback controller and topography estimator in AFM. When imaging for instance fragile biological samples, minimizing the force variations between the tip and the sample may be most important in order not to damage the sample, aiming for an as high as possible control bandwidth and therefore the requirements on the accuracy of the topography estimation may be relaxed. However, in other application such as quality assurance in the semiconductor industry, higher emphasis might be given on the quality of the topography estimation. Samples from material science or semiconductors potentially are not as fragile as biological systems, and higher importance may be given to the metrological aspects of the instrument. The integrated design method proposed in this contribution can be used to handle this design trade-off and optimize the feedback controller and topography estimator of the system to the particular imaging application.

These results also indicate that reducing the dynamic uncertainty of the system may be an important design criterion for future AFM development. The consistency of the dynamical behavior may be improved for instance by fixing the alignment of the sample on the scanner, normalizing the weight of the sample discs, or by damping the weakly damped (lateral) resonances within the system for instance by the self-sensing actuation method discussed in Chapter 2. Reducing the dynamical uncertainty of the system would allow better prediction of the dynamical behavior of the system and therefore allow both faster and more accurate AFM imaging.

Dual actuated control of the tip-sample force³

The imaging speed in AFM is strongly limited by the bandwidth of the feedback loop controlling the tip-sample force. To increase the closed-loop bandwidth, without sacrificing effective positioning range, dual actuated control of the tip-sample force is investigated, combining a long-range, low-bandwidth actuator with a short-range, high-bandwidth actuator. This chapter is focussed at systematic design of the controller for dual actuated AFM, in order to improve the performance of a given dual actuated AFM, and to identify the performance limiting aspects. The design of a feedback controller for a prototype dual actuated AFM is reported, aimed at achieving the highest control bandwidth possible. Special emphasis is laid on guaranteeing robust stability of the feedback loop under influence of variations in the dynamical behavior of the system, and to prevent strong destructive interference between both actuators. To prevent instability of the feedback loop due to saturation of the short-range actuator, an anti-windup controller is presented that robustly stabilizes the system under all imaging conditions. The designed feedback controller is implemented on a prototype dual actuated AFM system, and demonstrates a disturbance rejection bandwidth of 20 kHz, which is about 20 times faster than the optimally controlled single actuated system. AFM images are obtained verifying a significant reduction of force variations between the tip and the sample while imaging.

4.1 Introduction

The demand for high speed AFM imaging sets high requirements on the feedback loop that controls the tip-sample force, which should prevent damage between

³Parts of this chapter are also published in [48, 54, 52, 53]

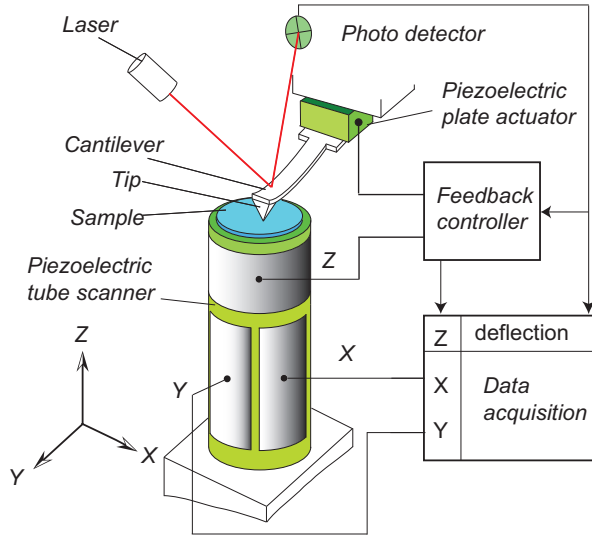


Figure 4.1: Schematic representation of a dual actuated atomic force microscope. The tip-sample force is controlled via a piezoelectric tube scanner that provides the long-range vertical positioning of the sample and an additional piezoelectric plate actuator to provide short-range vertical positioning of the cantilever chip.

the tip and the sample during imaging and provide an estimate of the sample topography. When increasing the scanning speed, the sample topography variations to be tracked by this feedback loop occur faster, which requires a higher control bandwidth of this feedback loop to prevent too large tip-sample forces. This becomes particularly important when imaging fragile biological specimen at high imaging speed or at rough sample surfaces [36].

Improved control of the tip-sample force by use of modern model-based control techniques has been investigated [84, 75], explicitly taking into account a model of the actuator dynamics in the design of the feedback controller. As compared to the classical PI-controllers used in most commercially available AFM systems, these model-based control techniques allow up to about 5 times higher closed-loop bandwidth. Furthermore, feedforward control methods are investigated, making use of the fact that the sample topography is partly repetitive from one scan-line to the next [84], which significantly reduces the tip-sample force variations. However, the control bandwidth that can be obtained for a given AFM system is most often limited by the dynamical uncertainty associated with the higher order resonance modes of the piezoelectric actuators [80].

In order to allow higher control bandwidths prototype high speed AFM systems are developed with improved actuator design optimized to push the first resonance modes to higher frequencies. Most often these high bandwidth AFM systems utilize piezoelectric stack actuators, which typically result in a stiffer construction and therefore higher resonance modes [46, 5, 79, 29]. Moreover, MEMS-based actuators are developed with integrated measurement probes [93, 94]. Op-

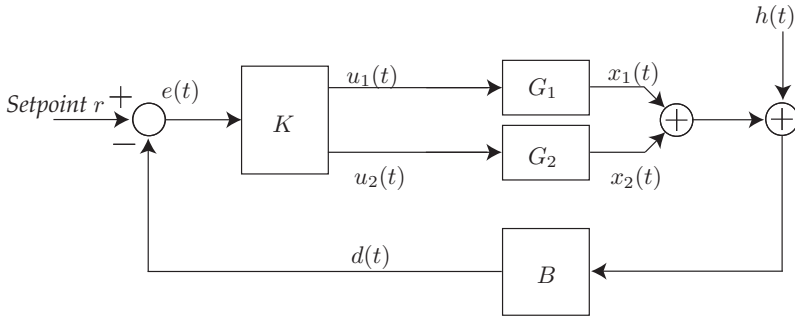


Figure 4.2: Block diagram depicting dual actuated control of the tip-sample force. The tip-sample force is controlled via the long-range, and the short-range actuator, denoted G_1 , and G_2 , respectively. During imaging the sample topography $h(t)$ enters the system as an unknown disturbance.

timizing these type of actuators for high-bandwidth positioning, however, often comes at the cost of a significant reduction in positioning range, limiting the application of these actuators to samples with relatively small topographic features when used as the sole means to track the sample surface. Meanwhile, often in AFM imaging the larger topographic variations are typically varying slowly, while the faster topographic variations are often of smaller amplitude. This aspect allows to combine a long-range, low-bandwidth actuator with a short-range, high-bandwidth actuator in order to obtain a system with both a high control bandwidth as well as a large effective positioning range. This technique is generally referred to as dual-actuation, and the resulting system can be seen as a simple form of an over-actuated system. Dual actuation has been thoroughly investigated for implementations on Hard Disk Drives (HDD) (e.g. [65,40]), and also has been investigated for the use within scanning probe microscopes [29,93,81,43,26], showing vast improvements on the control-bandwidths of the vertical feedback loops as compared to single actuated system.

This chapter reports on the development of a systematic approach of designing the controller for such dual actuated AFM, with special emphasis on dealing with the dynamical uncertainty of the system, handling the limited positioning range of the short-range actuator, and the topography estimation in dual actuated AFM. The design of the controller requires a comprehensive analysis of the overall control requirements, and the performance limiting factors of the overall system. Therefore, a systematic design of the controller may significantly improve the performance of the overall system, and additionally provide valuable insights on the potential, limitations, and design trade-offs in dual actuated AFM, which could be used to formulate the design requirements for future high speed AFM designs.

4.1.1 Control problem in dual actuated AFM

The principle of a dual actuated AFM is depicted in Figure 4.1, in which the tip-sample force is controlled via the long-range and the short-range actuator. This

system may also be represented by the block diagram of Figure 4.2. Similar as for conventional single actuated AFM systems, the controller for a dual actuated AFM should satisfy the following design requirements:

- Track the sample topography to minimize tip-sample force variations
- Provide an estimate of the sample topography.
- Provide robustness against dynamical variations of the system.

Other than for conventional, single actuated AFMs, one important design consideration for the feedback controller of a dual-actuated AFM is posed by the limited positioning range of the short-range actuator. The underlying assumption of dual actuated AFM is that the long-range actuator primarily tracks the larger amplitude low-frequency topography variations, while the short-range actuator has sufficient range to track high frequency topography variations that typically have smaller amplitudes. Hence, the feedback controller should provide a frequency separation between both control paths, assigning different frequency regions to the actuators. One important aspect in addressing the frequency separation in the controller design is to prevent strong destructive interference between both actuators in which they negate part of each others motion, caused by too large phase difference between both control paths [87]. This destructive interference will be referred to as 'actuator fighting', and may result in large ineffective controller outputs which may reduce the effective positioning range. Furthermore, due to the limited positioning range of the short range actuator, actuator saturation may occur due to incidental large disturbances or due to large steps in the sample surface. When saturation of the short-range actuator occurs the system is entering a non-linear operating regime which can lead to instability of the overall control system if not accounted for. Hence, for dual actuated AFM the designed control system has to satisfy two additional design requirements:

- Provide a frequency separation between both actuators, without introducing strong actuator fighting.
- Prevent instability and provide fast recovery of the closed-loop system if saturation of the short-range actuator occurs.

The design of the controller is therefore split into two stages; first a nominal linear feedback controller is designed aimed at optimal performance within the intended linear operating regime of the system, and secondly an anti-windup controller is designed which guarantees stability and fast recovery of the system in case of saturation of the short-range actuator.

As discussed in Chapter 3 the requirements on the tracking bandwidth and on the accuracy of the topography estimate can be conflicting due to the dynamical uncertainty of the system, and a trade-off has to be made between the two. However, as the main argument for dual actuated AFM is to increase the control bandwidth of the system, in this research first a control system is designed to push the bandwidth of the system towards its maximum control bandwidth, while neglecting the influence of the feedback control bandwidth on the accuracy of the

topography estimation accuracy. This design case is consistent with the imaging applications where minimizing the variations of the tip-sample forces is most important to prevent damage to the tip and sample, and the metrological aspects of the system are deemed less important, for instance when imaging fragile biological samples at high speed. This allows to investigate the full potential of the dual actuated system in terms of imaging bandwidth, and the aspects concerning the saturation of the short-range actuator. As an additional step the topography estimation in dual-actuated AFM is investigated, explicitly addressing the accuracy of the topography estimate in the controller design based on the integrated design approach of Chapter 3.

4.1.2 Experimental Setup

For this research the Mutlimode V system is extended to a dual actuated system. The piezoelectric tube-scanner of this system (J-Scanner, Bruker, Santa Barbara USA), is used to provide the scanning motion of the sample during imaging, as well as the vertical positioning of the sample to control the tip-sample force. This piezoelectric tube scanner is referred to as the 'long-range actuator', and is driven by an external piezo amplifier (PZD700, Trek, Medina, USA) providing a vertical positioning range of $5 \mu\text{m}$. This system is extended to a dual actuated system by using a small piezoelectric plate actuator (CMAP12, Noliac, Kvistgaard, Denmark) which is glued onto the cantilever holder to form the new mounting spot for the cantilever-chip (cf. Fig. 4.3), and allows vertical positioning of the cantilever-chip. The plate-actuator is driven by a piezo amplifier (A400, FLC-electronics, Partille, Sweden), of which the output voltage is restricted to $20 V_{pp}$ to prevent it from running into its current limitations while dynamically driving the 36 nF capacitive load of the piezoelectric plate actuator. This allows a maximum positioning range of about $0.5 \mu\text{m}$ for the piezoelectric plate actuator, which will be referred to as the 'short-range actuator'.

Although also different types of dual-actuated AFM systems can be found in literature with the long-range actuator positioning the cantilever and the short-range actuator positioning the sample, from a control engineering point of view the overall system architecture is similar, and therefore the methodology developed in this research can be translated to other types of dual actuated AFM systems as well.

4.1.3 Outline

In Section 4.2 the design of the nominal, linear feedback controller for dual actuated AFM is discussed, focussed at controlling the tip-sample force at the maximum control bandwidth given the two actuators. Special emphasis is laid on guaranteeing robust stability of the system under influence of uncertain dynamics of the actuators, and preventing strong destructive interference between the control actions of both actuators. In Section 4.3 an approach is discussed to analyze the stability of the feedback loop during saturation of the short-range actuator, and an anti-windup controller is introduced that assures stability of the feedback

loop under all imaging conditions. The improved closed-loop bandwidth of the dual-actuated system is experimentally verified in Section 4.4 and demonstrated in an imaging application, enabling higher imaging speeds. In Section 4.5 the topography estimation accuracy for dual actuated systems is analyzed and addressed in the design of the feedback controller and the topography estimator. The conclusions of this work are discussed in Section 4.6.

4.2 Linear feedback controller design for dual actuated AFM

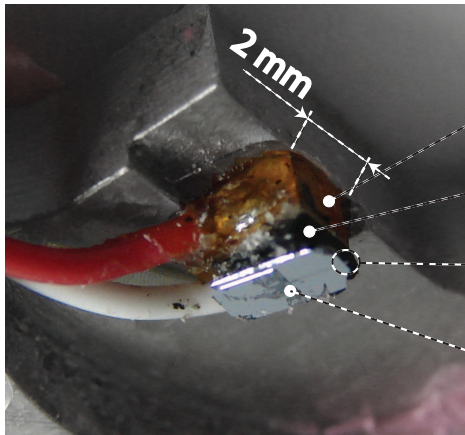
In this section a linear feedback controller is designed for the dual actuated AFM to allow tracking of the sample topography with the maximum bandwidth possible, provided that the system is robustly stable against the dynamical uncertainties of the system. In this chapter the influence of the feedback controller on the topography estimation accuracy is neglected, reducing the control problem to a classical tracking control problem, as can be depicted by the block diagram of Figure 4.2. In the design of the feedback controller special emphasis is laid on preventing strong destructive interference between both actuators.

4.2.1 Design procedure nominal feedback controller

Although the dual-actuated servo systems are multi input/single output (MISO) systems, several controller design methods can be found in literature which are based on SISO controller design techniques. Examples are the nested or Master-Slave structure (e.g. [93]), and the decoupled Master-Slave structure [34], in which the individual control paths are sequentially tuned. Alternatively, in [87] a method is proposed in which first the design of the controller is focussed on tuning the frequency separation between both control-paths, while in a second step the overall feedback control action is tuned. Although these SISO-based design methods provide intuitive ways to design a feedback controller for dual actuated systems, the sequential design of the different parts of the controller, and the fact that specific controller structures are pre-imposed might not always lead to the best possible performance of the overall system.

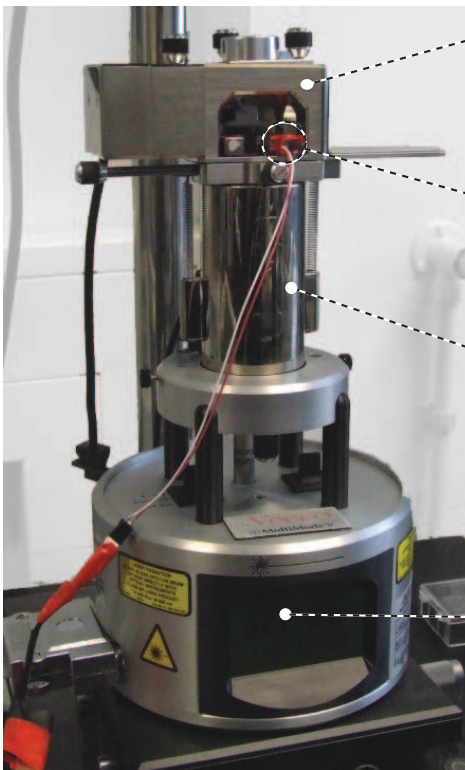
Model-based controller design methods are well suited for these type of MISO systems, and have the advantage that the overall closed-loop behavior can be directly enforced, without pre-imposing a certain structure on the controller. Model-based feedback controller designs for dual actuated systems are reported in literature for dual-stage HDD drives (see [40] and the reference therein), and more recently on dual-actuated AFM [81]. As outlined above, an important design criterion for the feedback controller in AFM is to provide robustness against the dynamical variations of the system, occurring for instance when using varying cantilevers and samples and by variations of the alignment. A model-based controller design that guarantees both robust stability as well as robust performance against dynamic uncertainties of the system is shown in [38] for dual-stage HDD drives by over-bounding the multiplicative dynamical uncertainty of the system with weighting

a)



Piezoelectric plate actuator
 Wedge to tilt
 Cantilever
 Location
 Cantilever
 Cantilever chip

b)



'AFM head'
 (containing laser
 and photodiode)
 Cantilever holder
 with piezoelectric
 plate actuator (cf. (a))
 Piezoelectric
 tube scanner
 'AFM' base
 (electronics)

Figure 4.3: Picture of the piezoelectric plate actuator manipulating the vertical position of the cantilever chip (a), and the complete dual actuated AFM system (b).

filters and applying μ -synthesis. To minimize the conservatism of this method, a tight over-bound of the dynamic uncertainty is needed. This, however, might lead to very high model orders and consequently high order feedback controllers which may be limited at the practical implementation. In [18] the use of high order over-bounding functions is circumvented by capturing the dynamic uncertainty as a parameter variation of several modes within the nominal model. For the actuators used in this particular research, however, the uncertain dynamical modes in the frequency range of interest are too numerous, and therefore it is impossible to sufficiently capture the dynamical uncertainty in a parametric sense (cf. Fig. 4.4).

The μ -synthesis techniques result in a non-convex optimization problem that needs to be solved by iterative method such as the *DK*-iteration methods. A drawback of these iterative optimization methods is that they may not always converge to the optimal controller parameters, and require the use of *D*-scalings which increase the resulting controller order. Therefore, the controller obtained from the μ -synthesis may not always be directly implementable, due to the limitations of the computational power of the real time signal processing hardware, particularly when a high control bandwidth (and thus sampling rate) is required. Alternatively, the controller design problem can be posed as a nominal \mathcal{H}_∞ problem, which results in a more tractable controller synthesis problem, and results in lower order controllers due to the absence of *D*-scalings. Although nominal \mathcal{H}_∞ does not allow to explicitly address the dynamical uncertainty of the system, robust stability can be implicitly imposed by enforcing bandwidth constraints for both actuators via the usual weighting filters. Therefore, in this research first the maximum allowable actuation bandwidth at which robust stability can still be guaranteed are determined for both actuators directly from frequency domain identification data, as discussed in Section 4.2.2. Next the feedback controller is designed via nominal \mathcal{H}_∞ controller synthesis techniques in which the actuation bandwidth limitations for both actuators are taken into account via the weighting filters, as discussed in Section 4.2.3. After the design of the feedback controller the robustness of the control system is verified via μ -analysis, based on a non-parametric model of the actuator dynamics and the uncertainty. As a first step of this design process, the actuator dynamics are identified for various combinations of cantilever chips and samples to analyze the dynamic behavior of the system over various measurement experiments, and to acquire a model of the systems dynamics to be used for model-based control design.

4.2.2 System identification and analysis

To identify both the nominal dynamical behavior of the system, as well as its dynamical variations over various imaging experiments, the frequency responses of both actuators are measured 12 different times while varying the type and the alignment of the cantilever chips and sample discs. The various load conditions are representative for actual AFM-measurements with the typical variation in the system setup. As the system used in this particular research is used for high-speed contact-mode imaging, only AFM-cantilevers with high free resonance frequency

are considered, ($300 \text{ kHz} < f_0 < 600 \text{ kHz}$). The weight of the sample discs used within these identification experiment ranges from 0.5 to 1 grams. The frequency responses of the vertical actuators of the AFM-system are identified by applying a reference signal to the actuators and measuring the cantilever deflection, while the tip is in contact with the sample and the scanning motion is disabled. The frequency responses are recorded by a network analyzer (4395A, Agilent, Santa Clara, USA), and stored in vectors denoted $\Upsilon_{l,j}(\omega_f)$, with $\omega_f \in \Omega_f$ the frequency points ranging from 10 Hz to 1 Mhz, and integer $j \in [0, n]$ denoting the measurement number. Subscript l is used to denote the corresponding actuator, with $l = 1$ being the long-range actuator, and $l = 2$ the short-range actuator. The results of two typical realizations of the identification experiments for both actuators are shown in Figure 4.4 (gray, solid and dashed lines). From Figure 4.4 the first longitudinal resonance of the long-range actuator can be recognized at 8 kHz, and for the short-range actuator the fundamental resonance can be recognized at 150 kHz. For convenience the DC-gains of the actuator outputs are normalized ($\lim_{\omega \rightarrow 0} G_l(\omega) = 1$).

Based on the obtained frequency responses $\Upsilon_{l,j}(\omega_f)$ first a nonparametric model is determined that captures the dynamical behavior of the system, and allows to analyze the degree of dynamical uncertainty of the actuator dynamics at each frequency point. The amount of dynamical uncertainty is determined by first finding the center of the set of $\Upsilon_{l,j}(\omega_f)$, at each frequency point, and then determining the maximum variation of the multiple frequency responses with respect to this center point. The center of the set of frequency responses $\Upsilon_{l,j}(\omega_f)$ can be found at each frequency point by:

$$\begin{aligned} \Gamma_l(\omega_f) &= \alpha(\omega_f) + i \cdot \beta(\omega_f), \\ \{\alpha(\omega_f), \beta(\omega_f)\} &= \arg \min_{\alpha(\omega_f), \beta(\omega_f)} \max_{j=1 \dots k} |\Upsilon_{l,j}(\omega_f) - \alpha(\omega_f) - i \cdot \beta(\omega_f)|, \end{aligned} \quad (4.1)$$

which is calculated in the same manner as is done in Section 3.3.1. The obtained nonparametric frequency responses $\Gamma_l(\omega_f) \in \mathbb{C}$ can be viewed as the ‘nominal’ frequency response, and is shown in Figure 4.4 (black, solid lines) for both actuators. Based on the nominal frequency response the maximum dynamical variations can be determined at each frequency point, i.e. $\max_{j=1 \dots n} |\Upsilon_{l,j}(\omega_f) - \Gamma_l(\omega_f)|$. By normalizing the maximum dynamical variations by the magnitude of $\Gamma_l(\omega_f)$, the ‘multiplicative dynamical uncertainty’ is obtained:

$$\Theta_l(\omega_f) = \max_{j=1 \dots n} \left| \frac{\Upsilon_{l,j}(\omega_f) - \Gamma_l(\omega_f)}{\Gamma_l(\omega_f)} \right|. \quad (4.2)$$

The resulting multiplicative uncertainties $\Theta_l(\omega_f)$ are shown in Figure 4.5, showing that the dynamical uncertainty of both actuators significantly increases at higher frequency. At frequency regions where the magnitude of the multiplicative dynamical uncertainty is larger than one ($\Theta_l(\omega_f) > 1$), the dynamical variation of the system is more than 100% of its center value, and hence the phase behavior of the system is fully unpredictable in that frequency region. Therefore, the frequency at which the multiplicative uncertainty exceeds the 0 dB-line can be seen as the absolute limit of the bandwidth at which the system can be robustly con-

trolled. From Figure 4.5 it can therefore be deduced that for the long-range actuator the maximum bandwidth is about 6 kHz, and for the short-range actuator the maximum bandwidth is about 40 kHz. These bandwidth limitations are explicitly taken into account in the design of the nominal feedback controller, as discussed in Section 4.2.3.

In order to allow model-based design of the feedback controller, parametric dynamical models are fitted based on the nominal frequency responses $\Gamma_l(\omega_f)$ (cf. Eqn. (4.1)). This data fitting is done using least squares data-fitting method according to the Sanathanan-and-Koerner method [69], which is implemented via the `fitfrd.m` command in `matlab`. In order to capture the dominant dynamical behavior of the actuators the model order are chosen 7th order and 5th order for the long-range and short-range actuators, respectively. These models are shown by the black dashed-dotted lines of Figure 4.4, and are used for controller synthesis as discussed in Section 4.2.3.

In order to allow verification of the robust stability of the closed-loop system after the designed of the feedback controller, a nonparametric frequency response model is used based on the nonparametric nominal response $\Gamma_l(\omega_f)$, and the multiplicative dynamical uncertainty $\Theta_l(\omega_f)$:

$$\mathcal{G}(\omega_f, \Delta) = \begin{cases} \Gamma_1(\omega_f) \cdot (1 + \Delta_1(\omega_f)\Theta_1(\omega_f)) \\ \Gamma_2(\omega_f) \cdot (1 + \Delta_2(\omega_f)\Theta_2(\omega_f)) \end{cases}, |\Delta_1(\omega_f)| \leq 1, |\Delta_2(\omega_f)| \leq 1, \forall \omega_f \in \Omega_f, \quad (4.3)$$

with $\Delta(\omega_f) \in \mathbb{C}$ the normalized, complex uncertain parameter which describes the dynamical uncertainty of the system at each frequency ω_f . Although the model of Equation (4.3) captures a larger set of frequency responses than the actual dynamics of the system, and therefore is slightly conservative, it allows to obtain valuable quantitative information on the stability margins of the closed loop system via μ -analysis, as discussed in Section 4.3.

4.2.3 Model-based feedback controller design

Based on the obtained parameterized frequency response models of the actuator dynamics $G_1(s)$ and $G_2(s)$ (black, dashed dotted lines of Fig. 4.4), the feedback controller is designed aimed at pushing the bandwidth for the overall system towards the maximum achievable control bandwidth of the short-range actuator, which in the previous section is determined to be 40 kHz. Moreover, an important design criterion for the feedback controller of dual actuated systems is to create the frequency separation between both actuators, such that the long-range actuator particularly tracks the low-frequency topography variations, while the short-range actuator takes over at higher frequencies. With model-based \mathcal{H}_∞ these design requirements on the closed-loop system can be directly enforced via proper choice of the weighting filters. To this end the controller design problem is cast in the mixed-sensitivity framework as depicted in Figure 4.6. The following transfer function blocks can be recognized: the nominal actuator dynamics $G(s) = \text{diag} [G_1(s), G_2(s)]$, the weighting filter on the control error $W_e(s)$, the weighting filter on the actuator outputs $W_y(s) = \text{diag} [W_{y1}(s), W_{y2}(s)]$, and

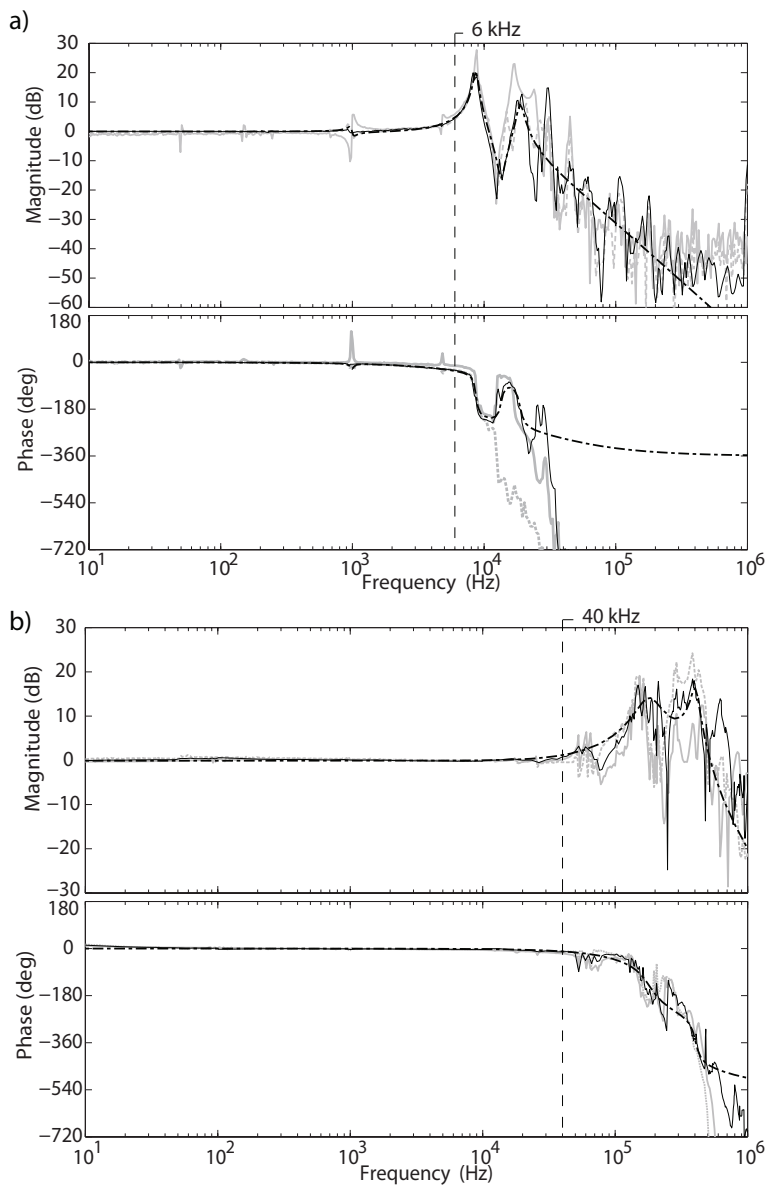


Figure 4.4: Frequency responses from the long-range actuator (a), and of the short-range actuator (b), for two different measurement runs (dashed and gray solid lines), the nonparametric nominal model (black, solid lines), and the parametric models capturing the nominal dynamics (black, dashed-dotted lines).

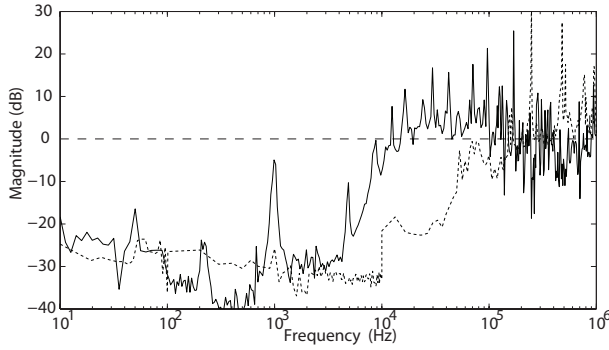


Figure 4.5: Bode magnitude plot of the multiplicative dynamic uncertainty $\Theta_l(\omega_f)$ for the long-range actuator (solid) and for the short-range actuator (dashed).

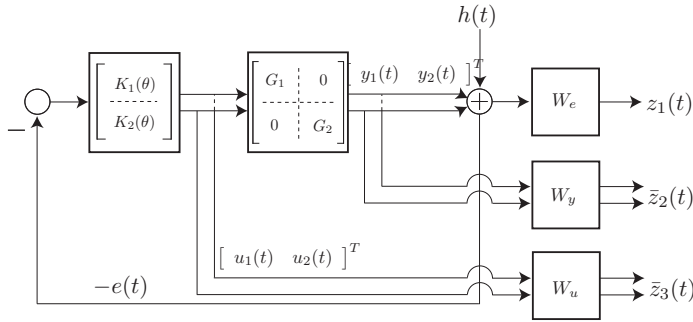


Figure 4.6: Block diagram of the dual actuated system representation used for controller synthesis, with controller $K(\theta)$, plant dynamics G , and weighting filters W_e , W_y , and W_u .

the weighting filters on the controller outputs $W_u(s) = \text{diag} [W_{u1}(s), W_{u2}(s)]$. The optimization objective is to find the parameters $\hat{\theta}$ of the controller $K(s, \theta) = [K_1(s, \theta) \quad K_2(s, \theta)]^T$ which minimizes the H_∞ -norm of the system:

$$\gamma \geq \min_{\theta} \left\| \begin{array}{c} W_e(s) \cdot S(s, \theta) \\ W_y(s) \cdot T(s, \theta) \\ W_u(s) \cdot S(s, \theta) \cdot K(s, \theta) \end{array} \right\|_{\infty}, \quad (4.4)$$

with upper-bound γ , the sensitivity function $S(s, \theta) = (1 + \sum G_l(s) \cdot K_l(s, \theta))^{-1}$, and the transfer from the topography signal $h(t)$ towards the individual actuator outputs $T(s, \theta) = G(s) \cdot K(s, \theta) \cdot S(s, \theta)$.

The weighting filters are used to enforce the desired behavior on the closed-loop system. Figure 4.7 shows the Bode magnitude responses of the individual (inverted) weighting filters together with the corresponding transfer function of the resulting closed-loop system. The most important criterion is the disturbance rejection, which is enforced by choosing the weighting filter $W_e(s)$ as an inverse

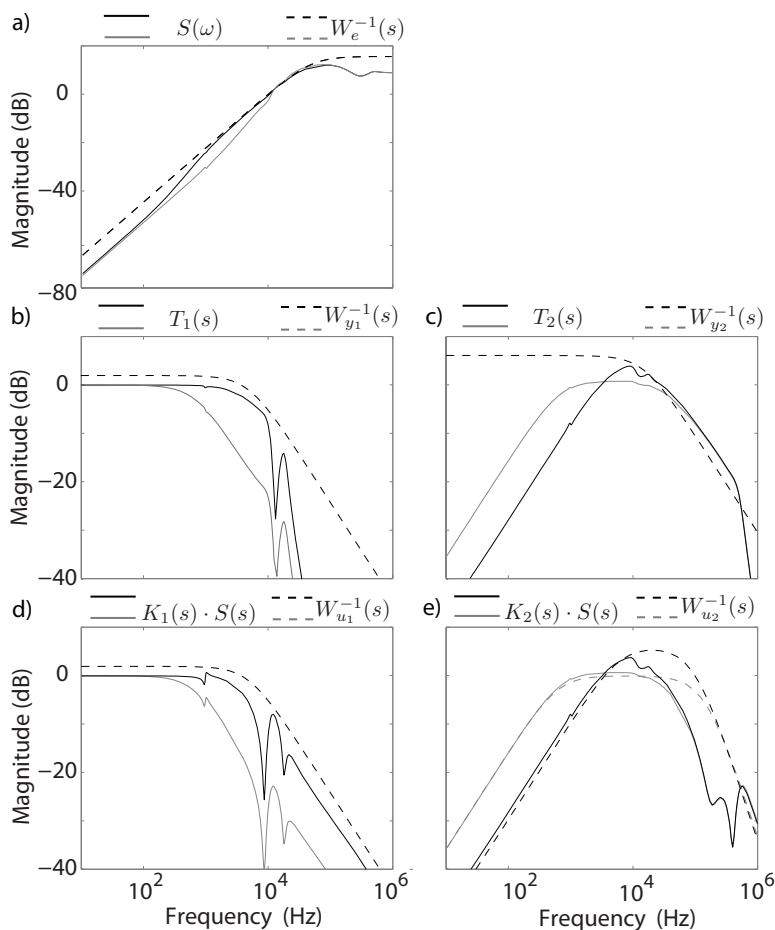


Figure 4.7: Bode magnitude plots of the closed-loop systems resulting from the model-based controller synthesis, and the corresponding weighting filters. The black lines correspond to the design case aimed for the higher transition frequency (2.5 kHz) between both actuators and the gray lines correspond to the design case aimed for the lower transition frequency (500 Hz).

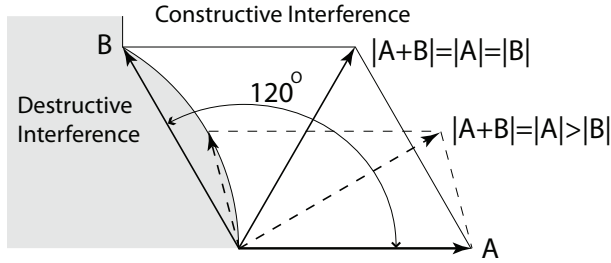


Figure 4.8: Illustration of the domains of constructive and destructive interference of the two actuator outputs which are represented by vectors A and B. Depending on the difference in magnitude of both vectors the destructive interference (i.e. $|A + B| < \max\{|A|, |B|\}$) starts at a phase difference of 90 up to 120 degrees.

high-pass filter (cf. Fig. 4.7a), pushing the bandwidth as high as possible. As discussed in Section 4.2.2 the actuation bandwidths should be limited to 6 kHz for the long-range actuator and 40 kHz for the short-range actuators to prevent instability due to excitation of the uncertain dynamics. To this end, weighting filters $W_{u_1}^{-1}(s)$, $W_{y_1}^{-1}(s)$, and $W_{y_2}^{-1}(s)$ are chosen as first order low-pass filters with corresponding cutoff frequencies. The DC-gain of these filters is set to 2 in order not to put too strong weights on potential peaking above the 0 dB line of these transfer functions, that naturally occurs just before the cross-over frequency (cf. Fig. 4.7b-d). Weighting filter $W_{u_2}^{-1}(s)$ is chosen to provide a 2nd order roll-off in order to enforce a steeper roll-off of the controller output for the short-range actuator at higher frequencies (cf. Fig. 4.7e). To enforce the frequency separation between both actuators, a weight is put on the control action of the short-range actuator at lower frequency via weighting filter $W_{u_2}^{-1}(s)$. This frequency separation should be carefully designed to minimize the chance of saturation of the short-range actuator during imaging, as discussed in the following section.

Frequency separation

One important design aspect for dual actuated systems is that both actuators may start to negate part of each others motion if the phase difference between both control paths gets too large in a particular frequency region, as discussed in [87]. This destructive interference among both actuators is sometimes referred to as ‘actuator fighting’. Actuator fighting should be avoided as this could result in large and inefficient controller outputs, which may in turn cause undesirable excitation of uncertain dynamics and may increase the chance of actuator saturation during imaging.

When actuator fighting occurs in a particular frequency region the magnitude of the overall complementary sensitivity function (i.e. the sum of the actuator outputs) is smaller than the largest magnitude of the individual actuator outputs in that frequency region; $|T_1(\omega) + T_2(\omega)| < \max\{|T_1(\omega)|, |T_2(\omega)|\}$. As depicted in Figure 4.8 this destructive interference between the two actuators can

start anywhere between a phase difference of 90° for $\min\{|T_1(\omega)|, |T_2(\omega)|\} \ll \max\{|T_1(\omega)|, |T_2(\omega)|\}$ up to 120° at the transition frequency $|T_1(\omega)| = |T_2(\omega)|$.

To prevent too large phase differences the transition between both actuators is restricted to a first order roll-on for the short-range actuator at lower frequency, i.e. having a 90° phase lead with respect to the long-range actuator. After the transition frequency $\omega_t \mid \{|T_1(\omega_t)| = |T_2(\omega_t)|\}$ the phase difference between both control paths is largely determined by the roll-off of the long-range actuator. Naturally one would like to choose the transition frequency as high as possible to make maximum use of the positioning range of the long-range actuator. However, the transition frequency should not be chosen too high, as this might require a steeper roll-off for the long-range actuator to provide sufficient attenuation of its uncertain dynamics at higher frequencies. Such rapid roll-off would result in large phase differences between both control paths, and consequently strong actuator fighting. Therefore, careful choice of the transition frequency is required to minimize the chance of actuator saturation given the expected spectrum of the sample topography signal to be tracked by the dual actuated AFM system.

During typical AFM imaging experiments, the sample topography signal to be tracked by the feedback loop can be split into low frequency components that have a larger amplitude, stemming mainly from a possible tilt of the sample, and smaller amplitude, high frequency components stemming from the actual nano-scale sample topography. Consequently, the sample topography signal has a predominantly triangular shape (in time domain), with a base frequency equal to the line-scan frequency and an amplitude spectrum which decays inversely proportional to the frequency. In order to minimize the actuator fighting at higher frequencies, the transition frequency between both actuators is chosen such that the long-range actuator has just sufficient bandwidth to track the height variations due to the sample tilt. As this particular system is designed for a scanning speed of up to about 50 Hz, a tracking bandwidth of about 500 Hz would be sufficient for the long-stroke actuator to track the height variations due to a tilt of the sample up to the 9th the harmonic. To enforce this actuator transition in the controller synthesis the weighting filter $W_{u2}^{-1}(s)$ is provided with a first order high-pass behavior with a cornering frequency of 500 Hz. The maximum gain of $W_{u2}^{-1}(s)$ is set to 1 in order to provide a higher weighting on any potential peaking of the short-range actuator controller output associated with fighting of the actuators (cf. Fig. 4.7e, gray lines).

In order to illustrate the importance of choosing the transition frequency between both actuators carefully, a second design case is considered in which the transition frequency is chosen such that the actuation bandwidth of the long-range actuator is pushed to its maximum of 6 kHz. In this case weighting filter $W_{u2}^{-1}(s)$ is provided with a maximum gain of 2 and a high-pass behavior of which the cornering frequency is tuned towards the point that an actuation bandwidth of 6 kHz is achieved for the long-range actuator.

Synthesis results

The controller synthesis is performed using the Robust Control Toolbox of `matlab`, which in both cases results in $\gamma \leq 1.5$ (cf. Eqn. (4.4)) and the closed-

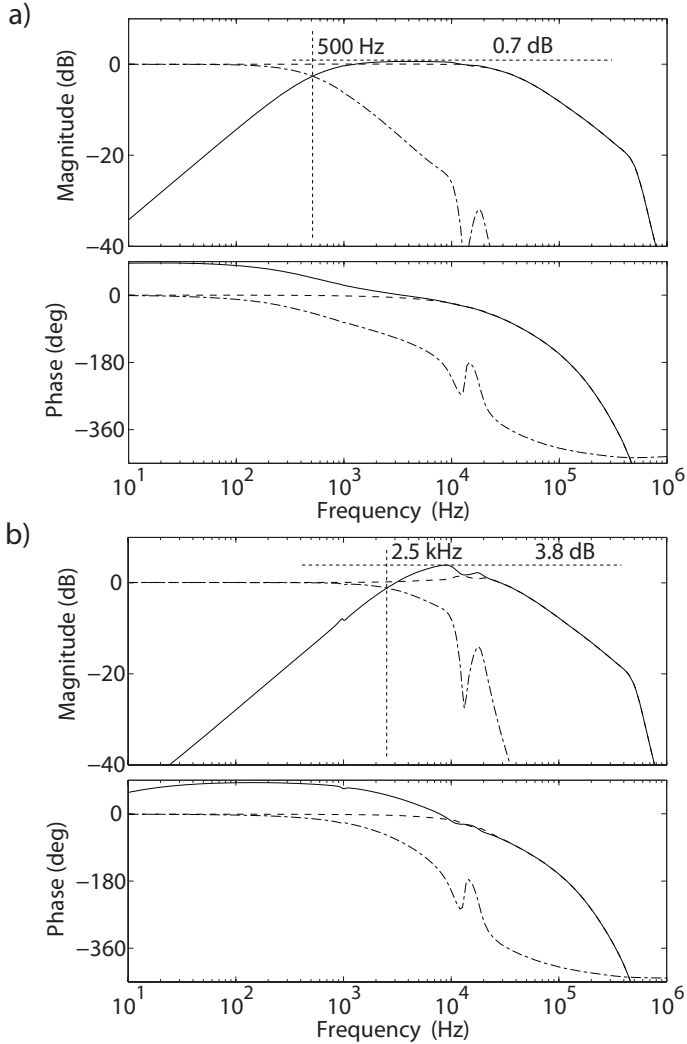


Figure 4.9: Frequency response plots of the complementary sensitivity function (dashed) $T(\omega)$, the control action of the long-range actuator $T_1(\omega)$ (dashed-dotted), and the control action of the short-range actuator $T_2(\omega)$ (solid) for the closed-loop controlled system with a lower transition frequency of 500 Hz between both actuators (a), and with a higher transition frequency of 2.5 kHz between both actuators (b).

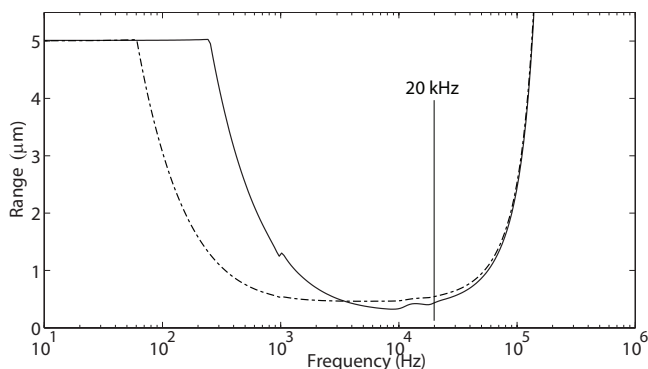


Figure 4.10: The maximum allowable disturbance amplitude $h_{max}(\omega)$ before saturation of one of the control paths occurs as a function of frequency. The dashed-dotted line corresponds to the closed-loop controlled system with the lower transition frequency between both actuators, and the solid line corresponds to the system with a higher transition frequency. The line at 20 kHz marks the disturbance rejection bandwidth of the system.

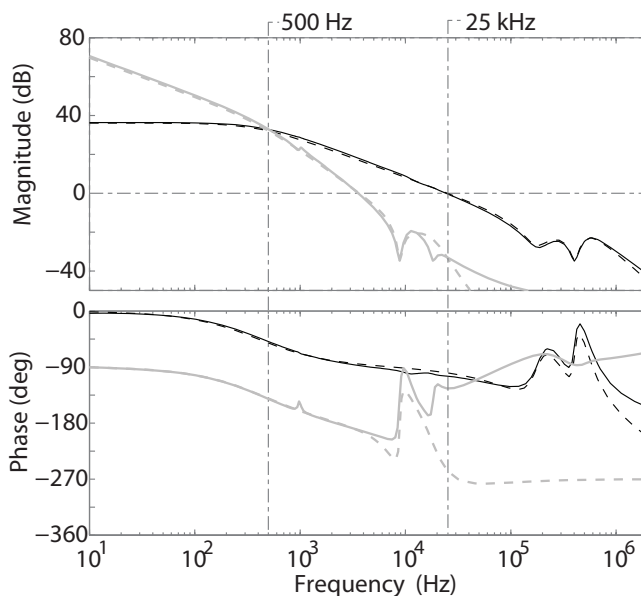


Figure 4.11: Bode plots of the controllers K_1 (gray lines) and K_2 (black lines) with full order (solid lines) and after order reduction (dashed lines).

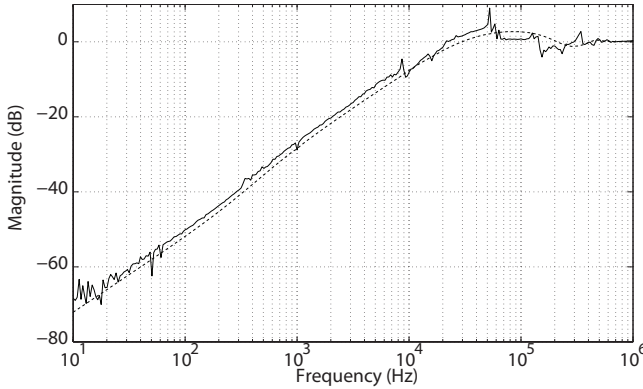


Figure 4.12: Frequency response of the measured (solid) and modeled (dashed) sensitivity function of the dual actuated AFM.

loop system responses are close to the corresponding inverse weighting filters, as can be seen in Figure 4.7. For both design cases a disturbance rejection bandwidth is achieved of about 20 kHz (cf. Fig. 4.7a), and a tracking bandwidth of 40 kHz (cf. Fig. 4.7c). As can be seen from Figures 4.7c and 4.7d, the controller and actuator outputs of the short-range actuator are slightly exceeding the magnitudes of the corresponding inverse weighting filters, which is due to the fact that the overall disturbance rejection bandwidth, governed by $W_e(s)$, is pushed as far up as possible. However, by applying μ -analysis based on the nonparametric frequency response model of Equation (4.3) it is verified that for both design cases the closed loop system is robustly stable against the dynamical variations of the system, as discussed in more detail in Section 4.3.

The differences between both design cases are clearly revealed when comparing the contributions of both actuators. Figure 4.9 shows the complementary sensitivity functions of both design cases along with the contributions of the long-range actuator (dash-dotted lines) and the short-range actuator (solid lines). In the first design case (Fig. 4.9a) the transition frequency between both actuators is at 500 Hz, and the peak gain of the short-range actuator is 0.7 dB (Fig. 4.9a), whereas in the second design case the transition frequency is at 2.5 kHz, and the peak gain of the short-range actuator is 3.8 dB (Fig. 4.9b). At these peaks of the short-range actuator output it can be seen that the magnitude of the complementary sensitivity function of the total system (dashed line) is significantly lower, which indicates that in those frequency regions the actuators are negating part of each others motion, i.e. they are ‘fighting’ each other.

The positioning range for both actuators is limited by the maximum output ranges of their respective high voltage amplifiers. The maximum topography variation that can be tracked by the system before either one of the amplifiers reaches its maximum range can be calculated at each frequency point by:

$$h_{max}(\omega) = \min \left\{ \frac{u_{1max}}{|S(i\omega) \cdot K_1(i\omega)|}, \frac{u_{2max}}{|S(i\omega) \cdot K_2(i\omega)|} \right\}, \quad (4.5)$$

with $u_{1_{max}}$, and $u_{2_{max}}$ the maximum output ranges of the respective amplifiers, and correspond to a range of $5 \mu\text{m}$ and $0.5 \mu\text{m}$ for the long-range and short-range actuator respectively. Figure 4.10 shows the calculated maximum allowable topography variation before saturation of one of the actuators $h_{max}(\omega)$ for both design cases. At lower frequency ($< 60 \text{ Hz}$) both designs utilize the full positioning range of the long-range actuator of $5 \mu\text{m}$. Beyond the disturbance rejection bandwidth of 20 kHz both plots show a steep incline due to the fact that beyond this bandwidth the actuators are not tracking the sample profile anymore and actuator saturation is less likely to happen. However, in the intermediate frequency region between 60 Hz and 20 kHz the allowable topographic variation $h_{max}(\omega)$ is restricted by the limited positioning range of the short-range actuator (cf. Fig. 4.10). For the design case (a) with the lower transition frequency between both actuators, the allowable disturbance $h_{max}(\omega)$ starts to roll-off at about 60 Hz , while for the design case (b) with the higher transition frequency this roll-off starts only at 220 Hz . However, the roll-off for design case (b) is steeper and goes down to a minimum of $0.33 \mu\text{m}$ at a frequency of 8 kHz , as compared to a minimum of $0.47 \mu\text{m}$ at a frequency of 3 kHz for design case (a). Hence, due to the actuator fighting at those frequencies, the effective positioning range is reduced by 6% and 34% respectively, of the $0.5 \mu\text{m}$ full positioning range of the short-range actuator. Figure 4.10 shows that due to the actuator fighting problem in dual actuated AFM, a design trade-off has to be made between the positioning range at lower frequencies, and the positioning range at higher frequencies.

The comparison between the two design cases illustrates that pushing the bandwidth of the long-range actuator higher than necessary might compromise the positioning range at higher frequencies due to the large phase differences between both control paths. Although the second design provides a large positioning range at lower frequencies, the reduction in positioning range beyond 2.5 kHz may pose higher chance of saturation of the short-range actuator while imaging rough sample surfaces at high speeds. Moreover, the larger actuator fighting in the second design case may also cause stronger excitation of the uncertain dynamics of the system in those frequency regions (cf. Fig. 4.5), which might degrade the reliability of the topography estimate as discussed in Chapter 3. Therefore, in the sequel of this chapter only the first controller design is considered.

Controller reduction and implementation

The resulting feedback controller from the model-based controller synthesis is an 18th order system with a single input and two outputs (SITO). The frequency response plots of the controller are depicted in Figure 4.11, showing that $K_1(s)$ has a high feedback gain predominantly at lower frequencies while the feedback gain of $K_2(s)$ is larger than $K_1(s)$ at frequencies above the transition frequency of 500 Hz , resulting in the frequency separation between both actuators. To facilitate implementation, the controller is split into two SISO controllers that are reduced via the balanced truncation method [90] to 6th and 7th order for the long-range and short-range actuator, respectively. The frequency responses of the reduced order controller are shown in Figure 4.11 (dashed lines) as well, showing only small deviations with respect to the full-order controllers within the respective actuation

bandwidths.

The feedback controllers are implemented using an *Field-Programmable Gate Array* (FPGA, Virtex-II Pro XtremeDSP Development Kit, Nallatech, Camarillo CA, USA), which runs at a sampling frequency of 65 Mhz. To minimize the quantization effects on the actual pole-locations the input data is down-sampled internally by a factor of 100 for the implementation of poles and zeros for controller $K_1(s)$, and by a factor of 15 for the implementation of the poles and zeros of controller $K_2(s)$. For this implementation the poles and zeros of the respective notch filters are grouped in a biquad structure and discretized using bilinear (Tustin) transformation via the `c2d.mat` command of `matlab`. The FPGA adds an additional 400 ns delay to the feedback loop which results in a phase lag of about 4 degrees at the 0 dB crossing of the loop gain of the short-range actuator at 25 kHz, which is well within in the phase margin of the control system and does not influence the system performance considerably.

In order to analyze the performance of the newly designed dual actuated AFM, the disturbance rejection bandwidth is measured using the network analyzer. Figure 4.12 shows the measured frequency response of the sensitivity function with a bandwidth of 20 kHz, which closely matches with the sensitivity function calculated based on the dynamical models as shown by the dashed lines in Figure 4.12.

4.3 Anti-windup⁴ control for dual actuated AFM

Due to the limited positioning range of the short-range actuator, saturation of this actuator might occur at large topography variations of the sample when scanning at high speed, or due to accidental large disturbances. Although, the intended application of the dual actuated AFM is within its linear regime in which actuator saturation does not occur, to prevent damage to the overall system the controller should assure overall stability and fast recovery of the system if it accidentally enters the non-linear regime with actuator saturation. Therefore, firstly the stability of the uncertain closed-loop system with actuator saturation is analyzed by casting the problem into a Linear-Fractional-Transformation (LFT) (see for instance [90]). Secondly, based on the obtained LFT an anti-windup controller is proposed which provides global stability of the uncertain closed-loop system with constrained controller outputs for the short-range actuator.

4.3.1 Analysis saturation problem

In the following analysis the block structure is assumed as depicted in Figure 4.13a, with the designed feedback controller K , the uncertain actuator dynamics $\mathcal{G}(\omega_f, \Delta)$ (cf. Eqn. (4.3)). The block AW in Figure 4.13 is the to be designed

⁴The term 'windup' is most often associated with integrator-windup, in which the integrator within the controller is accumulating energy while the system is in saturation, causing large overshoots when the system recovers from saturation. However, for the dual-actuated system considered in this research the windup is not limited to the state of the integrator as the entire system may become unstable when saturation of the short-range actuator occurs, as analyzed in Section 4.3.1.

anti-windup controller that feeds back the difference between the unconstrained and the constrained control signal for the short-range actuator, as is discussed in Section 4.3.2. The constrained controller output is given by:

$$\bar{u}_2(t) = \text{sat}(u_2(t)) = \begin{cases} \text{sign}(u_2(t)) \cdot u_{max} & , |u_2(t)| > u_{max} \\ u_2(t) & , |u_2(t)| \leq u_{max} \end{cases} \quad (4.6)$$

Figure 4.13b shows an alternative representation of this saturation problem where the saturation non-linearity is replaced by a dead-zone non-linearity [25], of which the output equals the difference between the unconstrained and constrained controller output:

$$\tilde{u}_2(t) = \phi(u_2(t)) = u_2(t) - \bar{u}_2(t) = u_2(t) - \text{sat}(u_2(t)). \quad (4.7)$$

The dead-zone non-linearity $\phi(u_2(t))$ can be seen as a non-linear gain belonging to the sector $[0,1]$, and is interconnected with the transfer from $\tilde{u}_2(t)$ towards $u_2(t)$ denoted $P(\omega_f, \Delta)$ which contains the system dynamics (cf. Fig. 4.13b):

$$P(\omega_f, \Delta) = \frac{K_2(i\omega_f) (\mathcal{G}_2(\omega_f, \Delta_2) - AW(i\omega_f))}{1 + K(i\omega_f) \cdot \mathcal{G}(\omega_f, \Delta)}, \quad (4.8)$$

Following the ‘loop transformation’ procedure as described in [25], this interconnected system can be normalized by defining $[\psi(u_2) = 2 \cdot \phi(u_2) - I]$ which belongs to the sector $[-1,1]$, and

$$P_s(\omega_f, \Delta) = \frac{0.5 \cdot P(\omega_f, \Delta)}{1 + 0.5 \cdot P(\omega_f, \Delta)}. \quad (4.9)$$

By also pulling out the dynamical uncertainty Δ the system can be represented by the LFT of Figure 4.13c. Based on this LFT the robustness of the system can be analyzed for both the dynamical uncertainty Δ as well as the non-linearity posed by the actuator saturation by applying μ -analysis [90]. Global asymptotic stability of the system is assured when the calculated Structured Singular Value (SSV) $\mu(\omega)$ of the system is smaller than one for all frequencies ($\mu(\omega) \leq 1, \forall \omega \in \Omega_f$), which is implemented via the `mussv.mat`-function of the robust control toolbox of `matlab`.

The black solid line of Figure 4.14 shows the calculated SSV-plot for the system when only regarding the dynamical uncertainty Δ , and the actuator saturation is neglected. As for this case the SSV-plot is below the 0 dB line for all frequencies, it can be concluded that the feedback controller K designed in the previous section indeed provides robust stability of the system within the unconstrained, linear operating regime. The dashed black line of Figure 4.14, however, shows the SSV-plot when taking the actuator saturation into account, but without implementation of an anti-windup controller (i.e. $AW = 0$). As for some frequencies this SSV-plot exceeds the 0 dB line, global asymptotic stability of the system without anti-windup controller cannot be guaranteed. Based on experimental results (data not shown) it is found that the constrained system without anti-windup controller is indeed getting unstable when tracking step-like feature that are slightly larger than 1 μm .

4.3.2 Anti-Windup controller design

The stability issues associated with the saturation of the short-range actuator in dual actuated systems has been addressed in literature for dual actuated HDD-system. In [34] a solution is provided to guarantee stability of dual actuated systems designed according to the decoupled Master/Slave structure. In [39] a more general solution is presented to synthesize both full-order and reduced order anti-windup controllers for dual actuated feedback systems. However, these methods assume accurate knowledge of the actuator dynamics, and therefore do not allow to directly take into account the dynamical uncertainty of the actuators. Alternatively, in this section the anti-windup controller structure is designed following the Internal Model Control (IMC) [105] method. Following this IMC method the anti-windup filter AW is designed to match the nominal dynamics of the short-range actuator, and is implemented following the structure as shown in Figure 4.13a. During saturation of the short-range actuator, the anti-windup controller AW mimics the dynamical behavior of the short-range actuator such that the rest of the loop is not affected by the saturation. When taking the anti-windup controller as the non-parametric nominal frequency response model $AW(\omega) = \Gamma_2(\omega)$ as derived in Section 4.2.2, the calculated SSV-plot exactly overlaps that of the unconstrained system (black solid line of Fig. 4.14). Hence, when the anti-windup controller AW matches the nominal frequency response of the short-range actuator, it fully compensates for the stability issues associated with the saturation of the short-range actuator.

For practical implementation of the anti-windup controller, however, the anti-windup controller needs to be designed in a finite order parametric sense. An important design consideration hereby is that although using a high order model for the anti-windup controller which closely matches the nominal dynamics of the short-range actuator $\Gamma_2(\omega)$ may provide the best robust stability of the system, the transient behavior of the system may be compromised by such a high order anti-windup controller. This results from the energy build up in the dynamical model AW during the saturation phase which can cause oscillations as soon as the system recovers from saturation, particularly when AW contains weakly damped resonant modes [105]. Moreover, the use of a high order anti-windup controller might not always be implementable or may consume a lot of computational power of the real-time hardware. However, as for this particular system the feedback bandwidth of 40 kHz is well below the first fundamental resonance frequency of the short-range actuator at 150 kHz (cf. Fig. 4.4), it is adequate to consider the short-range actuator as a static gain in the design of the anti-windup controller: $AW = G_2(s = 0)$. The use of such a static anti-windup controller requires minimal computation power, and problems with poor transient performance associated with energy buildup in AW does not occur. Figure 4.14 (gray solid lines) shows the calculated SSV-plot for the system with the static anti-windup controller, showing that although the robust stability is slightly less than in case of the unconstrained system, the SSV-plot is smaller than 0 dB over all frequencies, and therefore global asymptotic stability of all systems within the uncertainty set of Equation 4.3 is guaranteed.

4.3.3 Experimental validation of the Anti-Windup controller

The static anti-windup controller is implemented on the FPGA along with the designed feedback controller. Figure 4.15 shows the response of the dual actuated AFM prototype system to a step at the input with a height of $1 \mu\text{m}$, with and without the proposed static anti-windup controller. In the case without the anti-windup controller (dashed lines) large oscillations are visible in both the error signal as well as in the control signals for the long- and short-range actuator, while in the case with the static anti-windup controller (solid lines) a smooth recovery from the actuator saturation can be seen. Experiments demonstrate (data not shown) that the system without anti-windup controller goes unstable for step inputs slightly larger than $1 \mu\text{m}$, while the system with the static anti-windup controller is stable over the entire working range. Hence, the static anti-windup controller is a simple but essential extension of the dual-actuated control system, which guarantees stability of the system under all imaging conditions.

4.4 Imaging results

In order to demonstrate the benefits of dual actuation to control the tip-sample force in AFM, three sets of AFM images are captured with different feedback controllers:

1. The single actuated system with a conventional, well-tuned Proportional Integral (PI) controller, which is the standard controller of the `MultiMode V` system, and achieves a disturbance rejection bandwidth of 400 Hz.
2. The single actuated system with a model-based feedback controller, which is designed according to the procedure as described in [84], and achieves a disturbance rejection bandwidth of about 1 kHz.
3. The newly designed dual actuated system with model-based feedback controller with the disturbance rejection bandwidth of 20 kHz (cf. Fig. 4.12) and the designed anti-windup controller.

Figure 4.16a-c show AFM-images of the same area of a calibration grating with step height of 200 nm, and $10 \mu\text{m}$ pitch obtained at a scan-speed of 2 lines per second with the prototype AFM system, controlled by the three different controllers. The 'height' images are obtained in the conventional way by a calibrated scaling of the feedback controller output $u(t)$, where for the dual actuated case this is a calibrated summation of the two controller outputs. The 'cantilever deflection' images are directly obtained from the measured cantilever deflection output, and reveal the control error of the feedback loop.

Figure 4.16 clearly shows that the cantilever deflection of the model-based single actuated system is significantly smaller than the cantilever deflection obtained with the single actuated PI controlled AFM as a result of the higher control bandwidth. For the dual actuated AFM (Fig. 4.16c) the cantilever deflection is even

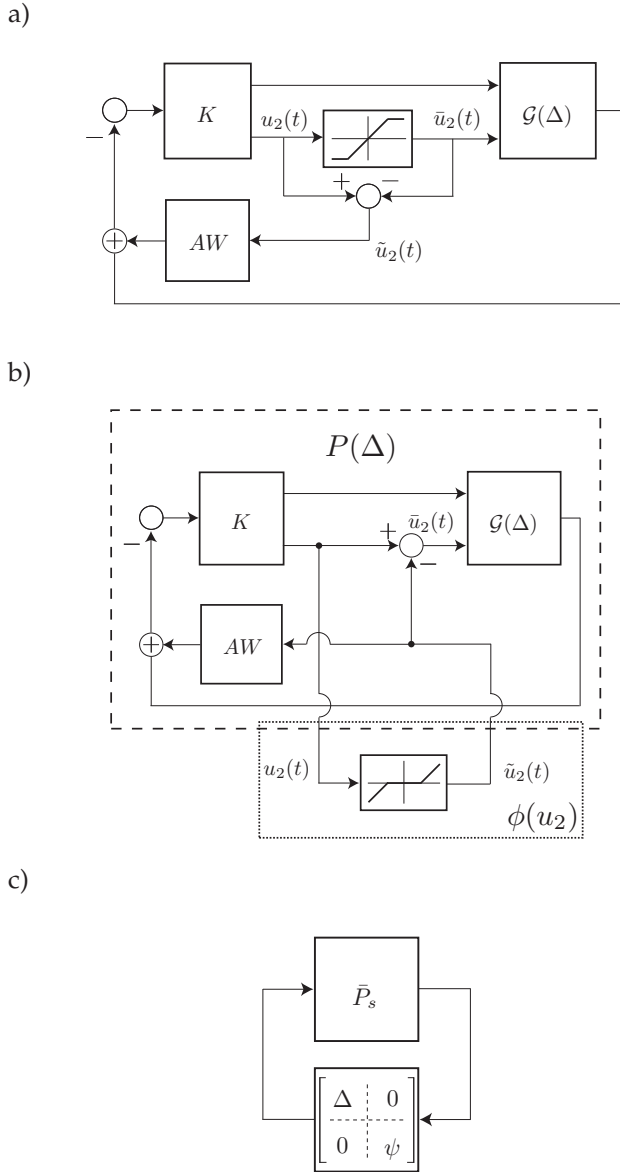


Figure 4.13: (a) Block diagram of the constrained dual actuated system with anti-windup compensator AW . (b) Alternative system representation where the saturation block is replaced by a dead-zone non-linearity. (c) Linear Fractional Transformation of the normalized system \bar{P}_s interconnected with the dynamical uncertainty Δ and the normalized output non-linearity ψ .

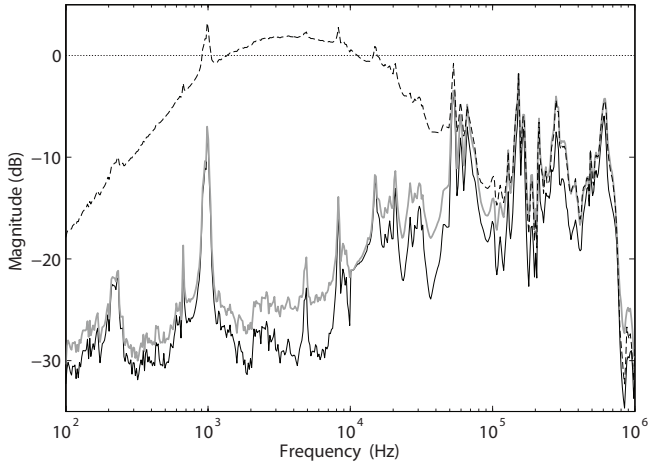


Figure 4.14: Structured Singular Value (SSV) plot for the unconstrained system, disregarding the actuator saturation (black, solid line), for the constrained system without anti-windup controller $AW(s) = 0$ (black, dashed line), and for the constrained system with a static anti-windup controller $AW = G_2(s = 0)$ (gray solid line).

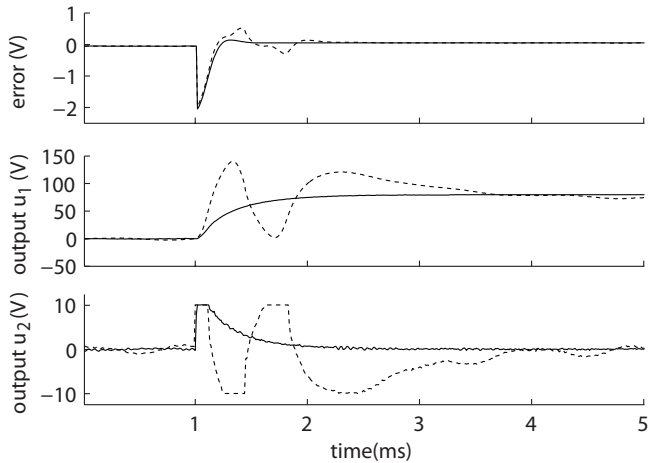


Figure 4.15: Measured system response to a reference step input of about $1 \mu m$ which results in saturation of the control output for the short-range actuator ($u_2(t)$), shown with (solid) and without (dashed) static anti-windup compensation.

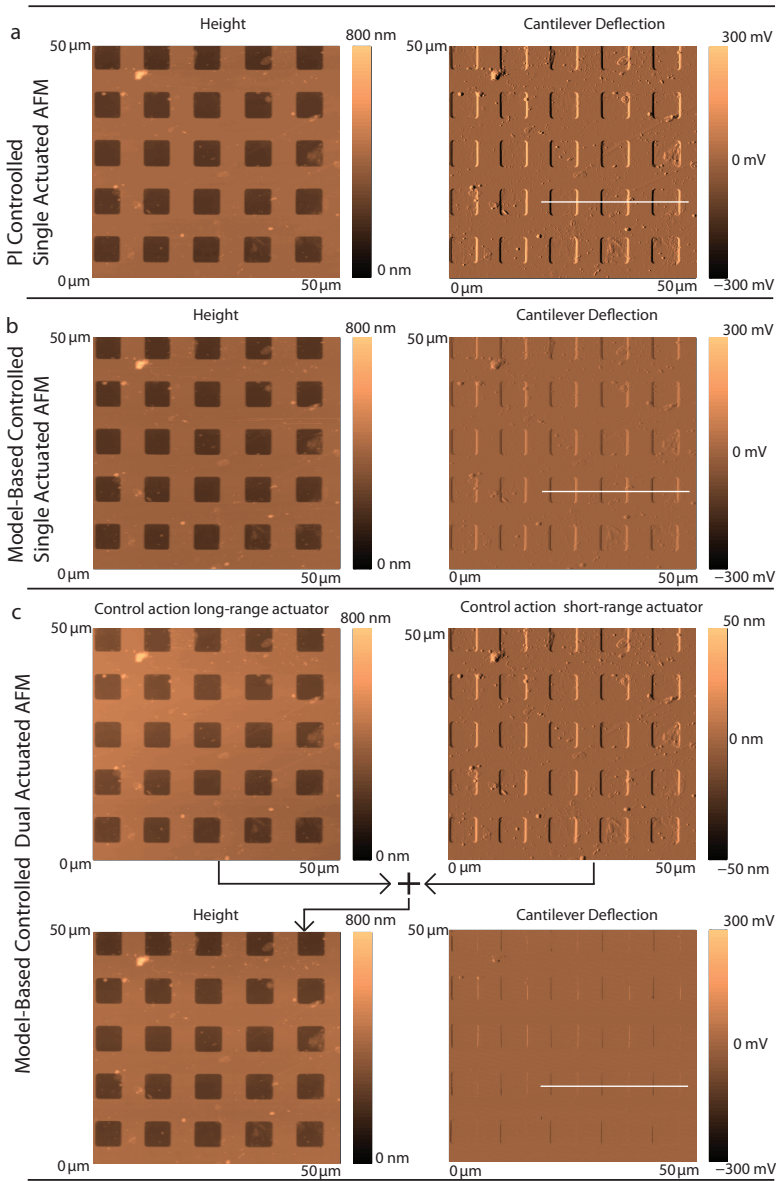


Figure 4.16: AFM images of the same area of a silicon calibration grating (10 μm pitch, 200 nm step height), obtained with the single actuated PI controlled AFM (a), the model-based controlled single actuated AFM (b), and the proposed model-based dual actuated AFM (c). The images recorded with the dual actuated AFM show a significant reduction of the cantilever deflection, and thus reduced force variations between the measurement tip and the sample, as compared to the single actuated AFM. The white line in the deflection images indicates the cross-sections shown in Figure 4.17.

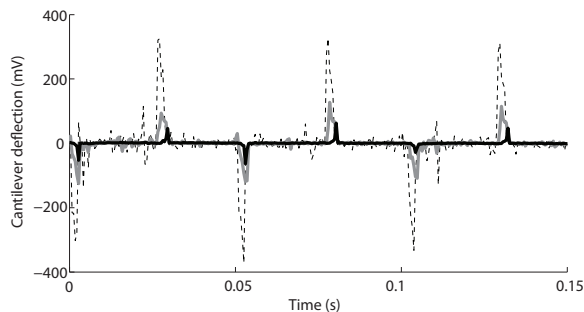


Figure 4.17: Cross-section of the cantilever deflection signal for the PI-controlled single actuated AFM (dashed, black), the single actuated AFM with model-based control (solid, gray), and the dual actuated AFM (solid, black).

further reduced, only showing small variation around the sharp edges of the calibration grating. Figure 4.17 shows cross-sections of the different cantilever deflection images as marked by the white lines in the deflection images in Fig. 4.16, confirming that with the dual actuated AFM the cantilever deflection is significantly reduced as compared to both single actuated AFMs. Figure 4.16c also shows images of the feedback controller outputs for both actuators in the dual actuated case, demonstrating that the long-range actuator tracks the larger amplitude, low frequency topography variations, while the short-range actuator only tracks the high frequency topography variations that otherwise would occur in the cantilever deflection image (cf. Fig. 4.16a).

As demonstrated by Figure 4.16 the higher control bandwidth in the dual actuated case results in less force variations between the tip and the sample and thus more gentle probing of the sample, which is particularly important when imaging fragile biological samples. The improved disturbance rejection bandwidth of the dual actuated AFM would allow 50 times faster imaging as compared to the single actuated AFM with the standard PI controller, and 20 times faster imaging as compared to the single actuated AFM with the model-based controller with equally large force variations between the tip and the sample.

4.5 Addressing the topography estimation accuracy for dual actuated AFM

While in the previous sections of this chapter the influence of the feedback controller on the accuracy of the topography estimate is neglected, as is done in conventional feedback controller design for AFM, in this section integrated design of the feedback controller and topography estimator for dual actuated AFM is investigated, following the methodology discussed in Section 3.3. To demonstrate the consequences of addressing the accuracy of the topography estimate in the design

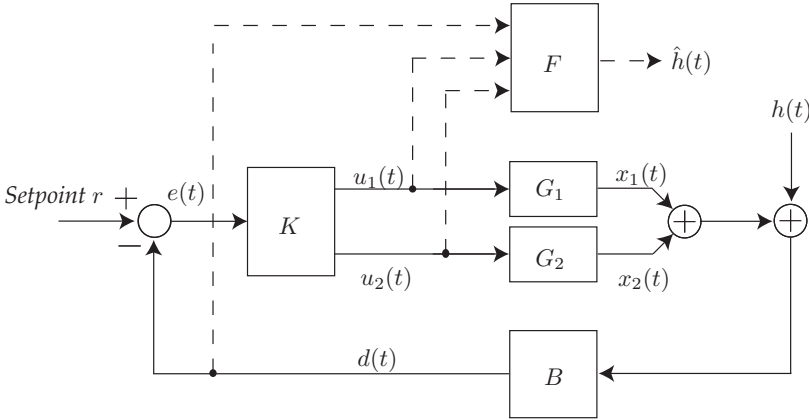


Figure 4.18: Block diagram depicting dual actuated control of the tip-sample force, including the topography estimator. The sample topography is estimated based on the measured cantilever deflection $d(t)$, and the controller outputs $u_1(t)$ and $u_2(t)$, corresponding to the long-range and short-range actuators respectively.

of the feedback controller, two different design cases are compared with different emphasis on the topography estimation accuracy.

4.5.1 Topography estimation in dual actuated AFM

While the representation of the AFM images of Figure 4.16 is done similar as in the conventional AFM, the accuracy and bandwidth of the topography estimate may be significantly improved by taking into account the system dynamics, as discussed in Section 3.2. For the topography estimation in dual actuated AFM three signals are available: the cantilever deflection signal $d(t)$, and both controller outputs $u_1(t)$, and $u_2(t)$. Therefore, the topography estimation in dual actuated AFM can be represented in as:

$$\begin{aligned}\hat{h}(t) &= F(p) \cdot [d(t) \quad u_1(t) \quad u_2(t)]^T \\ &= F(p) \cdot \left[\frac{B(p)}{1+L(p)} \quad -\frac{B(p) \cdot K_1(p)}{1+L(p)} \quad -\frac{B(p) \cdot K_2(p)}{1+L(p)} \right]^T \cdot h(t),\end{aligned}\quad (4.10)$$

with $L(p) = [G_1(p) \quad G_2(p)] \cdot [K_1(p), K_2(p)]^T \cdot B(p)$ the loop gain, $B(p)$ the sensor dynamics (cf. Fig. 3.1), and $F(p)$ the topography estimator of the dual actuated AFM. This topography estimator is the extended version of the topography estimator for the single actuated AFM as presented in Equation (3.7), and is given by:

$$F(p) = F_2(p) \cdot \underbrace{\left[\hat{B}^{-1}(p) \quad -\hat{G}_1(p) \quad -\hat{G}_2(p) \right]}_{F_1(p)} \quad (4.11)$$

with $F_2(p)$ the filter that handles the noise as derived in Equation (3.6), $\hat{B}(p)$ a model of the sensor dynamics, and $\hat{G}_1(p)$ and $\hat{G}_2(p)$ the models of the long-range, and short-range actuator dynamics, respectively. Hence, the dual actuated feedback loop with the topography estimator can be presented as in the block diagram of Figure 4.18. When assuming the noise is zero, the noise filter $F_2 = 1$ (cf. Section 3.2), the transfer from topography signal $h(t)$ towards the topography estimation error $\varepsilon(t) = \hat{h}(t) - h(t)$ can be derived as:

$$\begin{aligned} & \left[F_1(p) \cdot \left[\frac{B(p)}{1+L(p)} \quad -\frac{B(p) \cdot K_1(p)}{1+L(p)} \quad -\frac{B(p) \cdot K_2(p)}{1+L(p)} \right]^T - 1 \right], \\ & = \frac{\left[\hat{B}^{-1}(p)B(p) - 1 \right] + B(p)K_1(p) \left[\hat{G}_1(p) - G_1(p) \right] + B(p)K_2(p) \left[\hat{G}_2(p) - G_2(p) \right]}{1 + L(p)}, \end{aligned} \quad (4.12)$$

showing that the topography estimation accuracy is depending on the modeling error of the sensor dynamics, and the modeling error of the dynamics of both actuators. Recall from Section 3.2 that these modeling errors are inevitable due to the dynamical uncertainty of the system, which tends to become larger at higher frequency (cf. Fig. 4.4). Equation (4.12) also shows that the design of the feedback controller influences the propagation of the modeling errors for each individual actuator towards the topography estimation error. Hence, in dual actuated AFM not only the overall control bandwidth strongly influences the overall topography estimation accuracy, but also the individual control actions of each actuator.

4.5.2 Integrated design of the feedback controller and topography estimator for dual actuated AFM

In order to investigate the consequences of addressing the accuracy of the topography estimate in the design of the feedback controller for a dual actuated AFM, the design procedure presented in Section 3.3.2 is implemented for the dual actuated AFM. Similar as in Section 3.3.2, the influence of the measurement noise is not considered (i.e. $F_2 = 1$), and the sensor dynamics are assumed to be linear and fully known (i.e. $\hat{B} = B = 1$), as is a fair assumption for contact mode imaging with high resonance frequency cantilevers. As discussed in Section 3.3.2, dynamical uncertainty of the system can be addressed in the model-based design of the feedback controller via the overbounding function $Q(\omega_f) \geq \Psi(\omega_f)$, with $\Psi(\omega_f)$ the maximum multiplicative modeling error according to Equation (3.13). For the long-stroke actuator the maximum multiplicative modeling error $\Psi_1(\omega_f)$, and the 5th order overbounding function (denoted $Q_1(s)$ in this section) are shown in Figure 3.5. For the short-stroke actuator the maximum multiplicative modeling error $\Psi_2(\omega_f)$ and the corresponding 3th order overbounding filter denoted Q_2 are shown in Figure 4.19.

In order to demonstrate the integrated design of the feedback controller and topography estimator for dual actuated AFM, two different design cases are compared with different emphasis on the topography estimation accuracy. Similar to the situation discussed for the single actuated AFM in Section 3.4, the weighting filters on the topography estimation error are set as $W_{es} = 1$, and $W_{es} = 8$, for the design cases with lower and higher emphasis on the topography estimation accuracy, respectively. Given these weights on the topography estimation accu-

racy, both the cornering frequency of the weight W_e on the control error as well as the cornering frequency of the weight W_{u_2} on the controller output of for the short-range actuator (determining the transition frequency) are tuned up to the point that the μ -synthesis objective of $\gamma \leq 1$ is achieved (cf. Eqn. (3.14)). For both design cases the topography estimator is designed according to the procedure of Section 3.3.3, with two 30th order models of the actuator dynamics.

Figure 4.20 shows the sensitivity functions based on the nominal dynamical models, and Figure 4.21 (dashed lines) shows the nominal complementary sensitivity functions for both cases. Figures 4.20, and 4.21 show that both the disturbance rejection bandwidth (3.5 kHz versus 14 kHz), as well as the tracking bandwidth (7 kHz versus 25 kHz) is significantly lower in the case where $W_{es} = 8$. The dashed-dotted lines in Figure 4.21 shows the closed loop control action of the long-range actuator, while the solid lines show the control action of the short-range actuator for both design cases. For the design case $W_{es} = 8$ the resulting transition frequency between both actuators is revealed at 130 Hz, which is significantly smaller than the 840 Hz obtained in design case $W_{es} = 1$. In contrast, Figure 4.22 shows the worst-case magnitude of the transfer from topography signal $h(t)$ towards the topography estimation error $\varepsilon(t)$ of Equation (4.12). These graphs are calculated by substituting the designed feedback controller K , actuator models \hat{G}_l of the topography estimator, the data of the various frequency response measurements $\Upsilon_{l,j}(\omega_f)$ and $\hat{B} = B = 1$:

$$\max_{\substack{j \in [1 \dots n] \\ k \in [1 \dots m]}} \left| \frac{K_1(\omega_f) \cdot [\hat{G}_1(\omega_f) - \Upsilon_{1,j}(\omega_f)] + K_2(\omega_f) \cdot [\hat{G}_2(\omega_f) - \Upsilon_{2,j}(\omega_f)]}{1 + K_1(\omega_f) \cdot \Upsilon_{1,j}(\omega_f) + K_2(\omega_f) \cdot \Upsilon_{2,j}(\omega_f)} \right|,$$

with n and m the number of frequency responses measurements for the long-range and short-range actuator respectively, which in this case is 12 for both actuators as discussed in Section 4.2.2. Figure 4.22 shows that with the lower bandwidth in the case $W_{es} = 8$, also the worst-case topography estimation error is much smaller as compared to the design case with $W_{es} = 1$, especially at higher frequency and for instance in the frequency region of the first lateral resonance of the long-stroke actuator around 1 kHz. This is explained by the fact that with the lower actuation bandwidths of both actuators for design case $W_{es} = 8$ also the excitation of the uncertain dynamics is significantly smaller, which improves the accuracy of the topography estimation.

These results show that apart from the overall control bandwidth, for dual actuated AFM the transition among both actuators provides additional design freedom to improve the topography estimation accuracy in the intermediate frequency region. Typically the dynamical uncertainty of the long-range actuator grows faster with increasing frequency as compared to the short-range actuator (cf. Fig. 4.4). Therefore, besides the actuator fighting problem discussed in Section 4.2.3, the effects on the topography estimation accuracy are another argument not to make the transition frequency between both actuators much larger than strictly necessary in terms of positioning range. Furthermore, comparing these results with the results of the single actuated system discussed in Section 3.4 reveals that when considering the same specification for the topography estimation accuracy, the bandwidth of the dual actuated system is still significantly higher as compared

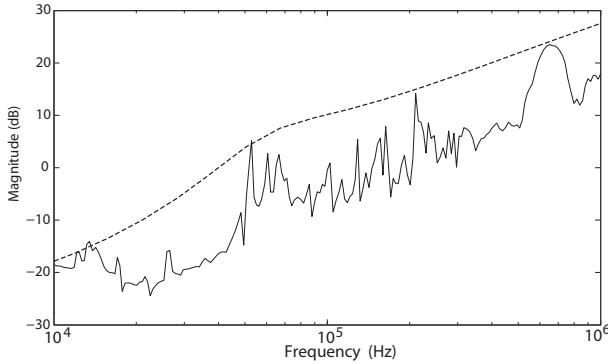


Figure 4.19: The maximum multiplicative modeling error of the structured dynamical model of the short-range actuator according to Equation 3.13 (solid line), and the overbounding filter Q_2 (dashed line).

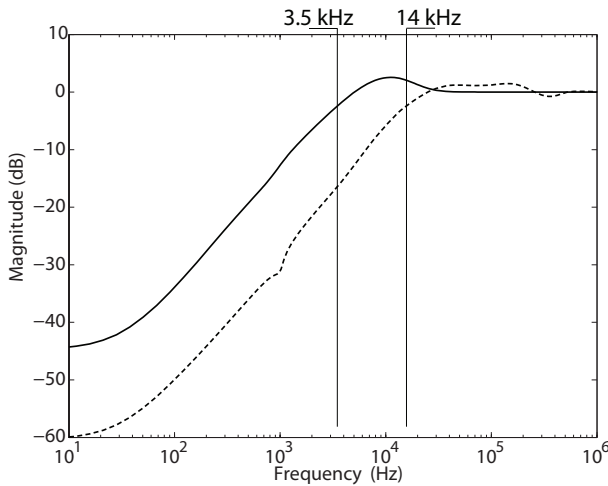


Figure 4.20: The nominal sensitivity functions of the dual actuated system designed with low emphasis on the topography estimation error $W_{es} = 1$ (dashed line) and with higher emphasis on the topography estimation error $W_{es} = 8$ (solid line).

to the single actuated system, i.e 3.5 kHz instead of 400 Hz for the design cases where $W_{es} = 8$.

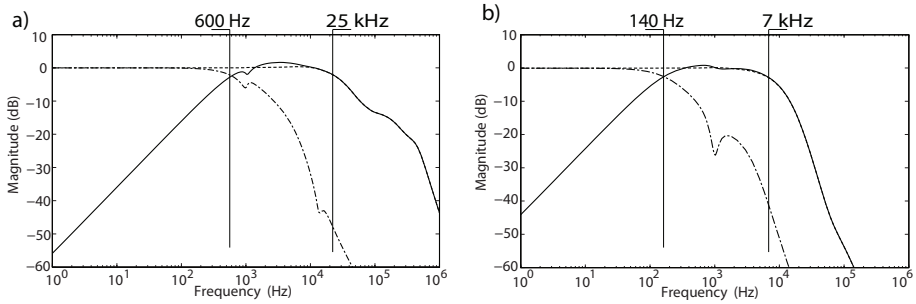


Figure 4.21: The nominal complementary sensitivity functions $T(\omega)$ (dashed lines), the control action of the long-range actuator T_1 (dash-dotted line), and the control action of the short-range actuator T_2 (solid line) of the dual actuated system, designed with low emphasis on the topography estimation error $W_{es} = 1$ (a) and with higher emphasis on the topography estimation error $W_{es} = 8$ (b).

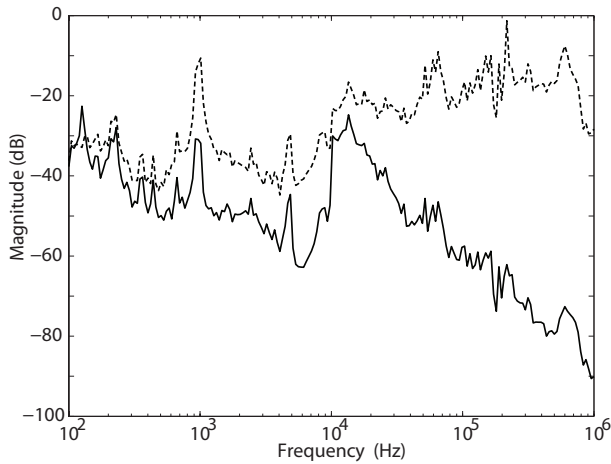


Figure 4.22: Worst-case magnitude of the transfer towards the topography estimation error determined at each frequency point for the closed-loop dual actuated system designed with $W_{es} = 1$ (dashed) and $W_{es} = 8$ (solid).

4.6 Conclusions

Dual-actuated control of the tip-sample force allows to increase the bandwidth of the feedback loop controlling the tip-sample force in AFM, without sacrificing effective positioning range. This chapter presents a model-based design approach for the feedback controller in dual actuated AFM. Special emphasis is given on preventing strong destructive interference between both actuators, preventing instability of the feedback loop due to actuator saturation and taking into account the influence of the feedback controller design on the accuracy of the topography estimate.

A feedback controller is designed for a prototype dual actuated AFM, aimed at achieving the highest possible control bandwidth, as may be relevant for imaging applications where minimal force variations between the tip and the sample are most important, e.g. when imaging fragile biological samples. In order to identify the dynamical behavior of the system for varying imaging conditions, the frequency responses of both actuators are measured with various measurement probes and sample discs. Based on the measured frequency responses, dynamical models for both actuators including an uncertainty description are derived and the maximum allowable actuation bandwidths are determined. Based on these models a model-based feedback controller is designed to control the tip-sample interaction force via the two actuators simultaneously.

An important design criterion for the controller of a dual actuated AFM is to prevent strong destructive interference between both actuators, in which both actuators are negating part of each others motion. In this research it is shown that due to this interference problem the choice of the transition frequency between both actuators is subject to a design trade-off between the effective positioning range at lower frequencies and the effective positioning range at higher frequencies. Given the expected frequency spectrum of the topography signal, the transition frequency between both actuators should be designed such that the probability of saturation of the short-range actuator is minimal. In order to prevent strong destructive interference between both actuators, the closed-loop bandwidth of the long-range actuator should not be made higher than strictly necessary for the tracking of the larger amplitude, low-frequency components of the topography signal, which are typically mainly stemming from the sample tilt.

In order to ensure stability of the closed-loop system in case of saturation of the short-range actuator an anti-windup controller is designed. It is shown that for this particular system a simple static anti-windup controller is sufficient to guarantee global stability of the system, and it has the advantage of not introducing any oscillations in the transient behavior of the system when recovering from saturation, which is generally a problem for higher order anti-windup control schemes. Experimental results verify that the system with the static anti-windup controller provides global stability and fast recovery from saturation, while the system without anti-windup controller shows large oscillations or even becomes unstable.

The designed controller is implemented on the prototype AFM system by utilizing an *FPGA*, achieving a closed-loop disturbance rejection of about 20 kHz, which is about 20 times higher than the optimally controlled single actuated system. AFM-

images are obtained with the newly designed dual-actuated AFM system in order to demonstrate the significant reduction in residual control error, as compared to the single actuated AFM that is controlled either by a PI-controller or a model-based controller. The reduced force variations between the tip and the sample results in a more gentle probing of the sample surface and allows for faster imaging, which is especially important when imaging fragile biological samples. Furthermore, it is shown that when addressing the accuracy of the topography estimate in the design of the feedback controller for dual actuated AFM, the transition frequency between both actuators provides additional design freedom to improve the accuracy of the topography estimate in the intermediate frequency region.

Conclusions and Recommendations

This research is focussed on improved mechatronics and control of current AFM systems, in order to improve the imaging performance in terms of speed and image quality, as formulated by the research question in Section 1.4. In the previous chapters these questions are subsequently addressed and in this chapter the findings are summarized and recommendations for future research are discussed.

5.1 Conclusions

While classical AFM imaging is often viewed as a rather static process, high speed AFM imaging is a highly dynamical process which requires accurate knowledge and control of the dynamical behavior of the AFM system. In order to improve the speed and accuracy of the imaging process, in this thesis the mechatronics of a commercially available AFM system have been adapted by modifying the driving electronics for the lateral scanning motion to allow combined sensing and actuation, and by adding an additional actuator for high bandwidth vertical positioning of the measurement tip. Furthermore, the control of the imaging process has been improved for the lateral scanning motion, the control of the tip-sample force, and the topography estimation.

One of the main limiting factors on the AFM imaging speed are the weakly damped resonance modes of the piezoelectric scanning stages used in AFM. Excitation of these weakly damped resonance modes result oscillations in the scanning path, which is a major source of image distortions. In order to compensate for these scanner oscillations during high speed AFM imaging, in Chapter 2 a method has been presented to add damping to the resonance modes in both scanning axes via active feedback control. By utilizing the piezoelectric elements of the scanning stage both as actuator and sensor simultaneously the use of expensive dedicated position sensors is omitted, resulting in an improvement on the imaging speed of existing AFM instruments with a factor of about 5 at low cost. To this end the scanning electrodes of the piezoelectric tube scanner have been connected in a capacitive bridge-circuit, which allows to sense the forces

acting on the piezoelectric actuators. An adaptive circuit balancing technique has been utilized in order to guarantee the integrity of the self-sensing signals by compensating for the effects of component mismatch and hysteresis within the piezo element, which is particularly important at larger scan range. The obtained measurement signals have been used for feedback control, which is demonstrated to add 18dB of damping to the first resonance modes in both axes of the piezoelectric scanning stage, and about 30dB to the corresponding cross-talk. Experimental results demonstrate a significantly reduction in scanner oscillations and the associated image distortions during high speed AFM imaging.

During AFM imaging the force between the tip and the sample is controlled in a feedback loop by measuring the cantilever deflection and manipulating the height between the tip and the sample. The compensating actions of the feedback loop are used to estimate the sample topography. The faster lateral scanning speed in high speed AFM, requires high bandwidth control of the tip-sample forces to prevent damaging the tip or the sample. The increased control bandwidths in high speed AFM result in stronger excitation of the higher order system dynamics which influences the measurement process. Therefore, in high speed AFM imaging the obtained measurement signals need to be de-convoluted with a model of the system dynamics in order to allow accurate reconstruction of the true sample topography. However, the dynamical behavior of the AFM system may show variations, for instance when changing the tip or the sample, which results in a certain degree of dynamical uncertainty. In Chapter 3 it is shown that the dynamical uncertainty of the AFM system poses strong limitations on the achievable accuracy of the topography estimation. Moreover, it is shown that the design of the feedback controller has a strong influence on the accuracy of the topography estimation as a result of the dynamical uncertainty of the system. In order to handle this coupling between the control objectives and the topography estimation, an integrated design method has been presented to design the feedback controller and topography estimator for a given AFM system, taking into account the dynamical uncertainty of the system associated with the varying load conditions. It has been shown that due to the dynamical uncertainty for a given AFM system a trade-off has to be made between the bandwidth of the vertical feedback loop on the one hand, and the accuracy of the topography estimation on the other hand. Therefore, in order to allow both a higher control bandwidth, as well as more accurate topography estimation the mechanical design of the system has to be optimized for more consistent dynamical behavior over an as large as possible bandwidth.

An attractive way to optimize the design of the z-actuators for consistent dynamics over a larger bandwidth is to decrease the overall size of these actuators resulting higher fundamental resonance frequencies. Short-range piezo-actuators [46], MEMS based actuators [94], or cantilevers with integrated actuation [93, 42] are a good examples of such actuators. However, by decreasing the size of the actuators they may be limited in positioning range. Therefore, to allow practical use of such short range, but high-bandwidth actuators, they may be combined with a long-range, low-bandwidth actuator to form a dual actuated

system. In Chapter 4 of this thesis dual actuated control of the tip-sample force has been investigated by extending a commercial AFM with a small piezoelectric actuator to allow fast positioning of the measurement probe in the z-axis. Systematic design of the feedback controller for dual actuated AFM has been investigated, aimed at achieving the maximum bandwidth for a given a dual actuated AFM, minimal destructive interference between both actuators, and guaranteeing stability of the system in case saturation of the short-range actuator occurs. To guarantee the stability of the control loop in case of saturation of the short-range actuator, an anti-windup controller is designed. It has been shown that the choice of the transition frequency at which the short-range actuator takes over from the long-range actuator is subject to a trade-off between the positioning range at lower frequency and the positioning range at higher frequency. Moreover, it has been shown that the use of multiple actuators allows more design freedom when considering the accuracy of the topography estimation in the design of the feedback controller. As compared to single actuated AFM, the designed prototype dual actuated AFM has shown significantly less force variation between the tip and the sample during imaging experiments, and consequently allows significantly faster AFM imaging.

In this thesis the dynamical uncertainty of the AFM instruments has been identified as one of the main limiting factors on the imaging performance, both in terms of speed and in terms of accuracy. While from a theoretical point of view controlling the system above its first resonance frequency is possible, in practise the control bandwidth often needs to be cutoff much earlier because the dynamical behavior of the system becomes largely unpredictable above the first mechanical resonances of the scanning stage, as also shown in this thesis. Moreover, the accuracy of the instruments is shown to be directly dependent on the predictability of the dynamical behavior. Hence, improving the mechanical design of the AFM instruments for more consistent dynamical behavior over a larger bandwidth may be an important design criterion for future AFM designs. Model-based controller design methods have shown to be very valuable to allow addressing the various controller objectives and to push the imaging performance towards its maximum, given a good dynamical model of the existing AFM system. While the controller synthesis itself is a well defined optimization problem, obtaining a dynamical model of the physical AFM system and translating the systems objectives into a cost-function for the optimization requires some judicious engineering choices. Hence, the model-based controller design techniques are important tools for the controller design in AFM but still require input from an experienced control engineer. However, AFM operators may not always have such expertise to design or readjust such high-end controllers. The robustness of these controllers is therefore an important aspect to allow these controllers to be designed only once by an control expert, after which they can be used for various imaging experiments by AFM operators which do not necessarily have this expertise. In order to achieve this robustness combined with high imaging performance, again the consistency of the dynamical behavior of the AFM system is a key aspect.

5.2 Recommendations

As a continuation of the research on improved mechatronics and control of AFM presented in this thesis, the following topics may be considered for future research:

- In order to allow high imaging speeds, dedicated high speed AFM scanners utilize lightweight and stiff mechanical designs in order to push the mechanical resonances to higher frequencies. Although, the mechanical design may be further improved to push the resonances frequencies even higher, at some point the bandwidth is mainly limited by the resonance frequencies of the piezoelectric actuators themselves. These piezoelectric actuators require a certain size in order to achieve sufficient positioning range and actuation force, and therefore may not allow to be scaled down much further. However, from a control engineering point of view, the resonances frequencies of the system may not be a direct limitation on the control bandwidth, as long as the dynamical behavior around these resonances remains predictable and controllable. Hence, instead of optimizing the mechanical design of the scanning stages for higher resonance frequencies, the mechanical design may be rather optimized for reduced dynamical uncertainty. As shown in this work, reducing the dynamical uncertainty may improve both the imaging speed, as well as the accuracy of the AFM instrument. The dynamical uncertainty of the system may be reduced for instance via an indexing system which fixes the alignment of the sample disc and the measurement tip, by standardizing the weight of the sample discs, and by damping the weakly damped resonances of the system, for instance via the self-sensing actuation method presented in Chapter 2.
- Dual actuated control of the tip-sample force in AFM allows high bandwidth control without sacrificing the effective positioning range, as also shown in this work. Because the typical triangular reference signals used for the lateral scanning motion have a frequency spectrum which decays with increasing frequency, a combination of a long-range, low-bandwidth actuator, and a high-bandwidth, short-range actuator may also be used to provide the fast lateral scanning motion, enabling both high-speed and long-range imaging.
- Iterative Learning Control (ILC) methods have shown to be very effective in compensating for the non-linear hysteresis in the scanning path, exploiting the fact that the scanning motion is a repetitive motion [56, 107, 96]. However, because ILC requires an accurate inverse model of the linear system dynamics, the control bandwidth of ILC is often limited by the dynamical uncertainties associated with slight variations of the weakly damped scanner resonances. However, by damping the scanner resonances via the self-sensing actuation method presented in this research, the dynamical uncertainty associated with a slight changes of the scanner resonances may also be significantly reduced. Therefore, a combination of ILC and active damping via self-sensing actuation may be investigated, allowing a higher con-

trol bandwidth for the ILC controller and consequently further improve the scanning accuracy and speed.

- While in this research mainly contact mode imaging is assumed, in some imaging applications dynamic mode imaging is preferred, mostly because of the reduced lateral friction forces between the tip and the sample. Most classical dynamic imaging modes rely on a steady state relation between the cantilever oscillation and the average tip-sample distance, and therefore the bandwidth of these dynamic imaging modes is limited. Moreover, because with dynamic mode imaging the tip travels through a larger part of the non-linear tip-sample force interaction regime, the reconstruction of the sample topography from the cantilever deflection signal is more involved as compared to contact mode imaging. In order to extend the results of this work to high speed dynamic mode imaging, these results may be combined with the recently developed observer-based dynamic mode imaging methods [73,42]. These observer-based dynamic imaging methods utilize a model of the cantilever dynamics to allow fast derivation of the average tip sample height within the transient behavior of the cantilever response, and therefore allow a significantly faster imaging bandwidth as compare to classical dynamic imaging modes. These methods may be extended with accurate calibration methods to also allow high bandwidth and accurate reconstruction of the sample topography, and potentially reconstruction of the tip-sample interaction force curves in dynamic mode imaging.
- In most AFM systems the sample topography is estimated based on the output of the feedback controller. As shown in this research, the accuracy of such approach is limited by the dynamical uncertainty of the actuator. Although a higher imaging accuracy may be obtained using dedicated position sensors which directly measure the displacement of the z-actuator, the precision of these position sensors is most often not sufficient to meet the required imaging resolution for high bandwidth applications. However, a combination of these two approaches may be investigated, using the measurement signal of the position sensor to allow online identification of the actuator dynamics, which may reduce the dynamical uncertainty and therefore improve the topography estimation accuracy. As in this case the sensor signal is not used to directly estimate the sample topography, the precision of the topography estimation is not affected by the sensor noise, which may enable the use of cheaper position sensors.
- While in this research only feedback control is considered for the control of the tip-sample force in dual actuated AFM, also feedforward control methods could be considered, making use of the fact that the low-frequency sample topography variations are largely repetitive over several scan-lines [84]. In dual actuated AFM, the application of feedforward control might be particularly valuable as the possibility of compensating for the topography variations in a non-causal manner might be used to minimize the chances of saturation for the short-range actuator, and consequently further reduce the chance of damage of the tip and sample.

Identification and compensation of hysteresis within the topography estimation

The piezoelectric actuators used to control the tip-sample force in AFM are generally known to exhibit a certain degree of hysteretic behavior, which may degrade the accuracy of the topography estimation. In this appendix it is discussed how the hysteresis may be compensated for in the topography estimation via a charge measurement. Moreover, the hysteresis within the z-axis of the piezoelectric tube scanner used in Chapter 3 is identified, and the compensation of hysteresis within the topography estimation via a charge measurement is experimentally validated.

A.1 Introduction

Most AFM systems utilize piezoelectric actuators which typically suffer from a certain degree of non-linearity due to hysteresis [33]. The hysteresis within a piezoelectric actuator is stemming from micro friction within the piezo crystals, causing a non-linear, memory type of behavior [33]. This non-linearity is predominantly observed in the relation between the voltage $u(t)$ applied over the piezo and the actuator displacement $x(t)$, while the relation between the charge $q(t)$ within the piezo element and the actuator displacement $x(t)$ is linear [1]. Depending on the quality of the piezo material this hysteresis may result in gain variations of about 1% up about 15%.

The integrated design methodology for the feedback controller and topography estimator in AFM as proposed in Section 3.3 assumes the actuator dynamics to be predominantly linear. This is valid for the AFM system with (high quality) piezoelectric actuators in the z-axis with low hysteresis. For AFM system with a more

severe hysteretic behavior in the z-actuator, in this appendix it is discussed how the methodology of Section 3.3 can be extended to explicitly address the actuator hysteresis within the topography estimation. Moreover, the hysteresis within the z-axis of the piezoelectric tube scanner used in Chapter 3 ('J-scanner', Bruker Nano Inc., Santa Barbara, USA) is identified, and the compensation of hysteresis in the topography estimate via charge measurement is experimentally verified.

A.1.1 Compensating for hysteresis in topography estimation

The dynamical behavior of the piezoelectric actuators can be linearized to a large extent by inverting the non-linear hysteretic behavior via a Preisach hysteresis model [17, 92]. However, in order to guarantee the accuracy of such a hysteresis model this may require frequent calibration. The hysteresis may also be compensated by utilizing a charge controlled amplifier [1, 28], making use of the fact that the hysteresis is not present in the relation between the charge and the displacement of the piezoelectric actuator [33]. However, applying charge control requires thorough redesign of the driving amplifier, and may suffer from stability issues particularly at low frequencies.

Instead of linearizing the piezo actuators, the degrading effects of hysteresis on the accuracy of the topography estimate may also be compensated by observing the hysteresis via a charge measurement, and taking this measurement into account in the topography estimator. As shown in Figure A.1 the actuator dynamics can be split in a (non-linear) part from input voltage $u(t)$ towards the charge $q(t)$ denoted G_{uq} , and a linear part from charge $q(t)$ towards the actuator displacement $x(t)$ denoted G_{qx} :

$$x(t) = G_{qx}(p) \cdot q(t) \tag{A.1}$$

Hence, the non-linear hysteresis may be compensated in the topography estimation by using the measured charge $\bar{q}(t)$ as an input to the topography estimator, i.e. the estimated topography of Equation (3.7) now becomes:

$$\hat{h}(t) = F_2(p) \cdot \underbrace{\left[\hat{B}^{-1}(p) \quad -\hat{G}_{qx}(p) \right]}_{\hat{F}_1} \cdot \begin{bmatrix} d(t) \\ \bar{q}(t) \end{bmatrix}, \tag{A.2}$$

with \hat{G}_{qx} a linear model of the actuator dynamics from charge $q(t)$ to actuator displacement $x(t)$. The blockdiagram of the feedback loop controlling the tip-sample force with the additional measurement of the charge is shown by Figure A.1. The charge within the piezoelectric actuator can be measured by connecting a reference capacitor in series with the piezoelectric element. Due to the series connection the charge within the piezo electric actuator is the same as in the reference capacitor which can be obtained by measuring the voltage over this capacitor ($q(t) = C_s \cdot u_s(t)$). Notice that such charge measurement allows to compensate only for the degrading effects of hysteresis within the topography estimation, while the effects of hysteresis in the positioning get compensated by the overall feedback control loop. However, the gain variations stemming from the hysteresis are in general too small to cause considerable loss of performance or stability

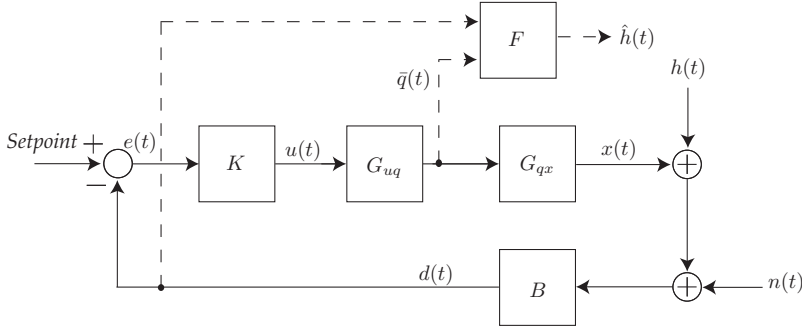


Figure A.1: Block diagram of the feedback loop controlling the tip sample force in AFM with an additional charge measurement as input for the topography estimator. The actuator dynamics from input $u(t)$ towards the charge $q(t)$ are given by G_{uq} , actuator dynamics from charge $q(t)$ towards the actuator displacement $x(t)$ are given by G_{qx} , the sensor dynamics are denoted B , and feedback controller is denoted K . The topography estimator F provides an estimate of the topography signal $\hat{h}(t)$ based on sensor signal $d(t)$, and the measured charge $\bar{q}(t)$.

issues, and are taken care off by the robustness of the feedback controller. Especially for AFM systems utilizing piezoelectric stack actuators, that typically have a large amount of hysteresis of up to about 15%, compensating for the hysteresis via a charge measurement may significantly improve the accuracy of the topography estimate. The piezoelectric actuators used within commercially available AFMs are most often of better quality, showing much lower hysteresis, and additional compensation of the hysteresis for the topography estimate may be not be required. Experimental validation of this method is discussed in Section A.2.

The integrated design methodology presented Section 3.3 can be extended to the case where the measured charge is used as an additional input for the topography estimator by using a separate (linearized) model of the dynamics from feedback output $u(t)$ towards charge $q(t)$ that contains the amplifier dynamics (G_{uq} in Fig. A.1) and basing the remainder of the identification experiments discussed in Section 3.3.1 on the charge $q(t)$ instead of $u(t)$ (i.e. identifying G_{uq} in Fig. A.1).

A.2 Experimental results

In order to identify the amount of hysteresis within the piezoelectric actuator used in Chapter 3 and to verify the hysteresis compensation method discussed in Section A.1.1, the relation between the voltage and the actuator displacement as well as the charge versus actuator displacement are measured. Therefore, the z-axis of this piezoelectric actuator is connected within a charge measurement circuit as shown by Figure A.2. The capacitance of the piezo element C_p is 47 nF, while the capacitance C_s is 1 μ F. This capacitor ratio is chosen such that the voltage on the input of the instrumentation amplifier will not exceed ± 10 V while driving

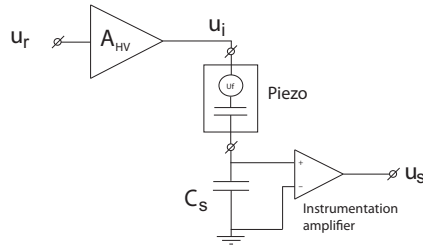


Figure A.2: Circuit to allow the measurement of the charge within the piezoelectric element for the hysteresis compensation in the topography estimate. The charge within the piezo element is directly proportional to the voltage measured over the reference capacitor: $q(t) = C_s \cdot u_s(t)$.

the piezoelectric actuator over its maximum range ± 200 V. Moreover, the large capacitor ratio ensures that the reference capacitor C_s is experiencing only low voltages which are within its linear regime. The system is driven by a high voltage amplifier denoted A_{HV} in Figure A.2 (PZD700, Trek, Medina, USA). While driving the system, the displacement of the piezoelectric actuator is measured using a capacitive position sensor (6810 gaging module with a 6504-01 probe, ADE Technologies, Westwood, USA).

Figure A.3 shows the results when driving the system with a sinusoidal input signal of 50 Hz with an amplitude of ± 200 V, resulting in a total displacement of the piezoelectric actuator of about $4.5 \mu\text{m}$. Figure A.3a depicts the input voltage versus the actuator displacement, showing that the forward motion does not exactly overlap the backward motion due to the hysteresis. The maximum width and height of the hysteresis curve is about $0.05 \mu\text{m}$ at about 5 V. Hence, the gain variations due to the hysteresis are less than 1.5% at full displacement range. Figure A.3b depicts the measured charge versus the actuator displacement, revealing no hysteresis in the relation between the charge within the piezo actuator and its displacement. Hence, these results indicate that although the hysteresis within this particular piezoelectric actuator is relatively low, using the charge measurement as an input to the topography estimator instead of the input voltage would provide more accurate estimation of the actuator displacement, and thus better accuracy of the topography estimation.

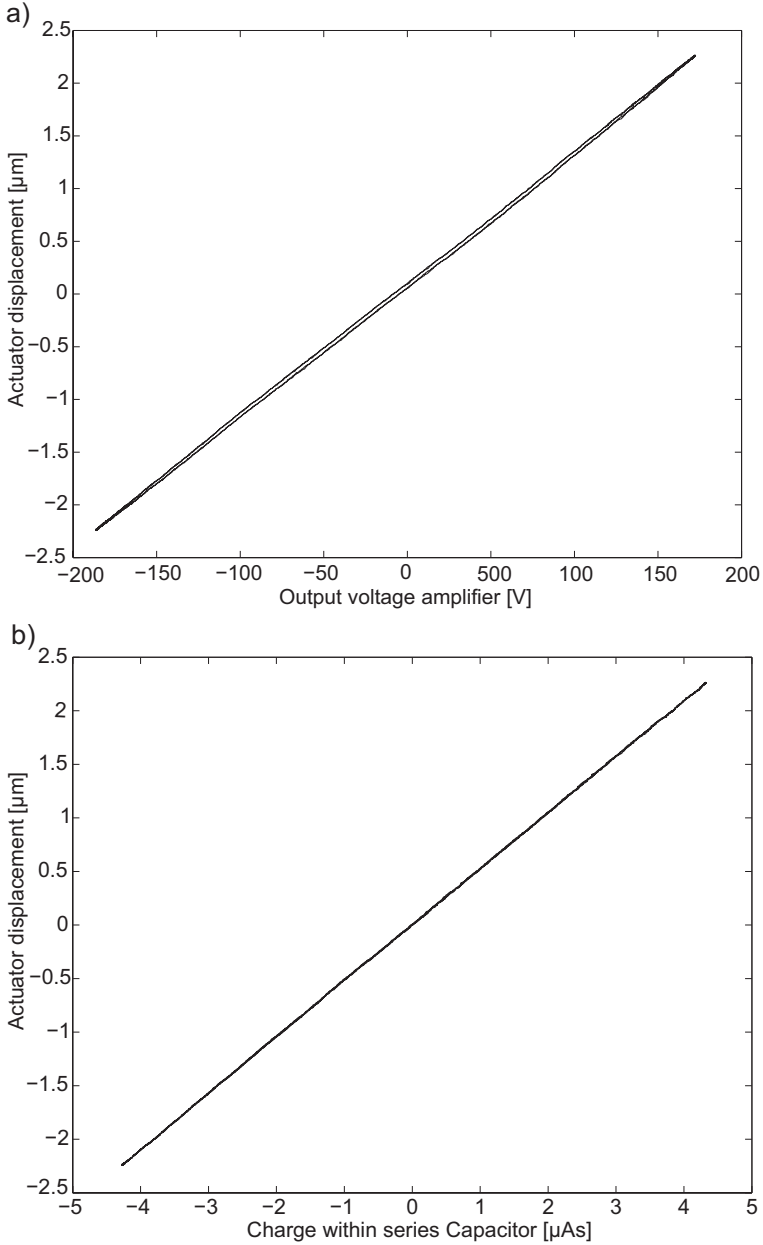


Figure A.3: Identification of the hysteresis within the z-axis of the piezoelectric tube scanner ('J-scanner', Bruker Nano Inc., Santa Barbara, USA), showing the input voltage versus actuator displacement (a), and charge versus actuator displacement (b), in response to a 50 Hz $400 V_{pp}$ sinusoidal input signal.

Bibliography

- [1] H. Adriaens, W.L. De Koning, and R. Banning. Modeling piezoelectric actuators. *IEEE/ASME Transactions on Mechatronics*, 5(4):331–341, 2000.
- [2] T.R. Albrecht, P. Grutter, D. Horne, and D. Rugar. Frequency modulation detection using high-q cantilevers for enhanced force microscope sensitivity. *Journal of Applied Physics*, 69(2):668–673, 1991.
- [3] S. Alexander, L. Hellemans, O. Marti, J. Schneir, V. Elings, PK Hansma, M. Longmire, and J. Gurley. An atomic-resolution atomic-force microscope implemented using an optical lever. *Journal of Applied Physics*, 65:164–167, 1989.
- [4] T. Ando, N. Kodera, Y. Naito, T. Kinoshita, K. Furuta, and Y.Y. Toyoshima. A high-speed atomic force microscope for studying biological macromolecules in action. *Chemphyschem*, 4(11):1196–1202, 2003.
- [5] T. Ando, N. Kodera, E. Takai, D. Maruyama, K. Saito, and A. Toda. A high-speed atomic force microscope for studying biological macromolecules. *Proceedings of the National Academy of Sciences*, 98(22):12468–12472, 2001.
- [6] B. Bhikkaji, M. Ratnam, A.J. Fleming, and S.O.R. Moheimani. High performance control of piezoelectric tube scanners. *IEEE Transactions of Control Systems Technology*, 15:853–866, 2007.
- [7] B. Bhushan and O. Marti. Scanning probe microscopy—principle of operation, instrumentation, and probes. *Springer Handbook of Nanotechnology*, pages 573–617, 2010.
- [8] G. Binnig, C.F. Quate, and C. Gerber. Atomic force microscope. *Physical Review Letters*, 56(9):930–933, 1986.
- [9] G. Binnig, H. Rohrer, C. Gerber, and E. Weibel. Surface studies by scanning tunneling microscopy. *Physical Review Letters*, 49(1):57–61, 1982.
- [10] G. Binnig and D.P.E. Smith. Single-tube three-dimensional scanner for scanning tunneling microscopy. *Review of Scientific Instruments*, 57:1688–1698, 1986.

- [11] R.S. Blom and P.M.J. Van den Hof. Multivariable frequency domain identification using iv-based linear regression. In *49th IEEE Conference on Decision and Control, Atlanta, USA*, pages 1148–1153. IEEE, 2010.
- [12] G. Borionetti, A. Bazzali, and R. Orizio. Atomic force microscopy: a powerful tool for surface defect and morphology inspection in semiconductor industry. *The European Physical Journal Applied Physics*, 27(1-3):101–106, 2004.
- [13] D.A. Bristow, M. Tharayil, and A.G. Alleyne. A survey of iterative learning control. *Control Systems Magazine, IEEE*, 26(3):96–114, 2006.
- [14] J.A. Butterworth, L.Y. Pao, and D.Y. Abramovitch. A comparison of control architectures for atomic force microscopes. *Asian Journal of Control*, 11(2):175–181, 2009.
- [15] D.G. Cole and R.L. Clark. Adaptive compensation of piezoelectric sensor-actuators. *Journal of Intelligent Material Systems and Structures*, 5:665–672, 1994.
- [16] D. Croft and S. Devasia. Vibration compensation for high speed scanning tunneling microscopy. *Review of Scientific Instruments*, 70:4600–4605, 1999.
- [17] D. Croft, G. Shed, and S. Devasia. Creep, hysteresis, and vibration compensation for piezoactuators: Atomic force microscopy applications. *AMSE Journal of Dynamic Systems, Measurement, and Control*, 123:35–43, 2001.
- [18] R.A. de Callafon, R. Nagamune, and R. Horowitz. Robust dynamic modeling and control of dual-stage actuators. *IEEE Transactions on Magnetics*, 42:247–254, 2006.
- [19] S. Devasia, E. Eleftheriou, and S.O.R. Moheimani. A survey of control issues in nanopositioning. *IEEE Transactions on Control Systems Technology*, 15:802–823, 2007.
- [20] J.J. Dosch, D.J. Inman, and E. Garcia. A self-sensing piezoelectric actuator for collocated control. *Journal of Intelligent Material Systems and Structures*, 3:166–185, 1992.
- [21] S.G. Douma and P.M.J. Van den Hof. Relations between uncertainty structures in identification for robust control. *Automatica*, 41(3):439–457, 2005.
- [22] Y.F. Dufrêne. Direct characterization of the physicochemical properties of fungal spores using functionalized afm probes. *Biophysical Journal*, 78(6):3286–3291, 2000.
- [23] Y.F. Dufrêne. Atomic force microscopy, a powerful tool in microbiology. *Journal of bacteriology*, 184(19):5205, 2002.
- [24] P. Easton and P. West. *Atomic Force Microscopy*. Oxford university press, 2010.
- [25] C. Edwards and I. Postlethwaite. An anti-windup scheme with closed-loop stability considerations. *Automatica*, 35(4):761–765, 1999.

- [26] G.E. Fantner, D.J. Burns, A.M. Belcher, I.W. Rangelow, and K. Youcef-Toumi. DMCMN: In Depth Characterization and Control of AFM Cantilevers With Integrated Sensing and Actuation. *Journal of Dynamic Systems, Measurement, and Control*, 131:061104(1–13), 2009.
- [27] A.J. Fleming. Time-domain adaptive feed-forward control of nanopositioning systems with periodic inputs. In *Proceedings of the 2009 American Control Conference, St Louis, USA*, pages 1676–1681. IEEE, 2009.
- [28] A.J. Fleming. Quantitative SPM topographies by charge linearization of the vertical actuator. *Review of Scientific Instruments*, 81(10):103701(1–5), October 2010.
- [29] AJ Fleming, BJ Kenton, and KK Leang. Bridging the gap between conventional and video-speed scanning probe microscopes. *Ultramicroscopy*, 110:1205–1214, 2010.
- [30] A.J. Fleming and K.K Leang. Charge drives for scanning probe microscope positioning stages. *Ultramicroscopy*, 108(12):1551–1557, November 2008.
- [31] A.J. Fleming and S.O.R. Moheimani. Sensorless vibration suppression and scan compensation for piezoelectric tube nanopositioners. *IEEE Transactions on Control Systems Technology*, 14:33–44, 2006.
- [32] F.J. Giessibl. Advances in atomic force microscopy. *Reviews of Modern Physics*, 75(3):949, 2003.
- [33] M. Goldfarb and N. Celanovic. Modeling piezoelectric stack actuators for control of micromanipulation. *IEEE Control Systems Magazine*, 17(3):69–79, 1997.
- [34] G. Guo, D. Wu, and T.C. Chong. Modified dual-stage controller for dealing with secondary-stage actuator saturation. *IEEE Transactions on Magnetics*, 39(6):3587–3592, 2003.
- [35] H.G. Hansma. Surface biology of dna by atomic force microscopy. *Annual Review of Physical Chemistry*, 52(1):71–92, 2001.
- [36] P.K. Hansma, G. Schitter, G.E. Fantner, and C. Prater. High speed atomic force microscopy. *Science*, 314:601–602, 2006.
- [37] U. Hartmann. Magnetic force microscopy. *Annual Review of Materials Science*, 29(1):53–87, 1999.
- [38] D. Hernandez, S.S. Park, R. Horowitz, and A.K. Packard. Dual-stage track-following servo design for hard disk drives. In *Proceedings of the 1999 American Control Conference, San Diego, USA*, volume 6, pages 4116–4121. IEEE, 1999.
- [39] G. Herrmann, MC Turner, I. Postlethwaite, and G. Guo. Practical implementation of a novel anti-windup scheme in a HDD-dual-stage servo-system. *IEEE/ASME Transactions on Mechatronics*, 9(3):580–592, 2004.

- [40] R. Horowitz, Y. Li, K. Oldham, S. Kon, and X. Huang. Dual-stage servo systems and vibration compensation in computer hard disk drives. *Control Engineering Practice*, 15(3):291–305, 2007.
- [41] A.D.L. Humphris, J.K. Hobbs, and M.J. Miles. Ultrahigh-speed scanning near-field optical microscopy capable of over 100 frames per second. *Applied Physics Letters*, 83:6, 2003.
- [42] Y. Jeong, G.R. Jayanth, S.M. Jhiang, and C.H. Menq. Direct tip-sample interaction force control for the dynamic mode atomic force microscopy. *Applied Physics Letters*, 88:204102, 2006.
- [43] Y. Jeong, G.R. Jayanth, and C.H. Menq. Control of tip-to-sample distance in atomic force microscopy: A dual-actuator tip-motion control scheme. *Review of Scientific Instruments*, 78:093706(1–7), 2007.
- [44] A. Karbach and D. Drechsler. Atomic force microscopy: a powerful tool for industrial applications. *Surface and interface analysis*, 27(5-6):401–409, 1999.
- [45] C.E. Kinney, R.A. de Callafon, and M. de Oliveira. Spectral over-bounding of frequency data for modeling product variability in hard disk drive actuators. In *Proceedings of the European Control Conference 2007, Kos, Greece*, pages 2902–2907, 2007.
- [46] D. Knebel, M. Amrein, K. Voigt, and R. Reichelt. A fast and versatile scan unit for scanning force microscopy. *Scanning*, 19(4):264–268, 1997.
- [47] N. Kodera, M. Sakashita, and T. Ando. Dynamic proportional-integral-differential controller for high-speed atomic force microscopy. *Review of Scientific Instruments*, 77:083704, 2006.
- [48] S. Kuiper, A.J. Fleming, and G. Schitter. Dual actuation for high speed atomic force microscopy. In *Proceedings of the 5th IFAC Symposium on Mechatronics Systems, Cambridge, USA*, pages 220–226, 2010.
- [49] S. Kuiper and G. Schitter. Mimo self-sensing actuation of a piezoelectric tube scanner. In *Proceedings of the ASME 2009 Dynamic Systems and Control Conference, Hollywood, CA, USA*, pages 811–817, 2009.
- [50] S. Kuiper and G. Schitter. Self-sensing actuation and damping of a piezoelectric tube scanner for atomic force microscopy. In *Proceedings of the European Control Conference, Budapest, Hungary, 2009*, pages 3887–3890, 2009.
- [51] S. Kuiper and G. Schitter. Active damping of a piezoelectric tube scanner using self-sensing piezo actuation. *Mechatronics*, 20:656–665, 2010.
- [52] S. Kuiper and G. Schitter. Improving the imaging speed of afm with modern control techniques. *Control Technologies for Emerging Micro and Nanoscale Systems*, 1:83–100, 2011.
- [53] S. Kuiper and G. Schitter. Model-based feedback controller design for dual actuated atomic force microscopy. *Mechatronics*, (in press), 2011.

- [54] S. Kuiper, P.M.J. Van den Hof, and G. Schitter. Towards integrated design of a robust feedback controller and topography estimator for atomic force microscopy. In *Proceedings of the 18th IFAC World Congress, Milan, Italy*, pages 12709–12714, 2011.
- [55] S. Kuiper, P.M.J. Van den Hof, and G. Schitter. Trade-off between the control bandwidth and the measurement accuracy in atomic force microscopy. In *To appear in the Proceedings of the 2012 IEEE International Instrumentation and Measurement Technology Conference, 13-16 May 2012, Graz, Austria.*, 2012.
- [56] K.K. Leang and S. Devasia. Design of hysteresis-compensating iterative learning control for piezo-positioners: Applications to atomic force microscope. *Mechantronics*, 16:141–158, 2006.
- [57] C. Lee and S.M. Salapaka. Fast imaging with alternative signal for dynamic atomic force microscopy. *Applied Physics Letters*, 97:133101, 2010.
- [58] Y. Li and J. Bechhoefer. Feedforward control of a piezoelectric flexure stage for afm. In *Proceedings of the 2008 American Control Conference, Seattle, USA*, pages 2703–2709. IEEE, 2008.
- [59] Y. Li, B.W. Maynor, and J. Liu. Electrochemical afm dip-pen nanolithography. *Journal of the American Chemical Society*, 123(9):2105–2106, 2001.
- [60] J. Loos. The art of spm: Scanning probe microscopy in materials science. *Advanced Materials*, 17(15):1821–1833, 2005.
- [61] F. Marinello, S. Carmignato, A. Voltan, E. Savio, and L. De Chiffre. Error sources in atomic force microscopy for dimensional measurements: Taxonomy and modeling. *Journal of Manufacturing Science and Engineering*, 132:030903, 2010.
- [62] A.H. Meitzler. Ieee standard on piezoelectricity. *Society*, 1988.
- [63] R. Merry, M. Uyanik, R. van de Molengraft, R. Koops, M. van Veghel, and M. Steinbuch. Identification, control and hysteresis compensation of a 3 DOF metrological AFM. *Asian Journal of Control*, 11:130–143, 2009.
- [64] S.O.R. Moheimani and Y.K. Yong. Simultaneous sensing and actuation with a piezoelectric tube scanner. *Review of Scientific Instruments*, 79:073702, 2008.
- [65] K. Mori, T. Munemoto, H. Otsuki, Y. Yamaguchi, and K. Akagi. A dual-stage magnetic disk drive actuator using a piezoelectric device for a high track density. *IEEE Transactions on Magnetics*, 27(6 Part 2):5298–5300, 1991.
- [66] D.J. Müller, H. Janovjak, T. Lehto, L. Kuerschner, and K. Anderson. Observing structure, function and assembly of single proteins by afm. *Progress in biophysics and molecular biology*, 79(1-3):1–43, 2002.
- [67] M. Nonnenmacher, M.P. Oboyle, and H.K. Wickramasinghe. Kelvin probe force microscopy. *Applied Physics Letters*, 58(25):2921–2923, 1991.

- [68] L.M. Picco, L. Bozec, A. Ulcinas, D.J. Engledew, M. Antognozzi, M.A. Horton, and M.J. Miles. Breaking the speed limit with atomic force microscopy. *Nanotechnology*, 18:044030, 2007.
- [69] R. Pintelon and J. Schoukens. *System identification: a frequency domain approach*. Wiley-IEEE Press, 2001.
- [70] A. Radke and Z. Gao. A survey of state and disturbance observers for practitioners. In *Proceedings of the 2006 American Control Conference, Minneapolis, USA*, pages 5183–5188. IEEE, 2006.
- [71] O.M.E Rifai and K. Youcef-Toumi. Coupling in piezoelectric tube scanners used in scanning probe microscope. In *Proceedings of the 2001 American Control Conference, Arlington, USA*, pages 3251–3255, 2001.
- [72] F.J. Rubio-Sierra, W.M. Heckl, and R.W. Stark. Nanomanipulation by atomic force microscopy. *Advanced Engineering Materials*, 7(4):193–196, 2005.
- [73] D.R. Sahoo, A. Sebastian, and M.V. Salapaka. Transient-signal-based sample-detection in atomic force microscopy. *Applied Physics Letters*, 83:5521, 2003.
- [74] S. Salapaka, A. Sebastian, JP Cleveland, and M.V. Salapaka. High bandwidth nano-positioner: A robust control approach. *Review of Scientific Instruments*, 73:3232–3241, 2002.
- [75] S.M. Salapaka, T. De, and A. Sebastian. A robust control based solution to the sample-profile estimation problem in fast atomic force microscopy. *International Journal of Robust and Nonlinear Control*, 15(16):821–838, 2005.
- [76] D. Sarid. *Scannig Force Microscopy*. New York: Oxford Univ. Press, 1994.
- [77] R.E. Scheid and D.S. Bayard. A globally optimal minimax solution for spectral overbounding and factorization. *IEEE Transactions on Automatic Control*, 40(4):712–716, 1995.
- [78] G. Schitter. Improving the speed of AFM by mechatronic design and modern control methods. *Technisches Messen*, 76(5):266–273, 2009.
- [79] G. Schitter, Karl Aström, B.E. DeMartini, P.J. Thurner, K.L. Turner, and P.K. Hansma. Design and modeling of a high-speed afm-scanner. *IEEE Transactions on Control Systems Technology*, 15:906–915, 2007.
- [80] G. Schitter, P. Menold, HF Knapp, F. Allgöwer, and A. Stemmer. High performance feedback for fast scanning atomic force microscopes. *Review of Scientific Instruments*, 72:3320, 2001.
- [81] G. Schitter, W.F. Rijkee, and N. Phan. Dual actuation for high-bandwidth nanopositioning. In *Proceedings of the 47th IEEE Conference on Decision and Control, Cancun, Mexico*, pages 5176–5181, 2008.
- [82] G. Schitter and A. Stemmer. Eliminating mechanical perturbations in scanning probe microscopy. *Nanotechnology*, 13:663, 2002.

- [83] G. Schitter and A. Stemmer. Identification and open-loop tracking control of a piezoelectric tube scanner for high-speed scanning-probe microscopy. *IEEE Transactions on Control Systems Technology*, 12:449–454, 2004.
- [84] G. Schitter, A. Stemmer, and F. Allgöwer. Robust two-degree-of-freedom control of an atomic force microscope. *Asian Journal of Control*, 6(2):156–163, 2004.
- [85] G. Schitter, P.J. Thurner, and P.K. Hansma. Design and input-shaping control of a novel scanner for high-speed atomic force microscopy. *Mechatronics*, 18(5-6):282–288, 2008.
- [86] E. Schrijver and J. Van Dijk. Disturbance observers for rigid mechanical systems: equivalence, stability, and design. *Journal of Dynamic Systems, Measurement, and Control*, 124:539–548, 2002.
- [87] S.J. Schroeck and W.C. Messner. On controller design for linear time-invariant dual-input single-output systems. In *Proceedings of the 1999 American Control Conference, San Diego, USA*, volume 6, pages 4122–4126, 1999.
- [88] A. Sebastian, A. Pantazi, S.O.R. Moheimani, H. Pozidis, and E. Eleftheriou. Achieving subnanometer precision in a mems-based storage device during self-servo write process. *IEEE Transactions on Nanotechnology*, 7(5):586–595, 2008.
- [89] A. Sebastian and S.M. Salapaka. Design methodologies for robust nanopositioning. *IEEE Transactions on Control Systems Technology*, 13(6):868–876, 2005.
- [90] S. Skogestad and I. Postlethwaite. *Multivariable feedback control: analysis and design*. John Wiley & Sons, 2005.
- [91] A.H. Slocum. *Precision machine design*. Society of Manufacturing, 1992.
- [92] H. Song. *Model-based Control in Adaptive Optical Systems*. PhD thesis, Delft University of Technology, 2011.
- [93] T. Sulchek, S.C. Minne, J.D. Adams, D.A. Fletcher, A. Atalar, C.F. Quate, and D.M. Adderton. Dual integrated actuators for extended range high speed atomic force microscopy. *Applied Physics Letters*, 75:1637–1639, 1999.
- [94] F.C. Tabak, E.C.M. Disseldorp, G.H. Wortel, A.J. Katan, M.B.S. Hesselberth, T.H. Oosterkamp, J.W.M. Frenken, and W.M. van Spengen. MEMS-based fast scanning probe microscopes. *Ultramicroscopy*, 110(6):599–604, 2010.
- [95] N. Tamer and M. Dahleh. Feedback control of piezoelectric tube scanners. In *Proceedings of the 33th Conference on Decision and Control, Lake Buena Vista, FL, USA*, volume 2, 1994.
- [96] J. ter Braake. Iterative learning control for high-speed atomic force microscopy. Master’s thesis, Delft University of Technology, 2009.

- [97] S. Tien, Q. Zou, and S. Devasia. Iterative control of dynamics-coupling-caused errors in piezoscanners during high-speed afm operation. *IEEE Transactions on Control Systems Technology*, 13(6):921–931, 2005.
- [98] D. Trumper, R. Hocken, D. Amin-Shahidi, D. Ljubcic, and J. Overcash. High-accuracy atomic force microscope. In Evangelos Eleftheriou and S. Moheimani, editors, *Control Technologies for Emerging Micro and Nanoscale Systems*, volume 413 of *Lecture Notes in Control and Information Sciences*, pages 17–46. Springer Berlin / Heidelberg, 2011.
- [99] A.A. Tseng. A comparison study of scratch and wear properties using atomic force microscopy. *Applied Surface Science*, 256(13):4246–4252, 2010.
- [100] A.A. Tseng, A. Notargiacomo, and TP Chen. Nanofabrication by scanning probe microscope lithography: A review. *Journal of Vacuum Science & Technology B: Microelectronics and Nanometer Structures*, 23:877, 2005.
- [101] J.R. van Hulzen, G. Schitter, PMJ Van den Hof, and J. van Eijk. Dynamics, load balancing, and modal control of piezoelectric tube actuators. *Mechatronics (in press)*, 2011.
- [102] S.V. Vaseghi. *Advanced digital signal processing and noise reduction*. Wiley, 2009.
- [103] J.S. Vipperman and R.L. Clark. Implementation of an adaptive piezoelectric sensoriactuator. *Asian Journal of Control*, 34:2102–2109, 1996.
- [104] T.V. Vorburger, J.A. Dagata, G. Wilkening, K. Lizuka, E.G. Thwaite, and P. Lonardo. Industrial uses of stm and afm. *CIRP Annals-Manufacturing Technology*, 46(2):597–620, 1997.
- [105] K.S. Walgama, S. Ronnback, and J. Sternby. Generalisation of conditioning technique for anti-windup compensators. In *IEE Proceedings D Control Theory and Applications*, volume 139, pages 109–118. IET, 2008.
- [106] D.A. Walters, J.P. Cleveland, N.H. Thomson, P.K. Hansma, M.A. Wendman, G. Gurley, and V. Elings. Short cantilevers for atomic force microscopy. *Review of Scientific Instruments*, 67(10):3583–3590, 1996.
- [107] Y. Wu and Q. Zou. Iterative control approach to compensate for both the hysteresis and the dynamics effects of piezo actuators. *IEEE Transactions on Control Systems Technology*, 15(5):936–944, 2007.
- [108] H. Xie, M. Rakotondrabe, and S. Régnier. Characterizing piezoscanner hysteresis and creep using optical levers and a reference nanopositioning stage. *Review of Scientific Instruments*, 80:046102, 2009.
- [109] Q. Zhong, D. Inness, K. Kjoller, and V.B. Elings. Fractured polymer/silica fiber surface studied by tapping mode atomic force microscopy. *Surface Science Letters*, 290(1-2):L688–L692, 1993.

List of Publications

Journal Papers:

- S. Kuiper, and G. Schitter.
Active Damping of a Piezoelectric Tube Scanner using Self-Sensing Piezo Actuation.
Mechatronics, volume 20, pages 656-665, (2010)
- S. Kuiper, and G. Schitter.
Model-Based Feedback Controller Design for Dual Actuated Atomic Force Microscopy
Mechatronics, (in press),(2011)
- J. Steininger, S. Kuiper, S. Ito, and G. Schitter.
Schnelle Rasterkraftmikroskopie durch moderne Regelungstechnik und mechatronische Systemintegration.
e & i Elektrotechnik und Informationstechnik, volume 129, pages 28-33, (2012)

Book Chapters:

- S. Kuiper, and G. Schitter.
Improving the Imaging Speed of AFM with Modern Control Techniques.
In *Control Technologies for Emerging Micro and Nanoscale Systems*, volume 413 of *Lecture Notes in Control and Information Sciences*, pages 83-100, Editors: E. Eleftheriou, and S.O.R. Moheimani, Springer-Verlag, Berlin-Heidelberg, Berlin-Heidelberg, ISBN: 978-3-642-22172-9, (2011)

Refereed Conference Proceedings:

- S. Kuiper, and G. Schitter.
Self-Sensing actuation and Damping of a Piezoelectric Tube Scanner for Atomic Force Microscopy.
Proceedings of the European Control Conference 2009, Budapest, Hungary, pages 3887-3890, (2009)
- S. Kuiper, and G. Schitter.
Mimo Self-Sensing Actuation of a Piezoelectric Tube Scanner.
Proceedings of the ASME 2009 Dynamic Systems and Control Conference, Hollywood, CA, USA, pages 811-817, (2009)

- S. Kuiper, and G. Schitter.
Dual Actuated Nano-Positioning for High Speed Atomic Force Microscopy.
Proceedings of the 10th International Conference of the European Society for Precision Engineering and Nanotechnology Delft, The Netherlands, volume 1, pages 225-228, (2010)
- S. Kuiper, A. Fleming, and G. Schitter.
Dual Actuation for High Speed Atomic Force Microscopy.
Proceedings of the 5th IFAC Symposium on Mechatronics Systems, Cambridge, MA, USA, pages 220-226, (2010)
- S. Kuiper, P.M.J. Van den Hof, and G. Schitter.
Towards Integrated Design of a Robust Feedback Controller and Topography Estimator for Atomic Force Microscopy.
Proceedings of the 18th IFAC World Congress, Milan, Italy, pages 12709-12714, (2011)
- S. Kuiper, P.M.J. Van den Hof, and G. Schitter.
Trade-off between the control bandwidth and the measurement accuracy in Atomic Force Microscopy.
To appear in the Proceedings of the 2012 IEEE International Instrumentation and Measurement Technology Conference, 13-16 May 2012, Graz, Austria, 2012

Non-refereed Conference Proceedings:

- S. Kuiper, and G. Schitter.
Sensorless damping of a Piezoelectric tube scanner.
Book of Abstracts 27th Benelux Meeting on Systems and Control, Heeze, the Netherlands, page 192, (2008)
- S. Kuiper, and G. Schitter.
Self-sensing actuation and damping of a Piezoelectric Tubescanner.
Book of Abstracts 28th Benelux Meeting on Systems and Control, Spa, Belgium, page 173, (2009)
- S. Kuiper, A.K. Madhusudhanan, P.M.J. Van den Hof, and G. Schitter.
Design of Feedback controllers and Topography Estimator for Dual Actuated Atomic Force Microscopy.
Book of Abstracts 29th Benelux Meeting on Systems and Control, Heeze, The Netherlands, page 202, (2010)
- S. Kuiper, P.M.J. Van den Hof, and G. Schitter.
Integrated Design of the Feedback Controller and Topography Estimator in Atomic Force Microscopy.
Book of Abstracts 30th Benelux Meeting on Systems and Control, Lommel, Belgium, page 31, (2011)

Summary

Mechatronics and Control Solutions for Increasing the Imaging Speed in Atomic Force Microscopy.

Stefan Kuiper

An Atomic Force Microscope (AFM) is a mechanical microscope in which the sample is probed by a very sharp tip, which allows to measure various sample properties such as the sample topography. As in AFM the sample is probed point by point, AFM imaging is a relatively slow process. This fact limits the applicability of AFMs in fields where high throughput is important. This research is focussed on improving the imaging speed of AFM, without hampering the accuracy of these instruments. Different techniques are developed which have led to a faster lateral scanning speed, higher bandwidth control of the tip sample force, and improved accuracy of the topography estimate.

In order to probe a certain area of interest, in AFM the sample is scanned in the lateral plane relative to the measurement tip in a raster scan pattern via a piezoelectric scanning stage. The speed of the lateral scanning motion is strongly limited by the weakly damped resonances of the scanner stage, which especially at higher scanning speeds may cause strong oscillations and therefore limit the accuracy of the scanning motion. In this research a method is developed to actively dampen these scanner oscillations by active feedback control. The oscillation of the scanner stage generate charge fluctuations within the piezo actuators, which allow to measure these scanner oscillations without the need for expensive position sensors. By making use of these properties of piezo actuators, a cost-efficient method is developed to allow active damping of these scanner oscillations, resulting in a higher achievable imaging speed of atomic force microscopes. Experimental results verify a significant increase in the scanner oscillations and the associated image distortions during high speed imaging.

In AFM the force between the tip and the sample is controlled in a feedback loop, which manipulates the vertical distance between the tip and the sample via a piezoelectric actuator. This feedback loop prevents damage between the tip and the sample during imaging. Moreover, the based on the compensating actions of this feedback loop the sample topography can be estimated via a topography estimator. When higher imaging speeds are required the bandwidth of this feedback loop should be sufficiently high in order to track the varying sample topography

during scanning. In this research the influence of the increased control bandwidth of this feedback loop on the accuracy of the topography estimation is investigated. The accuracy of the topography estimation is restricted by the variations in the dynamical behavior of the system, which may occur for instance when changing the tip or the sample. A method is developed to identify the dynamical variations of the AFM instrument, and to explicitly take these into account in the design of the feedback controller and the topography estimator. An important conclusion of this work is that for a given AFM instrument a trade-off has to be made between the bandwidth of this feedback loop and the accuracy of the topography estimation. Moreover, it can be concluded that the variations in the dynamical behavior of the instrument may be an important design criterion for future AFM systems, to allow both high speed and accurate AFM imaging.

The control bandwidth of the feedback loop controlling the force between the tip and the sample is often strongly limited by the first resonance modes of the piezoelectric actuators. Increasing these resonance frequency often comes at the cost of a reduction in positioning range of the piezo actuators. However, often in AFM imaging the larger amplitude topographic variations occur at relatively low frequencies, while the high frequency topography variations are generally of smaller amplitude. This allow the use of a combination of a long range, low bandwidth actuator, with a short range, high bandwidth actuator, which allows to increase the control bandwidth without sacrificing effective positioning range. In this research the advantages of dual actuated control of the tip-sample force in AFM are investigated. A model-based feedback controller is designed to control the tip-sample force with these two actuators, while preventing strong destructive interference between the two actuators. Moreover, an anti-windup controller is designed which prevents the control loop of getting unstable when saturation of the short-range actuator occurs. Experimental results verify that the system with the dual actuators is about 20 times faster then the system a single actuator, which results in significantly less force variations between the tip and the sample during imaging, and allows significantly faster AFM imaging. Furthermore, it is shown that the use of multiple actuators allows more design freedom in the controller design to suppress the uncertain dynamical modes of the system, which allows more accurate AFM imaging.

Samenvatting

Mechatronische en regeltechnische oplossingen voor het verhogen van de meetsnelheid van atoomkracht microscopen.

Stefan Kuiper

Een atoomkracht microscoop (AFM) is een mechanische microscoop waarbij het sample wordt afgetast door een zeer fijne naald. Met een AFM kunnen verschillende eigenschappen van het sample gemeten worden met een resolutie in het nanometerbereik. Hierbij wordt het sample in een laterale scanbeweging onder de naald bewogen, terwijl deze in verticale richting door de naald wordt afgetast. Omdat in een AFM het sample punt voor punt wordt afgetast is deze vorm van microscopie een relatief langzaam proces, wat de doorvoersnelheid en daarmee de toepasbaarheid van deze microscopen sterk beperkt. Dit onderzoek is gericht op het verhogen van de meetsnelheid van AFM's door middel van het verbeteren van het mechatronisch ontwerp en de regelstrategieën.

Een belangrijke beperking voor de snelheid van AFM is de snelheid van de laterale scanbeweging waarmee het sample onder de naald bewogen wordt. Deze beweging wordt gegenereerd door een piezoelektrisch aangedreven positioneringmodule. De snelheid van deze laterale scanbeweging wordt sterk beperkt door de zwak gedempte resonanties van deze positioneringmodule die vooral bij hoge scansnelheden sterke oscillaties kunnen veroorzaken en daarmee de nauwkeurigheid van de scanbeweging kunnen beperken. In dit onderzoek is een oplossing bedacht voor dit probleem door deze resonanties actief te dempen met behulp van een terugkoppelregeling. De oscillaties van de positioneringmodule genereren meetbare ladingsfluctuaties in de piezo-actuatoren die het mogelijk maken deze oscillaties te meten zonder gebruik te maken van dure positie-sensoren. Door hiervan gebruik te maken is een kostenefficiënte methode ontwikkeld om deze resonanties actief te dempen en daarmee de toelaatbare scansnelheid van AFM te verhogen. Experimentele resultaten laten zien dat de oscillaties van de positioneringmodule sterk zijn gereduceerd en daarmee de beeldverstoringen tijdens hoge scansnelheden.

Tijdens het scannen wordt in AFM de kracht tussen de naald en het sample geregeld met behulp van een terugkoppelregelaar die de verticale afstand tussen het sample en de naald regelt met behulp van piezo-actuatoren. Deze

terugkoppelregelaar moet schade aan het sample en de naald voorkomen. Daarnaast kan op basis van de geleverde regelactie de topografie van het sample worden geschat via een topografieschatter. Wanneer hogere scansnelheden vereist zijn is het van belang dat de regelbandbreedte van deze terugkoppelregelaar voldoende hoog is om de topografie van het sample te volgen. In dit onderzoek is onderzocht wat het verhogen van de regelbandbreedte voor invloed heeft op de nauwkeurigheid van het instrument. Deze nauwkeurigheid wordt beperkt door variaties in het dynamische gedrag van het systeem die bijvoorbeeld ontstaan wanneer het sample of de naald gewisseld worden. Er is een methode ontwikkeld om deze dynamische variaties te identificeren en de invloed hiervan op de meetnauwkeurigheid expliciet mee te nemen in het ontwerp van de terugkoppelregelaar en de topografieschatter. Een belangrijke conclusie van dit onderzoek is dat voor een gegeven AFM een directe afweging geldt tussen de regelbandbreedte van de terugkoppelregelaar enerzijds en de nauwkeurigheid van de topografieschatting anderzijds. Bij het ontwerp van de regelaar en de topografieschatter moet daarom sterk rekening gehouden worden met het beoogde toepassingsgebied van het instrument. Ook kan geconcludeerd worden dat het verminderen van de variaties in het dynamische gedrag van deze microscopen een belangrijk ontwerpcriterium is om zowel de snelheid als de meetnauwkeurigheid van deze instrumenten te kunnen verhogen.

De regelbandbreedte van de terugkoppelregelaar voor de kracht tussen de naald en het sample in AFM wordt sterk beperkt door hogere resonantiefrequenties van de piezo-actuatoren. Het verhogen van de eerste resonantiefrequenties van deze piezo-actuatoren gaat echter vaak ten koste van het positioneringsbereik. Daarentegen treden de topografie veranderingen met grotere amplitudes vaak op bij relatief lagere frequenties, en zijn de hoogfrequente topografie veranderingen meestal van kleinere amplitude. Door gebruik te maken van een combinatie van een lange-slag-actuator met relatief lage bandbreedte, en een korte-slag-actuator met hogere bandbreedte is het mogelijk om zowel een hoge regelbandbreedte te behalen als wel een groot effectief positioneringsbereik. In dit onderzoek zijn de mogelijkheden van het gebruik van twee actuatoren om de kracht tussen de naald en het sample te regelen in AFM onderzocht. Een modelgebaseerde regelstrategie is ontwikkeld om de kracht tussen de naald en het sample te regelen via deze twee actuatoren, zonder dat deze elkaar sterk gaan tegen werken. Daarnaast is een secundaire regelaar ontwikkeld die voorkomt dat het complete regelsysteem instabiel wordt wanneer de korte-slag-actuator tegen zijn begrenzingen aanloopt. Experimentele resultaten laten zien dat het systeem met de dubbele actuatoren ruim twintig keer sneller is dan het systeem met een enkele actuator, wat resulteert in aanzienlijk minder krachtvariaties tussen het sample en de naald tijdens het scannen en daardoor aanzienlijk hogere meetsnelheden toestaat. Ook is aangetoond dat het gebruik van meerdere actuatoren extra ontwerpvrijheid biedt om de onzekerheid van het dynamische gedrag van het systeem te onderdrukken, wat kan resulteren in een hogere meetnauwkeurigheid.

Curriculum Vitae

Stefan Kuiper was born in Zwolle, The Netherlands, in 1983. He received his bachelor degree in Mechanical Engineering in 2004, at the Hogeschool Windesheim, in Zwolle, The Netherlands. He continued his study in Mechanical Engineering at the University of Twente, in Enschede, The Netherlands, with a specialization in mechanical automation and mechatronics. His master thesis topic was to develop an adaptive feedforward control strategy for an active vibration isolation platform, for which he received his masters degree in 2007.

In October 2007 Stefan Kuiper started his PhD project at the Delft Center for Systems and Control (DCSC), Delft University of Technology, Delft, The Netherlands. The primary focus of his PhD project was to improve the mechatronic design and control of atomic force microscopes to increase the imaging speed and accuracy of these instruments. During this research he was supervised by Univ.-Prof. Dipl.-Ing.Dr.sc.techn. Georg Schitter, and Prof.dr.ir Paul Van den Hof. During his PhD project, Stefan Kuiper obtained the DISC certificate for fulfilling the course program requirements of the Dutch Institute for Systems and Control. In spring 2011 Stefan Kuiper worked as a visiting researcher in the Automation and Control Institute (ACIN) in Vienna, Austria. Furthermore, during his PhD project Stefan Kuiper supervised several M.Sc. students, and gave lectures and supervised lab-sessions for two different M.Sc. courses on control within the Delft Center for Systems and Control.

Since January 2012 Stefan Kuiper is affiliated with the Netherlands Organisation for Applied Scientific Research (TNO). His main research interest are mechatronics systems, motion systems, model-based control, and adaptive control.

